EXPERIMENTAL AND NUMERICAL PROGRESSIVE FAILURE ANALYSIS IN OPEN-HOLE TENSILE TESTS OF QUASI-ISOTROPIC COMPOSITE LAMINATES

by

Sina Ahmadvashaghbash

B.S., Mechanical Engineering, Urmia University, 2014

Submitted to the Institute for Graduate Studies in

Science and Engineering in partial fulfillment of

the requirements for the degree of

Master of Science

Graduate Program in Mechanical Engineering

Boğaziçi University

2018

EXPERIMENTAL AND NUMERICAL PROGRESSIVE FAILURE ANALYSIS IN OPEN-HOLE TENSILE TESTS OF QUASI-ISOTROPIC COMPOSITE LAMINATES

APPROVED BY:

Assoc. Prof. C. Can Aydıner ..... 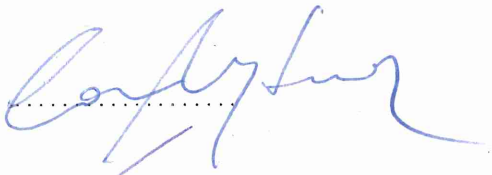
(Thesis Supervisor)

Prof. Dr. Nuri Ersoy ..... 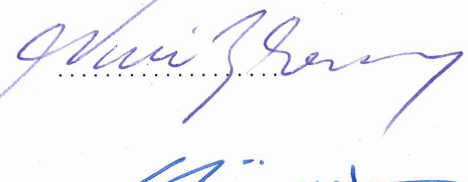
(Thesis Co-supervisor)

Prof. Dr. Fazıl Önder Sönmez ..... 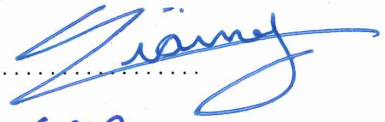

Assoc. Prof. Murat Sözer ..... 

DATE OF APPROVAL: 08.08.2018

ACKNOWLEDGMENTS

Working under supervision of Assoc. Prof. Can C. Aydıner and Prof. Dr. Nuri Ersoy was a valuable experience for me. They were not only patient and incredible mentors but also teachers with such a friendly approach towards students. This research would not have been possible without their guidance and encouragements. I find myself more than lucky to find the chance to work with them for more than two years.

I would like to acknowledge my thesis committee, Prof. Dr. Fazıl Önder Sönmez and Assoc. Prof. Murat Sözer for devoting their valuable time to read and comment on my thesis.

My special thanks goes to my current and former colleagues of Composites Research Group: Fatih E. Öz, Onur Yüksel, Mehmet Can Engül, Emre Çalık and Sina Narimani. I have a long list of friends who made my stay at the beautiful Istanbul unforgettable. To name a few, I would mention SeyedMehdi Emadian, Amin Delparish, Pouya Yousefi, Aidin Sheikhi, Mehdi Madani, Çağlar Şahin and Salar Kamari.

I would also like to acknowledge the support of my brothers Sina ZarePakzad and Siamak VajdiHokmabad and my beloved flatmates Julia Baarck and Nissa Berntsen. Thank you for always being there through all my ups and downs.

I devote this thesis to the most special part of my life, my family. This thesis would not have been possible without their love and encouragements.

ABSTRACT

EXPERIMENTAL AND NUMERICAL PROGRESSIVE FAILURE ANALYSIS IN OPEN-HOLE TENSILE TESTS OF QUASI-ISOTROPIC COMPOSITE LAMINATES

In this study, the progressive failure behavior of the Open-Hole Tension (OHT) specimens was analyzed by both numerical and experimental methods. The analysis of failure behavior of the notched composite laminates under tensile loading is carried out by implementing both intralaminar failure and delamination failure modes. For damage initiation of in-plane failure, Hashin's failure criterion has been assigned into the model mainly due to its higher accuracy that can be obtained with a lower number of material properties. In conjunction with damage initiation, damage evolution law for in-plane failure was defined in terms of fracture energy with linear softening. Initiation and evolution of delamination as a result of shear or normal stresses in adjacent plies were based on the Cohesive Zone Model. Numerical and experimental benchmarking studies have been conducted to evaluate Mode I and Mode II interlaminar fracture toughness by performing Double Cantilever Beam and End-Notched Flexure tests. In the experimental part of the study, damage progression in composites was investigated with Acoustic Emission (AE) technique. Optical instruments have been used to obtain reliable correlations with damage modes and the AE events. On the other hand, Digital Image Correlation and *in-situ* edge observation are applied simultaneously during the tensile tests of notched quasi-isotropic laminates. Finally, results are compared with predictions of the finite element model. The model is considered to successfully predict the strength and damage modes of the OHT specimens.

ÖZET

YARI-İZOTROPİK AÇIK DELIKLİ KOMPOZİT LAMİNATLARIN ÇEKME TESTLERİNDE HASAR İLERLEMENİN DENEYSEL VE SAYISAL ANALİZİ

Bu çalışmada Açık Delikli Çekme (OHT) numunelerin'de hasar ilerlemesinin davranışı hem sayısal hem de deneysel yöntemlerle analiz edilmiştir. Çentikli kompozit laminatların gerilme yüklemesi altındaki hasar davranışlarının analizi, hem intralaminar hasar hem de delaminasyon hasar modlarının uygulanmasıyla gerçekleştirilmektedir. Düzlem içi arızaya yönelik hasar başlangıcı için, Hashin'in hasar kriteri, daha az sayıda malzeme özelliği ile elde edilebilecek daha yüksek doğruluğu nedeniyle modele atanmıştır. Hasar başlangıcı ile bağlantılı olarak, düzlem içi hasar için hasar evrim yasası doğrusal yumuşatma ile kırılma enerjisi olarak tanımlanmıştır. Bitişik katlarda kesme veya normal gerilmelerin sonucu olarak delaminasyonun başlatılması ve evrimi, Cohesive Zone Model'ine dayanmaktadır. Çift Konsollu Kiriş ve Son Çentikli Eğilme testleri yapılarak Mod I ve Mod II katlararası kırılma tokluklarının değerlendirilmesi için sayısal ve deneysel kıyaslama çalışmaları yapılmıştır. Çalışmanın deneysel bölümünde, kompozitlerde hasar ilerlemesi Akustik Emisyon (AE) tekniği ile araştırılmıştır. Optik aletler, hasar modları ve AE olayları ile güvenilir korelasyonlar elde etmek için kullanılmıştır. Öte yandan, delikli yarı-izotropik laminatların çekme testleri sırasında aynı anda Dijital Görüntü Korelasyonu ve kenar gözlemleri uygulanmaktadır. Son olarak, sonuçlar sonlu eleman modelinin tahminleriyle karşılaştırılmıştır. Modelin, OHT numunelerin mukavemet ve hasar modlarını başarılı bir şekilde tahmin ettiği düşünülmektedir.

TABLE OF CONTENTS

ACKNOWLEDGEMENTS iii

ABSTRACT iv

ÖZET v

TABLE OF CONTENTS vi

LIST OF FIGURES ix

LIST OF TABLES xiii

LIST OF SYMBOLS xiv

LIST OF ACRONYMS/ABBREVIATIONS xvi

1. INTRODUCTION 1

1.1. Motivation 1

1.2. Objective 4

1.3. Literature Review 5

2. THEORY 12

2.1. In-Plane Failure Modes in Composites 13

2.2. Review of the Cohesive Zone Model (CZM) 13

2.3. Review of the Failure Criteria for In-Plane Damage Initiation of Fiber Reinforced Composites 19

2.4. Damage Evolution for In-Plane Failure Modes 23

2.5. Out-of-Plane Failure Modes 27

2.6. Mixed-Mode 29

2.7. Damage Stabilization.....31

3. EXPERIMENTAL METHODS.....32

3.1. Material 32

3.2. Manufacturing 33

3.3. Preparation of Tension Specimens 34

4. ASSESSMENT OF MODE I AND MODE II FRACTURE TOUGHNESS OF AS4/8552.....36

4.1. Double Cantilever Beam (DCB) Numerical Simulation.....36

4.1.1. Benchmarking Study of Turon et al. [36] 36

4.1.1.1. Benchmarking Model with Plane Strain Elements with Cohesive Surface Method 37

4.1.1.2. 3D Solid Elements with Cohesive Surface Interaction.....40

4.1.1.3. Continuum Shell Elements with Cohesive Surface Interaction..42

4.1.1.4. 3D DCB using Cohesive Elements Method.....42

4.1.1.5. Experimental and Numerical Investigation of Mode I Fracture Toughness of AS4/8552 45

4.2. End-Notch Flexure Experimental and Numerical Analysis 48

4.2.1. Introduction 48

4.2.2. Material and Test Specimens.....49

4.2.3. Experimental Procedure 49

4.2.4. Finite Element Model 51

4.2.5. ENF Test Results 54

4.2.6. Comparison with Finite Element Model 57

5. FINITE ELEMENT MODELING OF OHT COMPOSITES 60

6. EXPERIMENTAL DAMAGE MODE IDENTIFICATION IN OHT LAMINATES 67

6.1. Accoustic Emission (AE) 68

6.2. Digital Image Correlation (DIC) 68

6.3. Edge Microscopy 68

6.4. Experimental Results 69

7. DISCUSSION 74

7.1. Modification of the Proposed OHT Model 76

8. CONCLUSION AND FUTURE WORKS 80

REFERENCES 81

LIST OF FIGURES

Figure 1.1. Different materials contribution in average vehicle weight through 1975-2010 2

Figure 1.2. Penetration rate of composites in different markets compared to typical materials 3

Figure 2.1. Demonstration of global and local directions in a laminate 12

Figure 2.2. In-plane failure modes (a) Fiber tensile (b) Fiber compressive (c) Matrix tensile (d) Matrix compressive (e) Shear failure in the 1-2 plane 14

Figure 2.3. Shear failure in the 2-3 plane 14

Figure 2.4. Crack growth in a continuum body Ω, Γcoh is the part of the crack with active cohesive law (Process Zone) 15

Figure 2.5. Crack opening Modes 16

Figure 2.6. Various forms of traction-separation curves 16

Figure 2.7. Cohesive element transition and delamination path in DCB 17

Figure 2.8. A typical materials stress-strain response showing progressive failure 23

Figure 2.9. Equivalent stress-displacement curve in ABAQUS damage evolution....26

Figure 2.10. Bilinear traction-separation constitutive law....28

Figure 2.11. Mixed-mode behaviour of cohesive elements....30

Figure 3.1. Layup sequence for vacuum bagging operation....33

Figure 3.2. Autoclave (Boğaziçi University, Composites Laboratory)....33

Figure 3.3. Curing cycle for AS4/8552....34

Figure 3.4. Drilling process of a tension specimen....35

Figure 4.1. Mesh and boundary conditions for 2D DCB model....37

Figure 4.2. Deformed state of the 2D DCB....37

Figure 4.3. Load-displacement curve for 2D DCB with various mesh sizes....38

Figure 4.4. Load-displacement curve for DCB using reduced interface strength....39

Figure 4.5. BC and mesh structure of 3D DCB model using solid elements and S2S cohesive contact....40

Figure 4.6. Deformed shape of 3D DCB model using solid elements and S2S cohesive interaction....41

Figure 4.7. Delamination initiation of 3D DCB using solid elements and S2S cohesive interaction....41

Figure 4.8. Delamination propagation of 3D DCB using solid elements S2S cohesive interaction....41

Figure 4.9. Load-displacement curves for various DCB models....42

Figure 4.10. Delamination initiation of 3D DCB using continuum shell elements and cohesive elements....43

Figure 4.11. Delamination extension of 3D DCB using continuum shell elements and cohesive elements....44

Figure 4.12. Load-displacement curves for DCB models using cohesive elements for delamination....44

Figure 4.13. DCB Test setup....45

Figure 4.14. DCB specimen with loading blocks....46

Figure 4.15. Load-displacement responses of experimental tests, 2D and 3D FEM models....48

Figure 4.16. ENF Test setup....50

Figure 4.17. Finite Element model of ENF specimen....52

Figure 4.18. Delamination initiation and stiffness degradation (SDEG) in cohesive layer....53

Figure 4.19. Delamination evolution and stiffness degradation (SDEG) in cohesive layer (the upper roller is removed from the viewport in order to show the extension clearly) 53

Figure 4.20. Behavior of the upper composite arm and stiffness degradation (SDEG) in cohesive elements 54

Figure 4.21. Load-displacement responses and cumulative AE energy curves of ENF specimens 55

Figure 4.22. FEM and experimental load-displacement responses of ENF specimens 57

Figure 4.23. FEM 3 and experimental load-displacement responses of ENF specimens 58

Figure 4.24. Effect of mesh size in 3D ENF model 59

Figure 5.1. Specimen configuration 61

Figure 5.2. Partitions and mesh structure 62

Figure 5.3. Constraint between loading point-loading surface and the applied nodal displacement 62

Figure 5.4. Boundary conditions used for the OHT analysis 63

Figure 5.5. Final damage state in $[-45_2/0_2/45_2/90_2]_s$ OHT half-model 65

Figure 6.1. Test setup in KU Leuven 67

Figure 6.2. An edge image of $[-45_2/0_2/45_2/90_2]_s$ specimen with damage modes identification 69

Figure 6.3. Accumulation of AE clusters for $[+45_2/90_2/-45_2/0_2]_s$ laminate: (a) full gage length; (b) edge observation region only; (1) events amplitude; (2) events weighted frequency; (3) events location 70

Figure 6.4. Cluster groups for $[+45_2/90_2/-45_2/0_2]_s$ (a) Clusters from a representative test (b) Cluster boundaries 71

Figure 6.5. Damage evolution in $[+45_2/90_2/-45_2/0_2]_s$ laminate 73

Figure 7.1. Comparison of experimental and FEM stress-strain results 75

Figure 7.2. Modified OHT model with 4 doubled thickness plies and 3 cohesive layers 76

Figure 7.3. Final damage state in modified $[-45_2/0_2/45_2/90_2]_s$ OHT half-model 77

Figure 7.4. Final state of delaminations in modified FE model 77

Figure 7.5. Comparison of experimental and FE model stress-strain results 78

Figure 7.6. Modified FE model results for composite and cohesive layers 79

LIST OF TABLES

Table 2.1. Various l_{CZ} in Literature and specified M parameter 18

Table 3.1. Physical and mechanical properties of AS4/8552 32

Table 4.1. Experimental results with calculated Mode I fracture toughnesses..... 47

Table 4.2. Specimen configuration and dimensions 49

Table 4.3. Material parameters for UD composite 52

Table 4.4. Interlaminar strength, fracture energy and stiffness parameters for cohesive elements..... 52

Table 4.5. ENF test results..... 56

Table 4.6. Comparison of test results with a previous study using different methods for evaluation of G_{IIc}..... 56

Table 4.7. ENF FE results..... 58

Table 4.8. ENF FE/Experimental results 59

Table 5.1. Interpretation of discrete SDV1 values and specified damage state..... 63

Table 5.2. Final damage state in composite plies and cohesive layers..... 66

Table 7.1. Comparison of FE model and experiments 75

Table 7.2. Comparison of FE models and experiments..... 78

LIST OF SYMBOLS

a_0	Initial crack length between spans
B	Specimen width
b	Width of beam
C	Compliance
C_d	Damaged elasticity matrix
d_v	Viscous damage variable
d_f	Fiber damage variable
d_m	Matrix damage variable
d_s	Shear damage variable
E_i	Young's modulus
G_I	Mode I fracture toughness
G_{II}	Mode II fracture toughness
G_{ij}	Shear modulus
G_c	Critical energy release rate
G_s^C	Mode II fracture energy
h	Thickness of beam
L	Half of the distance between support spans
L^c	Characteristic length
l_{CZ}	Cohesive zone length
$l_{CZ,f}$	Maximum cohesive zone length for the first failed element
l_e	Length of the cohesive zone element
M	Damage operator
m	Slope of the secant of the force-deflection curve
N_e	Minimum number of elements required in cohesive zone
P_c	Maximum load reached during test
S	In-plane shear strength

S_L	Allowable longitudinal component of S
S_T	Allowable transverse component of S
t	Traction vector for cohesive elements
T_0	Initial thickness of a cohesive element
X_c	Compressive strength of lamina in the longitudinal direction
X_t	Tensile strength of lamina in the longitudinal direction
Y_c	Compressive strength of lamina in the transverse direction
Y_t	Tensile strength of lamina in the transverse direction
Γ_{coh}	Part of crack with active cohesive law (process zone)
δ^0	Critical opening displacement for damage onset
δ_{eq}	Equivalent displacement for in-plane failure
δ_m	Relative total displacement
ε	Strain tensor
η	Viscosity coefficient
ν	Poisson's ratio
σ	Normal stress tensor
σ_{eq}	Equivalent stress tensor for in-plane failure
σ_{true}	True stress tensor
σ_s^C	Compression shear strength
σ_t^C	Tension shear strength
τ	Shear stress tensor
τ^0	Interfacial strength
Ω	Continuum body

LIST OF ACRONYMS/ABBREVIATIONS

A:	Amplitude
AE:	Acoustic Emission
ASCA:	Autodesk Simulation Composite Analysis
B-K:	Benzeggagh-Kenane
BMW:	Bavarian Motor Works
CCD:	Charge-Coupled Device
CDM:	Continuum Damage Mechanics
CFRP:	Carbon Fiber Reinforced Polymer
CZM:	Cohesive Zone Model
CμT:	Computerized Micro-Tomography
DCB:	Double Cantilever Beam
DDM:	Discrete Damage Mechanics
DIC:	Digital Image Correlation
DoF:	Degree of Freedom
DPM:	Discrete Ply Model
DWT:	Discrete Wavelet Transform
EBD:	Energy-Based Degradation
EFM:	Element-Failure Method
ENF:	End-Notch Flexure
EU:	European Union
FCM:	Fuzzy C-Mean
FEA:	Finite Element Analysis
FEM:	Finite Element Modelling
FNM:	Floating-Node Method
FPF:	First-Ply Failure
FRP:	Fiber Reinforced Plastic
GFRP:	Glass Fiber Reinforced Polymer

KU Leuven:	Katholike Universiteit Leuven
MCT:	Multi-Continuum Theory
MRRC:	Manufacturer's Recommended Cure Cycle
NDT:	Non-Destructive Testing
OHC:	Open-Hole Compression
OHT:	Open-Hole Tension
PFA:	Progressive Failure Analysis
QI:	Quasi-Isotropic
SBS:	Short Beam Shear
SDEG:	Stiffness Degradation
SDV:	Solution Dependent Variable
SEM:	Scanning Electron Microscope
SIFT:	Strain Invariant Failure Theory
UD:	Unidirectional
UGENS:	User General Section
USD:	United States Dollar
VCCT:	Virtual Crack Closure Technique
WF:	Weighted Frequency
XFEM:	Extended Finite Element Method

1. INTRODUCTION

1.1. Motivation

Conventional materials used in industry cannot always satisfy the whole design specifications. Composite materials are recent favorable substitutes with number of advantages over common industrial materials, primarily because of their high-strength-to-weight ratio and low-cost machinery and tooling. By using composites, which generally are lighter than metals, a manufacturer would have a greater flexibility since the strength and the stiffness of the structure can be manipulated by stacking laminate plies in localized areas and along favored orientations. Also, with the advances made in the manufacturing processes, complex shapes can now be made in autoclaves.

Automotive composites as a developing market have been estimated to reach 4.3 billion USD in 2017 with a growth rate of 7% per year. Although composites with only 3.6% contribution to the automotive sector, are struggling against aluminum and steel but the potential of the Fiber-Reinforced Plastic (FRP) composites in weight-reduction of the vehicles can surpass both aluminum and steel. The urge for weight reduction is impelled by EU legislation on CO_2 emission, which has to be decreased to <95g CO_2/km by 2021 (<130g CO_2/km in 2015). The advantages of using composites as a medium for weight reduction can result in 7 million tons of CO_2 reduction in EU per year (total of 500 million ton in 2007 produced by road vehicles). This saving has the potential to improve the life quality in Europe by 1.4% [1].

The timeline and the recent application of composites in the automotive industry as a replacement for traditional materials have been started since the 1940s when first fiberglass body shell and air suspension is used in Stout 46. Since 1990s composites have found their place in mass-produced cars. The BMW i3 model (2013) can be considered as the world's first mass-produced carbon fiber automobile, where the passenger cell is completely made of

CFRP. Figure 1.1 shows the different materials contribution in average vehicle weight through 1975-2010. The growing trend of using plastics and composites is considered as a weight reduction option to decrease the CO2 emission [1].

Figure 1.2 demonstrates the penetration rate of composites in different markets compared to typical materials (aluminum or steel). These numbers clearly point out the transportation and automotive sector as one of the massive markets with the least composite penetration rate (3.6%) in comparison to conventional materials and show the great embedded potential in the mass application of CFRP in the automotive sector [2].

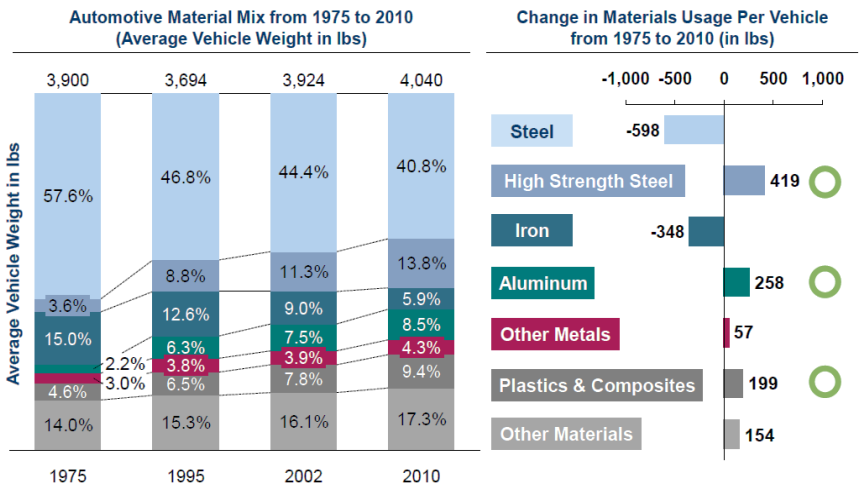

Figure 1.1. Different materials contribution in average vehicle weight through 1975-2010 [2].

Like any other industry, automotive composites have to overcome some challenges. Some of these barriers include recycling, expensive raw material, replacement of the whole damaged part rather than repairing and joining techniques in multi-material structures. Despite the fact that composites are promising materials in offering strength and stiffness, the brittle behavior, early damage initiation and lower failure strain are inevitable problems in tensile loading. The damage mechanisms in composites are rather different and related to

various failure modes under a variety of loading conditions. The failure modes in composite laminates can be divided into two classes; in-plane and out-of-plane failures. The combination of these failure modes will lead to the fracture, while in isotropic materials, fracture appears normal to the principal stress. In-plane failure mode which is also called as the intralaminar failure takes place in the plane of laminate and includes tensile and compressive failure of matrix or fiber. Out-of-plane failure or delamination which is the separation of two adjacent plies is the second failure mode. Delamination is considered as a catastrophic failure mode since it degrades the stiffness of the composite part considerably.

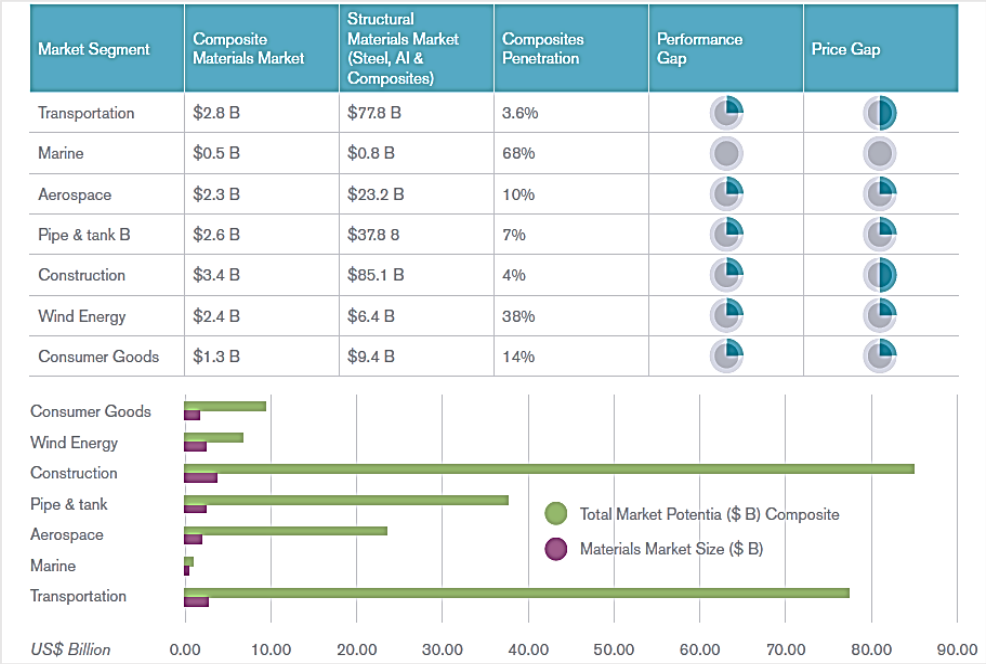

Market Segment	Composite Materials Market	Structural Materials Market (Steel, Al & Composites)	Composites Penetration	Performance Gap	Price Gap
Transportation	$2.8 B	$77.8 B	3.6%		
Marine	$0.5 B	$0.8 B	68%		
Aerospace	$2.3 B	$23.2 B	10%		
Pipe & tank B	$2.6 B	$37.8 8	7%		
Construction	$3.4 B	$85.1 B	4%		
Wind Energy	$2.4 B	$6.4 B	38%		
Consumer Goods	$1.3 B	$9.4 B	14%		

Figure 1.2. Penetration rate of composites in different markets compared to typical materials [1].

Progressive failure analysis in unidirectional (UD) laminates used to be considered as a mystery since ultimate failure is the only visible damage mode. However recent advances in Non-Destructive-Testing (NDT) methods like Acoustic Emission (AE) monitoring technique or Computerized Micro-tomography (CμT) enables to document the specific

failure modes. Furthermore, Finite Element Analysis can also be carried out as an alternative, predictive or a supplementary tool in damage evaluation of composites. In comparison to experimental study, FEA provides more comprehensive and expeditious results. The main purpose of this study is the development of a coherent progressive failure model and correlation investigation with experimental results.

The structural application of composites generally demands the presence of holes or predefined cracks. Investigation of an efficient Finite Element model that can cover both intralaminar and interlaminar failure modes in open-hole tension test of composites is considered worthwhile. Introducing a methodology which merely relies on the capabilities of ABAQUS software package in FEA rather than attached user-defined subroutines will provide a convenient insight for designers and a universal model that copes with different failure modes.

1.2. Objective

In this study, the progressive failure behavior of the open-hole tension specimens is analyzed by both numerical and experimental methods. Modelling of the failure behavior of the notched composite laminates under tensile loading is carried out by implementing in-plane (intralaminar) failure and delamination (interlaminar) failure. For damage initiation of in-plane failure, Hashin's failure criterion is implemented into the model mainly due to its high accuracy that can be obtained with a low number of material properties. In conjunction with damage initiation, damage evolution law for in-plane failure is defined in terms of fracture energy with linear softening. Initiation and evolution of delamination as a result of shear or normal stresses in adjacent plies are based on the Cohesive Zone Method (CZM). A comprehensive description of different failure criteria and CZM are presented in upcoming chapters. Finally, progressive failure analysis and experimental results are compared and the quality of the correlation is discussed.

1.3. Literature Review

Over the past decades, various approaches and parametric investigations have been conducted on the progressive failure analysis of the notched composites. In this chapter, some milestones of the previous studies are presented.

B.Y. Chen *et al*. [3] investigated the size effects on open-hole tensile composites. In their numerical study, it is observed that excluding delamination will give mesh-dependent and overvalued strengths which make delamination as an inevitable consideration in Progressive Failure Analysis (PFA). Matrix cracking failure is modeled by embedding crack elements in predicted directions of each ply, while delamination is performed by using cohesive elements. The variation of interface parameters required for interlaminar failure modelling including shear strength σ_s^C (=σ_s^T) and Mode II fracture energy G_s^C are perceived to have a negligible effect on damage patterns and pull-out failure mode. However, the delamination is observed to be extremely sensitive to these two parameters which puts the experimental measurements of them on the spot.

Coelho *et al*. [4] constructed a simplified 3-D model to predict damage initiation and progression of OHT that only relies on the capabilities of ABAQUS. Their proposed model is conducted by using composite lay-up method and continuum shell elements available in ABAQUS. This model with a reasonable accuracy predicts the fiber and matrix crack extension and the load-drop. Since cohesive elements or surfaces are not applied between plies it fails to capture the delamination phenomena. To reduce the computational cost, symmetry boundary condition, viscous regularization, mass scaling, global stabilization and damping factors are used in the model.

Bao *et al*. [5] employed surface-based cohesive contacts with fiber-aligned mesh for each ply instead of using cohesive elements. The benefits of applying cohesive interactions over cohesive elements are primarily due to the possibility of using different mesh configurations for differently oriented plies which are considered compulsory to predict

matrix cracks in this method. On the other hand, this approach eliminates the extra effort regarding the implementation of zero-thickness cohesive elements in ABAQUS. The proposed model shows a good correlation with experimental findings.

S.R. Hallet *et al*. [6] in a numerical and experimental study of the notched quasi-isotropic laminates reported the sequence and pattern of the damage propagation. Damage starts from the hole edge as matrix cracking with accompanied delaminations. These delaminations will appear at higher stresses by increasing the hole diameter. The delaminations growth around the hole allows a through-thickness damage extension with a final stress relaxation caused by splitting in 0˚ plies. Ultimately the damage will propagate all over the specimen and fiber breakage would be the closing failure. In the FE model which is carried out by using LS-DYNA Explicit code, in-plane failures are simulated by embedding split elements, while cohesive elements for delamination are introduced as a user-material and fiber failure is analyzed by using the Weibull criterion. The presented model is in a good correlation with experimental tests performed by Non-Destructive Testing methods such as X-ray and C-scan.

In a micromechanical study, M. U. Saeed *et al*. [7] examined the fracture surfaces of OHT specimens by using Scanning Electron Microscopy (SEM). From micrographs, it is observed that the microcracks initiate around the hole and expand towards the edges perpendicular to the applied load. The fiber breakage causes the load to transfer to the adjacent fibers by means of fiber/matrix interface. This denotes the key role of fiber breakage and fiber pull-out in the failure of OHT specimens.

B. Y. Chen *et al*. [8] in another study developed user-defined 3-D elements in Floating Node Method (FNM) for both ply elements and cohesive elements to predict progressive failure of OHT laminates in ABAQUS/Implicit. The default FEM element fails to predict movements of new crack boundaries, so the redefined elements are embedded with additional DoFs and functions. Besides including node, the FNM element also contains edge and surface connectivities. This model is successful at capturing complete sequence of failure modes and patterns in $[45_4/90_4/-45_4/0_4]_s$ laminates when compared to experimental tests.

Wisnom *et al*. [9] analyzed scaling effect in quasi-isotropic IM7/8552 OHT and OHC specimens in both sub-laminate-level scaling $[45/90/-45/0]_{ns}$ and ply-level $[45_n/90_n/-45_n/0_n]_s$ with varying hole diameters. It is concluded that increasing the hole size would not increase the strength of the laminates, but the damage mechanisms would be entirely different.

In another study Wisnom *et al*. [10] experimentally investigated the role of delamination in the intra-ply strength and failure mechanisms. The hole diameter is reported to have a direct effect on the quasi-isotropic laminate strength. By enlarging the notch diameter the strength converges to the strength of wide unnotched specimens. In other words, the delamination failure becomes more dominant as the hole diameter decreases. In ply-level scaled laminates the delamination extension is reported to be the ultimate failure mode, whereas in sub-laminate level scaled laminates, the ultimate failure mode is fiber breakage in 0˚ ply.

Abisett *et al*. [11] validated the experimental work published by Wisnom *et al*. [10] by utilizing an FE code-based damage mesomodel. In this model, critical strain energy release rates are presumed to be the same for both composite and cohesive elements. The three selected case verifications include thin, thick and intermediate ply-thickness laminates. The dominant failure modes are fiber breakage, delamination and combination of both as in experimental tests.

While the scaling effects have been the focus of the most studies on OHT failure mechanisms, Zhou *et al*. [12] analyzed the effect of material orthotropy on strength and progressive failure of OHT specimens. The material orthotropy effect has been investigated by comparing seven laminates with different stacking sequences in FE model. To predict the matrix damage initiation, Tsai-Wu, Hoffman and Pinho criteria have been implemented in ABAQUS UMAT. Pinho criterion has been considered to have a higher accuracy in determining damage progression.

Ridha *et al*. [13] applied Tsai-Wu criterion in conjunction with the maximum-stress criterion to simulate matrix and fiber failure initiation respectively. The delamination between plies is modelled by using cohesive elements and a traction separation law in

ABAQUS. As an alternative approach to the linear softening method for in-plane failure, zigzagging method (UMAT code) has been preferred as a stabilization algorithm to achieve converged results and also damage extension even after load drop.

Aidi *et al*. [14] conducted a numerical and experimental study on OHT coupons with dominant fiber pull-out or brittle behavior rather than delamination. To alleviate the computational cost and convergence issues, Autodesk Simulation Composite Analysis (ASCA) user-material has been plugged in ABAQUS. ASCA can be set to apply multi-continuum theory (MCT) and energy-based degradation (EBD) as failure initiation and evolution respectively. In the experimental part of their study, 3D Digital Image Correlation (DIC) technique has been employed to obtain strain maps around the notch. These strain fields are in a good correlation with the proposed model.

To model the shear behaviour and damage modes of Short Beam Shear (SBS) specimens under 3-point bending condition, Perogamvros *et al*. [15] utilized Stacked Shell (2.5D) method in LS-DYNA. In this approach, the sublaminates of the composite laminate are represented by shell elements which are tied together with cohesive elements or contact interaction to account for delamination. The numerical estimations negligibly differ from test result, but the method is considered to be computationally time-efficient.

Mohammadi *et al*. [16] compared FEA predictions with Acoustic Emission (AE) and Scanning Electron Microscope (SEM) monitoring of damage mechanisms in OHT composites. In FE simulation matrix failure, matrix/fiber debonding and fiber breakage failure criteria are implemented by using USDFLD user subroutine. The proposed 2D model consisted of 4-node plane stress (CPS4) elements without considering delamination. Discrete Wavelet Transform (DWT) and Fuzzy C-Means (FCM) clustering are used to process AE signals to distinguishing discrete damage modes. The AE using DWT are in a better correlation to FE as compared to the FCM method.

Higuchi *et al*. [17] constructed a predictive model using coupled extended finite element method and cohesive zone model (XFEM/CZM) based on quasi-isotropic 3D XFEM approach proposed by Nagashima *et al*. [18]. The elasto-plastic constitutive law is

implemented to count for non-linear behavior before peak load. Matrix crack and delamination extension are modeled with combining XFEM and CZM where zigzagging softening law used in later to ease computational convergence. Furthermore, fiber failure is modeled using Weibull criterion [6]. This model is considered to successfully predict the strength of OHT specimens.

Moure *et al*. [19] investigated the effect of ply-level scaling (clustering) thickness and placement on the evolution of matrix cracking in OHT specimens. A modified Discrete Damage Mechanics (DDM) model of Barbero-Cortes [20] has been used to count for the crack density, stiffness degradation and failure load in ABAQUS/Standard by User General Section (UGENS) user subroutine. By comparing laminates with different stacking sequences it is observed that cluster position in laminate has a significant effect on crack density evolution. For instance, matrix crack evolution is slower in laminates with clusters on the surface like $[90_7/0]_{2s}$ compared to laminates with interior clusters as in $[0/90_7]_{2s}$.

In an experimental study Green *et al*. [21] investigated the effect of hole diameter, laminate and ply thickness on strength of OHT laminates whilst keeping the width and length to hole diameter ratios (w/d and l/d respectively) constant. Increasing the ply thickness will alleviate the delamination stress and would change the failure mode from fiber pull-out to delamination. While keeping the thickness constant and increasing the hole size results in increased delamination stress which will change the damage mechanism from delamination to fiber pull-out in ply-level scaling.

Based on the experimental works of Green *et al*. [21] in a numerical study Bao *et al*. [5] employed surface-based cohesive interaction rather than cohesive elements to model the delamination and splitting. The reason behind this approach lies in the fact that using cohesive surfaces provides the possibility to assign different mesh patterns for different plies. Using aligned mesh in the fiber direction of each ply will allow the precise prediction of matrix crack paths.

Serra *et al*. [22] conducted a numerical investigation on scaling effects in open hole composites using Discrete Ply Model (DPM). This approach covers the fiber failure by using

C3D8 elements, where delamination and matrix crack is simulated using cohesive elements COH3D8 in ABAQUS/Explicit. It is proposed that a discrete number of matrix cracks are implemented in the model. Mesh size is based on the distance between two cracks such that it is 1.5-2 times the thickness of the ply.

Erçin *et al*. [23] examined the size effects on OHT and OHC laminates experimentally and numerically. The DIC method in conjunction with MATLAB scripts has been applied to detect the First-Ply Failure (FPF) load and progressive damage mechanisms on the top 90˚ ply in $[90/45/0\text{-}45]_s$ laminates with varying hole diameter. It is concluded that all the OHT coupons form transverse matrix cracks on the top ply originating from the hole boundary and also from free edges at upper applied strains. The most accurate analysis models to predict the strength of notched laminates are proved to be the stress fracture model [1] and finite fracture mechanics model [7] which only relies on the independent material properties.

In a novel approach T.E. Tay *et al*. [24] proposed a 3-D implicit code based on Element-Failure Method (EFM) or nodal force modification. This method has the advantage of not altering and recalculating the stiffness matrix of the element, unlike the conventional stiffness degradation method. The EFM is applied with strain invariant failure theory (SIFT) to spot the next failed element. Since SIFT is fully 3-D, it is chosen as the failure criteria to be accompanied with EFM to predict damage initiation and evolution.

Amacher *et al*. [25] analyzed the effect of ply thickness on damage progression and strength of composites. In thin-ply OHT specimens when compare to thick-ply coupons, there exists a failure mode transition from multi-mode failure to brittle failure in addition to failure at lower peak loads. This reason behind this transition to brittle behaviour is reported to be the suppression of early damage growth in thin-ply laminates, while in thick-ply laminates the damage initiates earlier and propagates in a stable trend up to the ultimate failure load.

Previous experimental and numerical investigations on progressive failure analysis of OHT laminates are briefly described in this section. None of the above mentioned papers did an extensive damage evolution observation, either using optical or Acoustic Emission

techniques to correlate the results of progressive damage analysis with the observed damage progression. Although some studies observed the specimens optically for damage progression but majority of these observations are limited to surface cracks. The main contribution of this study is observing how damage evolves using two optical techniques, namely DIC and microscopic edge observations, and AE technique to detect damage modes inside the specimens in order to correlate the progressive damage model predictions with experimentally observed damage modes. Furthermore, experimentally measured material data are used for setting up the model parameters in progressive damage analysis to obtain better correlation.

For damage initiation of in-plane failure, Hashin's failure criterion is suggested to be implemented into the model. In conjunction with damage initiation, damage evolution law for in-plane failure needs to be defined in terms of fracture energy with linear softening. Initiation and evolution of delamination CZM must also be considered between adjacent plies in the laminate for a realistic simulation. The objective of this study is the development of a coherent global progressive failure model with the implementation of experimentally obtained material properties and the correlation investigation with the Non-Destructive Testing (NDT) results.

2. THEORY

Modern composites mainly consist of two components, a matrix and a fiber. The fibers are mainly carbon, aramid or glass while the polymer matrix is usually a polymeric resin like an epoxy resin or polyester which provides toughness and compressional strength to the composite [26]. Several layers of carbon fiber reinforced polymers (CFRPs) with fiber orientations in different directions can be stacked to form a multi-layered composite laminate. A layer of the composite can be either unidirectional or woven in which the fibers are aligned in two or more directions. Unlike metals, the composite materials are not isotropic and show different strength, toughness, stiffness etc. in different directions. As seen in Figure 2.1, in addition to the global coordinate system (x, y, z), the local coordinate system is denoted as (1, 2, 3) with 1 being the fibre direction, 2 the transverse direction and 3 the through the thickness (out-of-plane) direction. A transversely orthotropic material is a material with identical mechanical properties in both 2 and 3 directions [27].

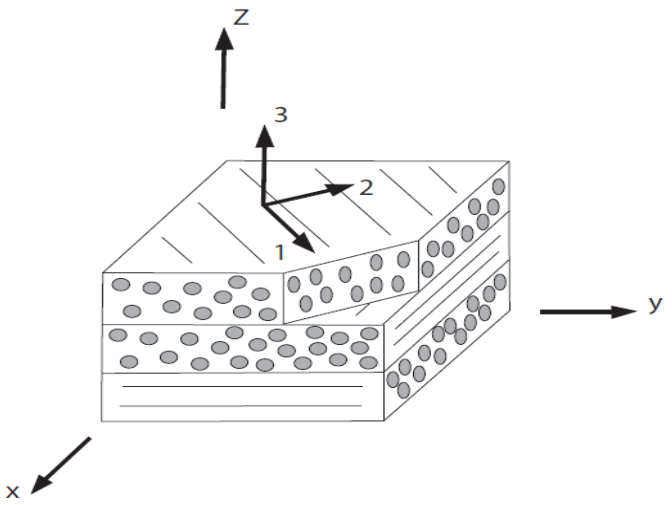

Figure 2.1. Demonstration of global and local directions in a laminate [28].

2.1. In-Plane Failure Modes in Composites

When composite material is subjected to various types of loading, different failure modes can be observed. Figure 2.2 and Figure 2.3 shows the schematic description of these discussed failure modes. The main in-plane failure modes are considered to be fiber tensile failure, fiber compressive failure, matrix tensile failure, matrix compressive failure and shear mode failure. These failure modes are described in this section. Fiber tensile failure, Figure 2.2.(a), which is considered as a catastrophic failure mode occurs when remaining undamaged fibers are no longer adequate to bear the applied load. Fiber compressive failure, Figure 2.2.(b), is mainly related to the shear behavior of matrix and defects in laminate such as voids and fiber misalignments. Fiber micro-buckling and formation of kinking bands are results of this failure mode.

Matrix tensile failure, Figure 2.2.(c), occurs perpendicular to the applied tensile load in the transverse direction. Due to the growth of matrix cracks, fibers may also split in this failure mode. Matrix compressive failure, Figure 2.2.(d), is due to the shear stresses rising in the matrix material and the resulted crack appears to be at an angle with compressive loading direction. Along the length of the fiber and matrix interface, failure in shear in the 1-2 plane, Figure 2.2.(e), occurs due to a shear separation of the matrix from the fiber. Since a shear stress generates a tensile stress on a 45˚ oriented plane, the overall shear performance of the laminate in the 2-3 plane (Figure 2.3) is limited to matrix tensile strength, fiber tensile strength and matrix/fiber interfacial strength.

2.2. Review of the Cohesive Zone Model (CZM)

Delamination or interfacial fracture in composite structures mainly generates from geometrical discontinuities such as matrix cracks and notches or manufacturing related defects. Delamination is defined as the separation of two adjacent plies in laminate and can lower the stiffness and strength of the composite part [31].

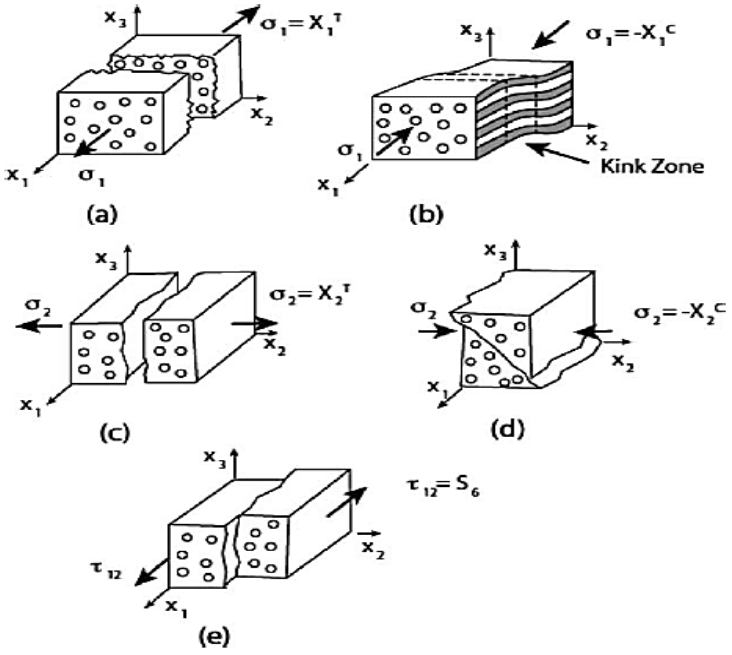

Figure 2.2. In-plane failure modes (a) Fiber tensile (b) Fiber compressive (c) Matrix tensile (d) Matrix compressive (e) Shear failure in the 1-2 plane [29].

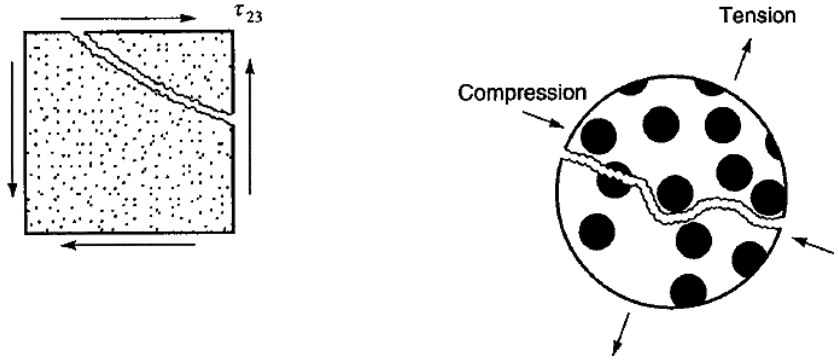

Figure 2.3. Shear failure in the 2-3 plane [30].

Therefore it is crucial to have a better understanding of the delamination behaviour in order to have a more accurate representation of inter-ply failure. This section is devoted to a general description and theoretical background regarding CZM.

The primary study on CZM backs to the works of Barenblatt [32] and Dugdale [33] on the fracture behaviour around the crack tip in brittle materials and steel. Hillerborg *et al*. [34] combined fracture mechanics with FEA to obtain more realistic results on crack formation and evolution. The CZM considers a cohesive zone (process zone) ahead of the crack tip to count for crack initiation and extension by using sets of constitutive equations such as traction-separation laws.

Figure 2.4 schematically represents the crack growth and cohesive zone of the crack in a body. The traction-separation laws associate the opposing tractions of the cohesive zone to the opening displacements. Depending on the crack opening mode (Mode I, II or III) as shown in Figure 2.5, the traction-separation laws are defined based on initial stiffness, maximum traction, interfacial strength and the area under the stress-displacement curve which is considered as the critical energy release rate G_c [31]. Different forms of traction-separation law are given in Figure 2.6 in which δ^0 denotes the critical opening displacement for damage onset. A linear elastic-linear softening behaviour is generally selected to implement in the simulations [35].

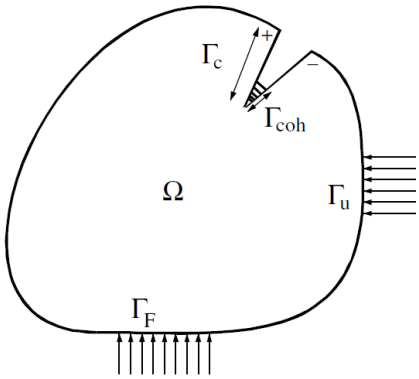

Figure 2.4. Crack growth in a continuum body Ω, Γ_{coh} is the part of the crack with active cohesive law (Process Zone) [36].

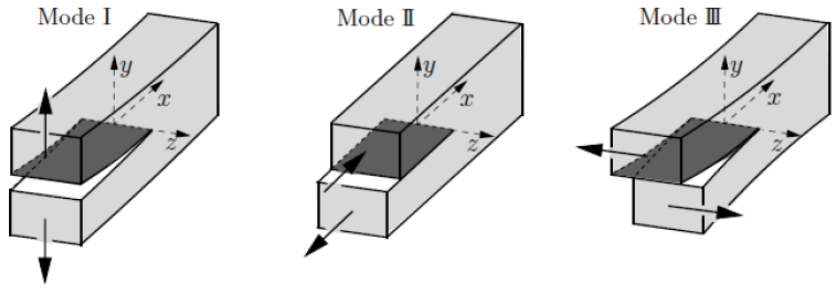

Figure 2.5. Crack opening Modes [37].

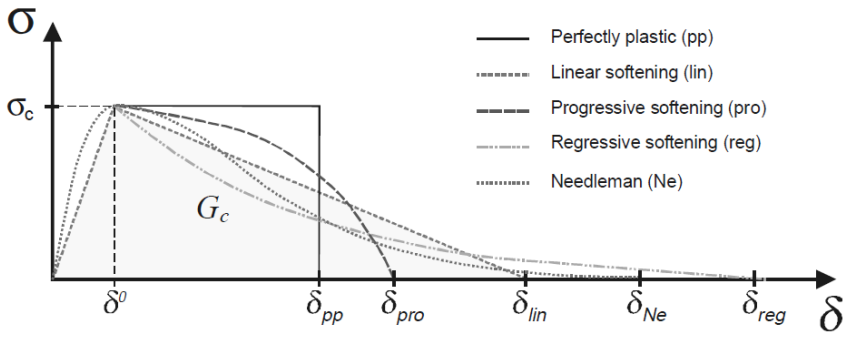

Figure 2.6. Various forms of traction-separation curves [35].

Based on the CZM approach, interface cohesive elements can be assigned in FEA to simulate delamination. Compared to alternative methods such as Virtual Crack Closure Technique (VCCT), which assumes that required energy for closing a crack is same as the energy consumed to open the same crack, this method provides the ability to have several crack paths without predefined crack propagation directions. To illustrate the cohesive zone formation and transition a DCB test can be considered as shown in Figure 2.7. After obtaining its maximum interfacial strength the element next to crack tip enters to its softening region of the traction-separation response. Ahead of the crack tip a cohesive zone length, l_{CZ}, forms as the opening stress increases and more elements undergo the same procedure.

The $l_{CZ,f}$ is defined as the maximum l_{CZ} when the first cohesive element at crack tip fails completely and causes the crack propagation [38].

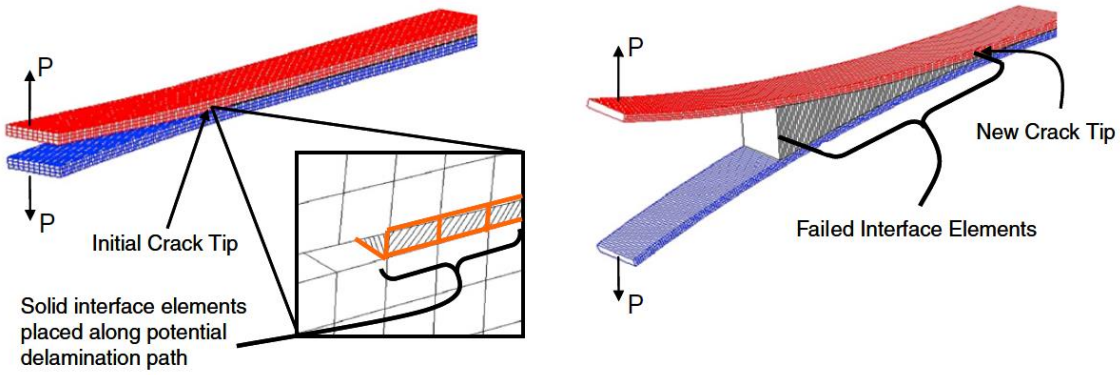

Figure 2.7. Cohesive element transition and delamination path in DCB [38].

The main drawback of the CZM is probably the mesh size requirements. In addition, the interface parameters are required to be selected precisely. Various studies have been conducted regarding the effect of different parameters on the behaviour of the cohesive elements. Turon *et al*. [39] investigated the minimum penalty stiffness (K) and the minimum number of elements within the CZ to correctly capture the delamination phenomena in FEM. It is observed that stiffness parameter is required to be large enough to ensure a stiff connection between two adjacent plies and small enough to avoid oscillatory and incorrect results. The element size is considered to be smaller than l_{CZ} (distance between the crack tip and the element with maximum traction). Cohesive zone length can be predicted by using:

$$l_{CZ} = ME\frac{G_c}{(\tau^0)^2} \tag{2.1}$$

Where E is the Young modulus (in the case of transversely isotropic materials, transverse elastic modulus, E_2). G_c is the critical energy release rate, τ^0 is the maximum

interfacial strength and the value for M parameter depends on the selected cohesive zone model. Table 2.1 demonstrates the common cohesive zone models and the specified M values. The minimum number of elements, N_e, required in the cohesive zone to obtain more accurate stress distribution within this zone in FEM, is not well addressed. Falk *et al*. [40] have assigned 2-5 elements and Turon *et al*. [39] have suggested 3 elements. This leads us to calculate the length of the cohesive zone element, l_e, using:

$$N_e = \frac{l_{CZ}}{l_e} \geq 3 \tag{2.2}$$

Considering this approach in a DCB test (Mode I) with the measured cohesive length of 1.2 mm [38], the required element length will be considerably small (0.4 mm). To eliminate this computationally inefficient barrier caused by assigning super fine mesh, Turon based on works of Alfano and Crisfield [41], which proves the insignificance of interfacial strength variation on final results, suggests the reduction of maximum interfacial strength to enlarge the cohesive zone length.

Table 2.1. Various l_{CZ} in Literature and specified M parameter.

	$\boldsymbol{l_{CZ}}$	$\boldsymbol{M}$
Hillerborg *et al*. [34]	$E\frac{G_c}{(\tau^0)^2}$	1.00
Rice [42]	$\frac{9\pi}{32}E\frac{G_c}{(\tau^0)^2}$	0.88
Barenblatt [32], Dugdale [33]	$\frac{\pi}{8}E\frac{G_c}{(\tau^0)^2}$	0.40
Irwin [43]	$\frac{1}{\pi}E\frac{G_c}{(\tau^0)^2}$	0.31
Hui *et al*. [44]	$\frac{2}{3\pi}E\frac{G_c}{(\tau^0)^2}$	0.21

The value of the interfacial strength, $\bar{\tau}^0$, required for the desired number of elements within the cohesive zone, N_e^0, is derived from Equation 2.1 and Equation 2.2 as:

$$\bar{\tau}^0 = \sqrt{\frac{E G_c}{N_e^0 l_e}} \tag{2.3}$$

The interfacial strength then selected as:

$$T = min\{\tau^0, \bar{\tau}^0\} \tag{2.4}$$

Fracture toughness and strength values (G_c and τ^0) are based on the loading mode. Satisfying results have been captured with reduced interfacial strength and a coarser mesh when compared to using default nominal strength. The main shortcoming of this approach is the inaccuracy of predicted stress distribution in the vicinity of the crack tip.

2.3. Review of the Failure Criteria for In-Plane Damage Initiation of Fiber Reinforced Composites

Failure in composite structures is considered as a complex phenomenon since the combination of in-plane and out-of-plane failures mentioned leads to the ultimate failure. Some of the earlier failure criteria for composites such as maximum stress, maximum strain, Tsai-Wu and Tsai-Hill are based on the failure criteria defined for isotropic materials. Later on, physically based criteria such as Hashin, considering the characteristics of composites, are developed. Commonly used failure criteria are briefly described in this section. In-plane failure criteria for CFRPs can be categorized into two main groups depending on how they take stress interactions into account: non-interactive and interactive failure criteria. Non-

interactive failure criteria such as maximum stress and maximum strain criteria neglect stress components interactions and their contribution in other directions leading to failure. The applied stress causes failure if it surpasses the material strength in the respective direction.

The Maximum Stress criterion for CFRPs is based on the uniaxial strength of a unidirectional (UD) composite ply. Failure initiates if one of the following conditions is satisfied:

Fiber failure : $$\frac{\sigma_1}{X_t} = 1 \text{ for } \sigma_1 > 0 \text{ and } \frac{|\sigma_1|}{X_c} = 1 \text{ for } \sigma_1 < 0 \quad (2.5)$$

Matrix failure: $$\frac{\sigma_2}{Y_t} = 1 \text{ for } \sigma_2 > 0 \text{ and } \frac{|\sigma_2|}{Y_c} = 1 \text{ for } \sigma_2 < 0 \quad (2.6)$$

Shear failure: $$\frac{|\tau_{12}|}{S} = 1 \quad (2.7)$$

Where σ_1, σ_2 and τ_{12} are normal and shear stresses. X_t and X_c are longitudinal material strengths in tension and compression, Y_t and Y_c are transverse strengths in tension and compression and S is the in-plane shear strength.

The Maximum Strain criterion similarly depends merely on the uniaxial failure strain of the UD ply. Failure occurs if one of the conditions below is verified:

Fiber failure : $$\frac{\varepsilon_1}{\varepsilon_{1t}^u} = 1 \text{ for } \varepsilon_1 > 0 \text{ and } \frac{|\varepsilon_1|}{\varepsilon_{1c}^u} = 1 \text{ for } \varepsilon_1 < 0 \quad (2.8)$$

Matrix failure: $$\frac{\varepsilon_2}{\varepsilon_{2t}^u} = 1 \text{ for } \sigma_2 > 0 \text{ and } \frac{|\varepsilon_2|}{\varepsilon_{2c}^u} = 1 \text{ for } \varepsilon_2 < 0 \quad (2.9)$$

Shear failure: $$\frac{|\gamma_{12}|}{\gamma_{12}^{u}} = 1 \quad (2.10)$$

Where ε_1, ε_2 and γ_{12} are normal and shear strains. ε_{1t}^{u} and ε_{1c}^{u} are longitudinal material ultimate failure strains in tension and compression, ε_{2t}^{u} and ε_{2c}^{u} are transverse failure strains in tension and compression and γ_{12}^{u} is the in-plane failure shear strain. The main downside of these non-interactive criteria is the absence of stresses or strains interactions despite the experimental observations of existing interactions [28].

Since damage in composites initiates with the presence of more than one stress or strain components, interactive failure criteria are defined to count for these interactions. Tsai-Hill modified the classical von Mises criterion for ductile materials so it would represent the failure in anisotropic ductile materials. For plane-stress states ($\sigma_3 = 0$) criterion is [45]:

$$\left(\frac{\sigma_1}{X}\right)^2 + \left(\frac{\sigma_2}{Y}\right)^2 + \left(\frac{\tau_{12}}{S}\right)^2 - \frac{\sigma_1\sigma_2}{X^2} = 1 \quad (2.11)$$

Where

$$X = X_t \text{ for } \sigma_1 > 0 \text{ and } X = -X_c \text{ for } \sigma_1 < 0 \quad (2.12)$$

$$Y = Y_t \text{ for } \sigma_2 > 0 \text{ and } Y = -Y_c \text{ for } \sigma_2 < 0 \quad (2.13)$$

The data for $X_{t,c}$ and $Y_{t,c}$ are obtained from standard uniaxial experimental tests. Tsai-Wu criterion is the more general form of Tsai-Hill criterion [46]:

$$\frac{\sigma_1^2}{X_tX_c} + \frac{\sigma_2^2}{Y_tY_c} + \frac{\tau_{12}^2}{S^2} + 2F_{12}\sigma_1\sigma_2 + \frac{\sigma_1}{X_t} + \frac{\sigma_2}{Y_t} - \frac{\sigma_1}{X_c} - \frac{\sigma_2}{Y_c} = 1 \quad (2.14)$$

The coefficient F_{12} is determined by a biaxial ($\sigma_1$and $\sigma_2 \neq 0$) experimental test. F_{12} can also be numerically calculated using Equation 2.15.

$$F_{12} = -\frac{1}{2}\sqrt{X_t X_c Y_t Y_c} \tag{2.15}$$

Hashin's damage initiation criterion [47] is a physically based criterion since each failure mode is covered with a specific equation.

Fiber tension $\sigma_1 > 0$

$$F_t^f = \left(\frac{\sigma_1}{X_t}\right)^2 + \left(\frac{\sigma_{12}}{S}\right)^2 = 1 \tag{2.16}$$

Fiber compression $\sigma_1 < 0$

$$F_c^f = \left(\frac{\sigma_1}{X_c}\right)^2 = 1 \tag{2.17}$$

Matrix tension $\sigma_2 > 0$

$$F_t^m = \left(\frac{\sigma_2}{Y_t}\right)^2 + \left(\frac{\sigma_{12}}{S}\right)^2 = 1 \tag{2.18}$$

Matrix compression $\sigma_2 < 0$

$$F_c^m = \left(\frac{\sigma_2}{2S_T}\right)^2 + \left[\left(\frac{\mathrm{Y_C}}{2\mathrm{S_T}}\right)^2 - 1\right]\frac{\sigma_2}{\mathrm{Y_c}} + \left(\frac{\sigma_{12}}{S_L}\right)^2 = 1 \tag{2.19}$$

Where σ_1, σ_2 and σ_{12} are the effective stress tensor components. S_L and S_T are the allowable longitudinal and transverse components of the S respectively. The mentioned failure criteria are damage initiation indicators. To attain the ultimate failure, which is mainly provoked by delamination or fiber failure, a damage evolution methodology is required.

2.4. Damage Evolution for In-Plane Failure Modes

The Hashin failure criterion is implemented for in-plane damage onset which is followed by an energy-based linear damage evolution. Once the damage initiation is met, stiffness degradation will reduce the load-carrying capacity of the laminate until the final failure. This is accompanied by a sharp load drop in force-displacement curve. Figure 2.8 demonstrates a typical material response undergoing progressive failure in a simple tension test. The linear-elastic response of the undamaged material is followed by damage initiation at point A. The path A-B is the damage evolution phase and at the point B elements can be set to be removed from stiffness matrix once they have fully degraded.

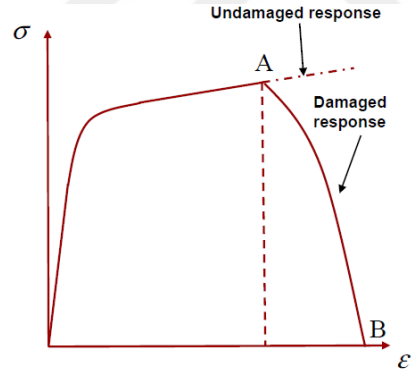

Figure 2.8. A typical materials stress-strain response showing progressive failure [48].

The stress-strain relations for the undamaged material can be interpreted by orthotropic linear elasticity. Considering the plane-stress case for a 2-D orthotropic material, we have:

$$\begin{Bmatrix} \varepsilon_1 \\ \varepsilon_2 \\ \gamma_{12} \end{Bmatrix} = \begin{bmatrix} 1/E_1 & -\nu_{12}/E_1 & 0 \\ -\nu_{21}/E_2 & 1/E_2 & 0 \\ 0 & 0 & 1/G_{12} \end{bmatrix} \begin{Bmatrix} \sigma_1 \\ \sigma_2 \\ \sigma_{12} \end{Bmatrix} \tag{2.20}$$

Where engineering constants E_1 and E_2 are the Young's modulus in the fibre and transverse direction respectively, G_{12} is the in-plane shear modulus, ν_{12} and ν_{21} are Poisson's ratios. The effective stress is applied to assess damage initiation criterion as [49]:

$$\sigma = M\sigma_{true} \tag{2.21}$$

The damage operator, M, is:

$$M = \begin{bmatrix} \frac{1}{(1-d^f)} & 0 & 0 \\ 0 & \frac{1}{(1-d^m)} & 0 \\ 0 & 0 & \frac{1}{(1-d^s)} \end{bmatrix} \tag{2.22}$$

The d_f ,d_m and d_s reflect the current states of fibre, matrix and shear damage respectively and are derived from damage variables d_t^f, d_c^f, d_t^m and d_c^m corresponding to pre-discussed four failure modes as:

$$d^f = \begin{cases} d_t^f \; if \; \sigma_1 \geq 0 \\ d_c^f if \; \sigma_1 < 0 \end{cases} \tag{2.23}$$

$$d^m = \begin{cases} d_t^m \; if \; \sigma_2 \geq 0 \\ d_c^m if \; \sigma_2 < 0 \end{cases} \tag{2.24}$$

$$d^s = 1 - (1-d_t^f)(1-d_c^f)(1-d_t^m)(1-d_c^m) \tag{2.25}$$

Prior to damage initiation and propagation, M equals to the dentity matrix. Value of one or higher for M denotes that the damage has been initiated. The damage evolution determines the material behaviour and rate of the reduction in stiffness after the damage onset is satisfied. Since CFRPs show an elastic-brittle behaviour, no plastic deformation is

considered regarding behaviour of composites. Damage models for composites are mainly based on Continuum Damage Mechanics (CDM) framework, where the material response is controlled by a damage parameter.

For a damage material the constitutive expression is [50][51]:

$$\sigma = C_d \varepsilon \tag{2.26}$$

Where ε is the strain tensor and C_d is the stiffness matrix (inverse of the compliance matrix) for damaged lamina and is written as:

$$C_d = \frac{1}{D}\begin{bmatrix} (1-d_f)E_1 & (1-d_f)(1-d_m)\nu_{21}E_1 & 0 \\ (1-d_f)(1-d_m)\nu_{12}E_2 & (1-d_m)E_2 & 0 \\ 0 & 0 & D(1-d_s)G_{12} \end{bmatrix} \tag{2.27}$$

With

$$D = 1-(1-d_f)(1-d_m)\nu_{21}\nu_{12} \tag{2.28}$$

Where ν_{12} and ν_{21} are Poisson's ratios. Material undergoes stiffness degradation as the damage parameters grow. An integration point can be removed from mesh when a damage parameter for that point reaches the value of unity. The deleted elements will no longer contribute any strength to the structure. A characteristic length parameter L^c has been introduced within ABAQUS to reduce mesh dependency and also to state constitutive law in terms of stress and equivalent displacement ($\sigma - \delta$). The damage evolution behaviour regarding any of the four failure modes is shown in Figure 2.9, and the characteristic length is explained below.

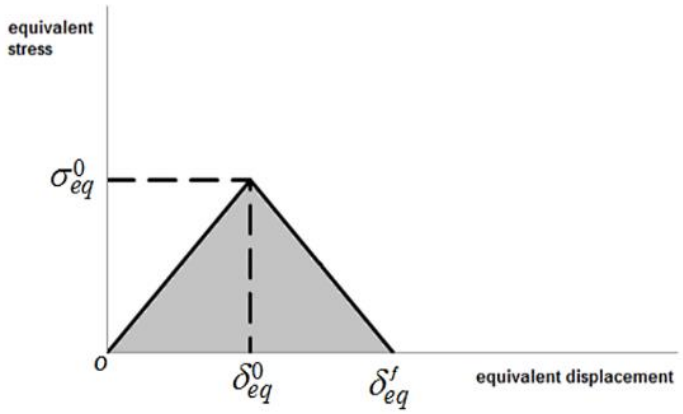

Figure 2.9. Equivalent stress-displacement curve in ABAQUS damage evolution [50].

The δ_{eq}^{0} and σ_{eq}^{0} are the equivalent displacement and stress at initiation and δ_{eq}^{f} is the displacement at failure. The negative slope of post damage initiation is obtained by evolution the of the damage parameters based on equivalent stress and displacement equations for four different failure modes:

Fiber tension ($\sigma_1 \geq 0$):

$$\delta_{eq}^{ft} = L^c \sqrt{\langle \varepsilon_1 \rangle^2 + \alpha \varepsilon_{12}^2} \tag{2.29}$$

$$\sigma_{eq}^{ft} = \frac{\langle \sigma_1 \rangle \langle \varepsilon_{11} \rangle + \alpha \sigma_{12} \varepsilon_{12}}{\delta_{eq,t}^{f} / L^c} \tag{2.30}$$

Fiber compression ($\sigma_1 < 0$):

$$\delta_{eq}^{fc} = L^c \langle -\varepsilon_{11} \rangle \tag{2.31}$$

$$\sigma_{eq}^{fc} \frac{\langle -\sigma_1 \rangle \langle -\varepsilon_{11} \rangle}{\delta_{eq,c}^{f} / L^c} \tag{2.32}$$

Matrix tension ($\sigma_2 \geq 0$):

$$\delta_{eq}^{mt} = L^c \sqrt{\langle \varepsilon_2 \rangle^2 + \varepsilon_{12}^2} \tag{2.33}$$

$$\sigma_{eq}^{mt} = \frac{\langle \sigma_2 \rangle \langle \varepsilon_{22} \rangle + \sigma_{12}\varepsilon_{12}}{\delta_{eq,t}^{m}/L^c} \tag{2.34}$$

Matrix compression ($\sigma_2 < 0$):

$$\delta_{eq}^{mc} = L^c \sqrt{\langle -\varepsilon_2 \rangle^2 + \varepsilon_{12}^2} \tag{2.35}$$

$$\sigma_{eq}^{mc} = \frac{\langle -\sigma_2 \rangle \langle -\varepsilon_{22} \rangle + \sigma_{12}\varepsilon_{12}}{\delta_{eq,c}^{m}/L^c} \tag{2.36}$$

Where characteristic length L^c is considered to be the length of a line across an element and the symbol $\langle\ \rangle$ is the Macaulay bracket defined for every $n \in \Re$, where $\langle n \rangle = (n + |n|)/2$. After damage initiation ($\delta_{eq} \geq \delta_{eq}^0$) damage variable for each mode is of the form:

$$d = \frac{\delta_{eq}^{f}(\delta_{eq} - \delta_{eq}^0)}{\delta_{eq}(\delta_{eq}^{f} - \delta_{eq}^0)} \tag{2.37}$$

For each failure mode the area under the σ_{eq}-δ_{eq} profile (Figure 9) is the dissipated energy due to failure, G_c. In order to properly define damage evolution for a material the fracture energy values for each failure mode must be known.

2.5. Out-of-Plane Failure Modes

The traction-separation behaviour of cohesive elements available in ABAQUS, as seen in Figure 2.10, assumes a linearly elastic behaviour pre-damage initiation and linear softening for evolution. This elastic behaviour is expressed in terms of nominal stresses (force divided by the initial area of an integration point) and nominal strains (separation of an integration point divided by initial thickness). Nominal traction vector, t, has three components: t_n, t_s and t_t corresponding to normal and shear tractions for a cohesive element. The nominal strains are defined as [52]:

$$\varepsilon_n = \frac{\delta_n}{T_0} \tag{2.38}$$

$$\varepsilon_s = \frac{\delta_s}{T_0} \tag{2.39}$$

$$\varepsilon_t = \frac{\delta_t}{T_0} \tag{2.40}$$

Where T_0 is the initial thickness of a cohesive element and δ_n, δ_s, and δ_{nt} are normal, in-plane and out-of-plane shear separations. The elastic behaviour can now be written as:

$$t = \begin{Bmatrix} t_n \\ t_s \\ t_t \end{Bmatrix} = \begin{bmatrix} K_{nn} & K_{ns} & K_{nt} \\ K_{ns} & K_{ss} & K_{st} \\ K_{nt} & K_{st} & K_{tt} \end{bmatrix} \begin{Bmatrix} \varepsilon_n \\ \varepsilon_s \\ \varepsilon_t \end{Bmatrix} = K\varepsilon \tag{2.41}$$

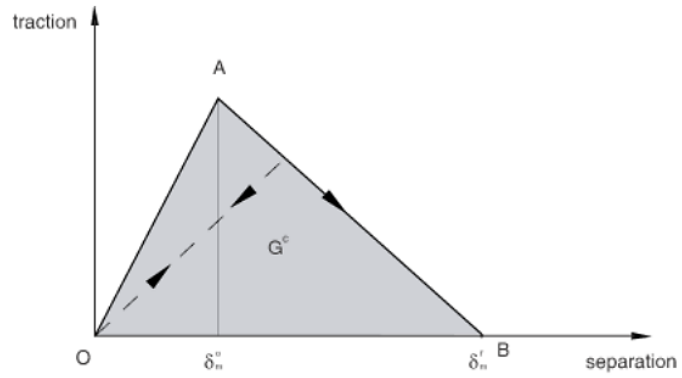

Figure 2.10. Bilinear traction-separation constitutive law [52].

The damage initiation is governed by quadratic nominal stress criterion as:

$$\left\{\frac{\langle t_n \rangle}{t_n^0}\right\}^2 + \left\{\frac{t_s}{t_s^0}\right\}^2 + \left\{\frac{t_t}{t_t^0}\right\}^2 = 1 \tag{2.42}$$

Where t_n^0, t_s^0 and t_t^0 are the peak nominal stresses in normal and shear directions respectively. Subsequent damage evolution is modelled as:

$$t_n = \begin{cases} (1-D)\bar{t}_n, & \bar{t}_n \geq 0 \\ \bar{t}_n, & \text{otherwise} \end{cases} \tag{2.43}$$

$$t_s = (1-D)\bar{t}_s \tag{2.44}$$

$$t_t = (1-D)\bar{t}_t \tag{2.45}$$

Where D is a scalar damage parameter evolving from 0 to 1 post initiation. The value of 1 denotes the complete failure of a cohesive element. $\bar{t}_n$, $\bar{t}_s$ and $\bar{t}_t$ are undamaged stress components.

2.6. Mixed-Mode

To describe the damage initiation and evolution for a cohesive element undergoing mixed-mode loading, a relative total displacement is defined as [53]:

$$\delta_m = \sqrt{\langle \delta_n \rangle^2 + \delta_s^2 + \delta_t^2} \tag{2.46}$$

Figure 2.11 illustrates the mixed-mode response of cohesive elements. The response under pure normal or pure shear loading is represented by unshaded triangles, while the intermediate vertical planes account for the damage response under mixed-mode conditions for various mode mixes. Damage evolution in mixed-mode conditions can be specified either in an effective-displacement-based definition or in an energy-based definition. Linear damage evolution is expressed by a damage variable, D, as:

$$D = \frac{\delta_m^f(\delta_m^{max} - \delta_m^0)}{\delta_m^{max}(\delta_m^f - \delta_m^0)} \tag{2.47}$$

Where δ_m^{max} is the maximum effective displacement obtained within loading history. δ_m^0 and δ_m^f are the effective displacement at damage initiation and cohesive element failure respectively.

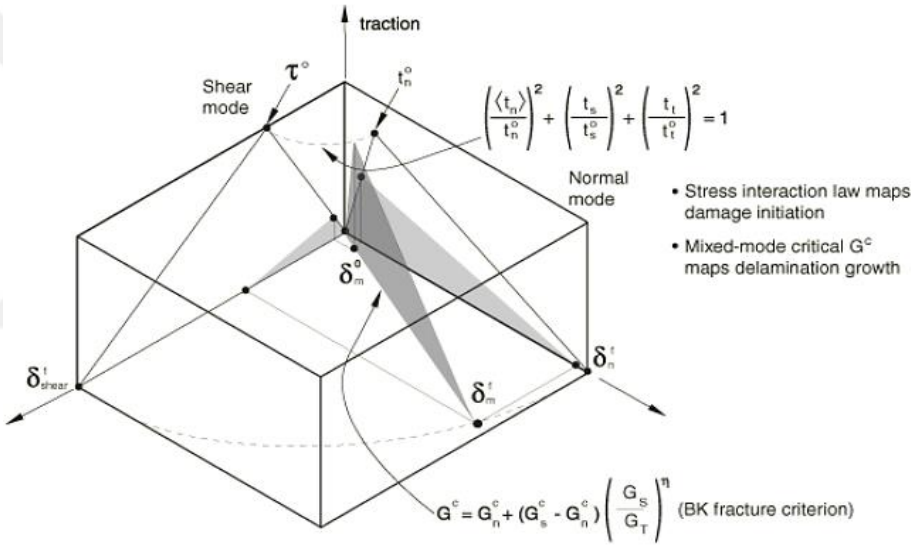

Figure 2.11. Mixed-mode behaviour of cohesive elements [52].

Damage evolution based on fracture energy (the area under the traction-separation curve) can be defined using power law fracture criterion as:

$$\left\{\frac{G_n}{G_n^c}\right\}^{\alpha} + \left\{\frac{G_s}{G_s^c}\right\}^{\alpha} + \left\{\frac{G_t}{G_t^c}\right\}^{\alpha} = 1 \tag{2.48}$$

The G_n^c, G_s^c and G_t^c are the critical fracture energies required to provoke failure in normal and two shear directions respectively. The Benzeggagh-Kenane (BK) fracture

criterion [54] is alternatively applied when the critical fracture energies along first and second shear directions are the same ($G_s^c = G_t^c$) and is given by:

$$G_n^c + (G_n^c - G_n^c)\left\{\frac{G_S}{G_T}\right\}^{\eta} = G^c \tag{2.49}$$

Where

$$G_S = G_s + G_t \tag{2.50}$$

$$G_T = G_n + G_S \tag{2.51}$$

With η as a material property.

2.7. Damage Stabilization

To overcome instability and convergence problems in nonlinear progressive failure analysis, which are mainly caused by stiffness degradation and softening behaviour, in ABAQUS/Implicit, viscous regularization scheme can be applied. Viscous damage variable based on damage evolution is defined as [50]:

$$\dot{d}_v = \frac{1}{\eta}(d - d_v) \tag{2.52}$$

The η in the above equation is the viscosity coefficient corresponding to the relaxation time in a viscous system. Where d is the evaluated damage variable in the inviscid model and d_v is the viscous damage variable. There exist four viscosity coefficients depending on four different failure modes present in damaged stiffness matrix, C_d (see Equation 2-26). Assigning small values for η (compared to time increment), usually with values from 10^{-5} to 10^{-3}, results in an improved convergence rate without affecting the outputs [50][55][56].

3. EXPERIMENTAL METHODS

3.1. Material

The material used in this study is AS4/8552 Hexcel® Composites. Hexply® 8552 is a high performance toughened epoxy resin which demonstrates good damage and impact resistance and commonly used in aerospace structures with embedded AS4 unidirectional fibers as reinforcement [57]. The physical and mechanical AS4/8552 prepreg properties are listed in Table 2.1.

Table 3.1. Physical and mechanical properties of AS4/8552.

	Data Sheet [57]	Sivakumar *et al*. [58]	Lemanski *et al*. [59]	FEM [60]	Units
Fiber Density	1.79				g/cm^3
Resin Density	1.30				
Nominal Laminate Density	1.58				
Nominal Fiber Volume	57.4				%
Ply Thickness	0.184				mm
E_1	141000	141300	124000	142840	MPa
$E_2 = E_3$	10000	10000	9500	10000	
$G_{12} = G_{13}$	-	4800	4900	5571	
G_{23}	-	-	4300	3278	
σ_1^T	2207	2206	-	2105	
σ_1^C	1531	1531	-	1531	
σ_2^T	81	-	-	51	
τ_{12}^S	-	114.5	-	114.5	
$\nu_{12} = \nu_{13}$	-	-	0.3	0.263	-
ν_{23}	-	-	0.3	0.525	-

3.2. Manufacturing

The manufacturing process is carried out by using autoclave in Composites Laboratory of Mechanical Engineering Department of Boğaziçi University. The autoclave maximizes the performance of thermoset composites by removal of all air voids. This can be achieved by pressurization and applying the temperature cycle namely cure cycle in autoclave [30]. Schematic view of vacuum bagging process and representational of an autoclave are shown in Figure 3.1 and Figure 3.2 respectively.

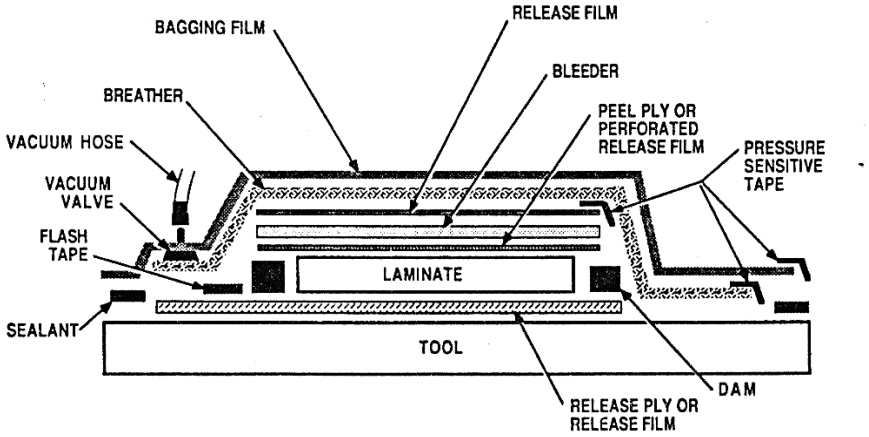

Figure 3.1. Layup sequence for vacuum bagging operation.

Figure 3.2. Autoclave (Boğaziçi University, Composites Laboratory).

The Manufacturer's Recommended Cure Cycle (MRCC) is demonstrated in Figure 3.3. This procedure starts with applying full vacuum (1 bar) followed by 7 bar gauge autoclave pressure. The first step is heating at a rate of 1- 3°C/min to 110°C ± 5° and holding at this temperature for 60 minutes. In the next step, temperature rises to 180°C ± 5°C with the constant rate of 1-3°C/min and stays for 120 minutes. Finally, the system cools at 2 – 5°C per minute and autoclave pressure vents out when the temperature reaches 60°C or below.

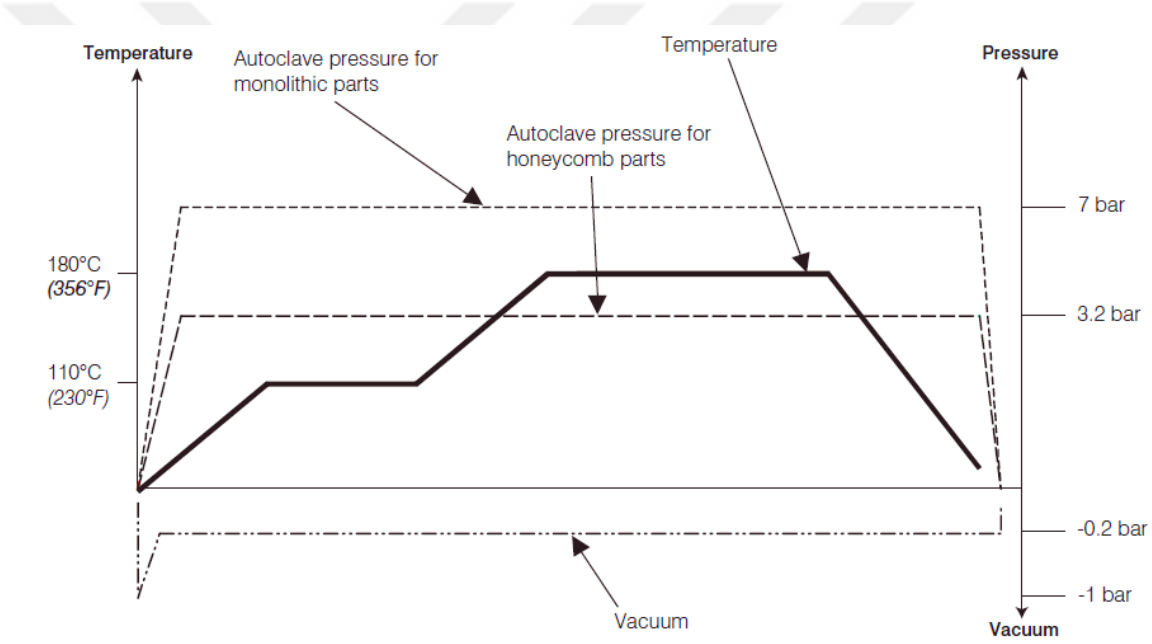

Figure 3.3. Curing cycle for AS4/8552 [57].

3.3. Preparation of Tension Specimens

The preparation procedure begins with cutting AS4/8552 unidirectional prepreg roll into desired directions and dimensions. According to the ASTM D-3039 [61] and ASTM D-5766 [62], a 30 x 30cm composite plate would be adequate to have at least 8 tension specimens. Finally, the CFRP plate is cut to standard specimen dimensions using 2mm thick water-cooled diamond disc. Since CFRPs are considerably soft in their through-thickness direction, to avoid crushing and early failure of the gripping sections within tension test, end

tabs should be attached to the specimens. End tabs are made of GFRP quasi-isotropic plates and manufacture by vacuum infusion technique with length and thickness of 50 cm and 1.5 mm respectively. Before attaching the end tabs on top and bottom surfaces of the plates, the gage section ends are tapered to 20˚-30˚ using grinding wheel. The adhesive required to bond CFRP to GFRP must have a high shear strength, for this reason, low cost-high strength *J-B Weld* steel reinforced epoxy twin tube adhesive is used which can endure up to 80kN load levels. The process of opening circular holes in the center of tension specimens is carried out according to ASTM D5766 standard. There exist various techniques to open a hole in CFRPs such as laser cut, water jet and drilling. The later has been applied within this study due to its cost efficiency and availability of drilling machines in Boğaziçi University machine shop. The drilling process should be done carefully in order to alleviate the delamination and fiber breakage around the hole. For this purpose *Sandvik CoroDrill 452 series* [63] carbide drill bits are preferred. Figure 3.4 shows the drilling setup. A wooden base is placed under the specimen to protect the drill bit tip after it leaves the composite. In addition, an open hole stainless steel plate is placed on top as a reference. These three plates are fixed together with a C-clamp and attached to the drilling machine to reduce vibrations. Finally, one edge of the specimens is grinded and polished with a grinding device for edge microscopy observations later on.

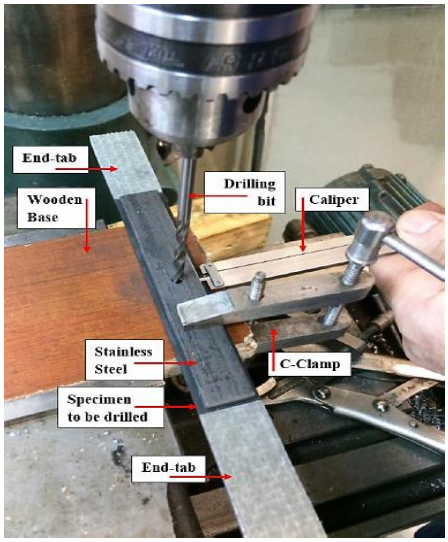

Figure 3.4. Drilling process of a tension specimen.

4. ASSESSMENT OF MODE I AND MODE II FRACTURE TOUGHNESS OF AS4/8552

4.1. Double Cantilever Beam (DCB) Numerical Simulation

4.1.1. Benchmarking Study of Turon *et al.* [36]

Decreasing run time for delamination simulations is a significant issue for designers. In order to increase the element length which would directly decrease the run time, a parametric study is carried out. Model parameters such as characteristic length, interfacial strength, etc. are optimized to obtain a good correlation between the test data and model predictions for DCB and ENF tests.

For Double Cantilever Beam (DCB) Test, according to the study of Falk *et al*. [40], the required number of elements in the cohesive zone should be between 2 and 5. This limits the required element length in a small interval. Turon *et al*. suggest that by keeping fracture energy constant and changing the interfacial strength, the cohesive zone length will be increased artificially meaning that larger elements can be used to apply the Falk's statement.

In this study, three different models for DCB test are applied for carbon/epoxy T300/977-2 with G_{Ic}= 0.352 N/mm. First one is to use plane strain elements with cohesive surfaces. The second one is to use 3D solid elements for plies with 3D cohesive elements between them. Finally, 3D continuum shell elements are replaced solid with elements. The model predictions are compared to the results discussed at Turon *et al*. [36] for benchmarking purposes.

4.1.1.1. Benchmarking Model with Plane Strain Elements with Cohesive Surface Method.

By using cohesive surface, using generalized plane strain elements to model a section perpendicular to the crack front and applying interaction properties between two layers, DCB test is simulated. *K* is calculated as 270000 N/mm^3 according to formulas presented in the study of Turon *et al*. This is assumed that at least 4 elements should be placed in the cohesive zone. Cohesive zone length is calculated approximately as 0.95 mm which means that element length must be at least 0.25 mm to reach more accurate results. Figure 4.1 shows the mesh structure of 2D DCB model (1 mm) and applied boundary conditions.

Figure 4.2 illustrates the deformed shape of the 2D DCB. Figure 4.3 shows the load-displacement results of the proposed model with several mesh sizes. These plots are also compared to the experimental data given in the original paper of Turon *et al*. All models are at the constant interfacial strength of 60 MPa.

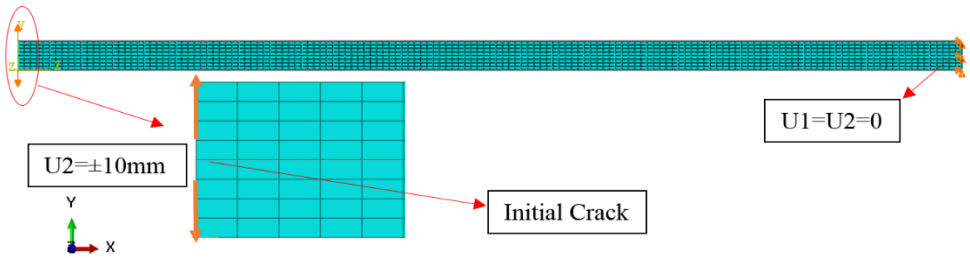

Figure 4.1. Mesh and boundary conditions for 2D DCB model.

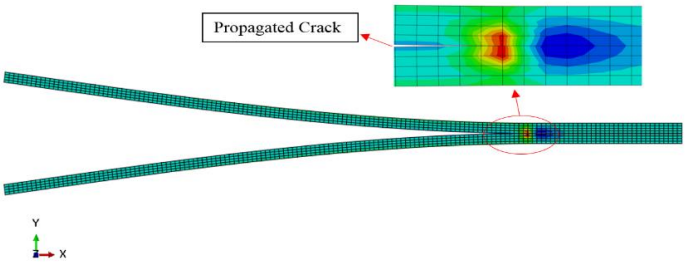

Figure 4.2. Deformed state of the 2D DCB.

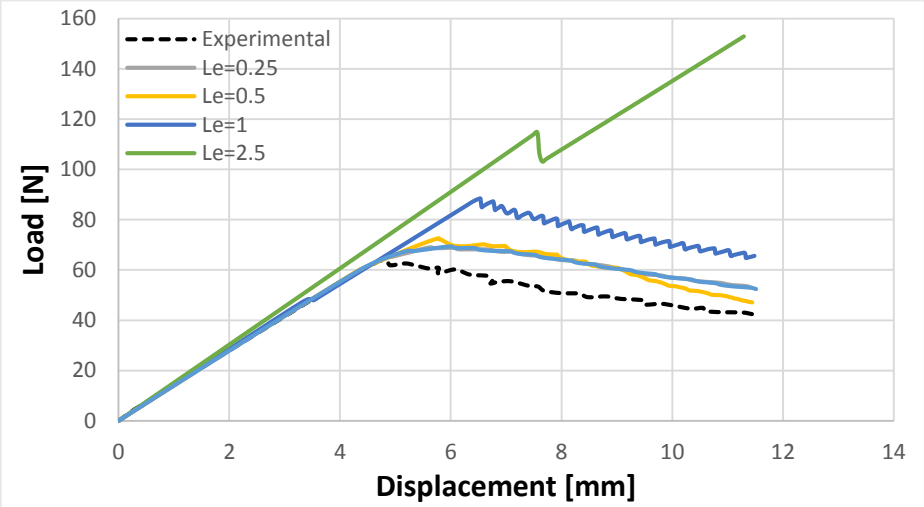

Figure 4.3. Load-displacement curve for 2D DCB with various mesh sizes.

According to the results for element lengths L_e =0.05, 0.25 and 0.5 mm, since there is no considerable difference, implementing 2-5 elements would give satisfying results (with constant interfacial strength) and decreasing mesh size would have a negligible effect on the results. In this case, having 4 elements in the cohesive zone would be adequate in our simulation. Despite the decrease in mesh size there still exist some differences with the experimental result. Since the interfacial stiffness parameter (K) is carried out by using equation below:

$$K = \frac{\alpha E_3}{t} \tag{4.1}$$

Where α is a parameter much greater than 1 ($\alpha >> 1$) and t is the thickness of the sub-laminate, it can be modified to have a higher correlation. Considering another case where larger mesh size is preferred, the requested cohesive zone length needs to be 4 mm. So the interfacial strength needs to be artificially reduced by using equation below:

$$\bar{\tau}^0 = \sqrt{\frac{EG_C}{N_e^0 l_e}} \tag{4.2}$$

Where N_e^0 is the number of elements in the cohesive zone. In order to reduce the computational time without sacrificing accuracy of the results, 1 mm mesh size can be applied with $\bar{\tau}^0 = 32$ MPa. The result of this transition is compared with experimental and using $\tau^0 = 60$ MPa in Figure 4.4. Since the number of cohesive elements has increased by using a reduced τ^0, obtained results are in a good correlation with experimental data.

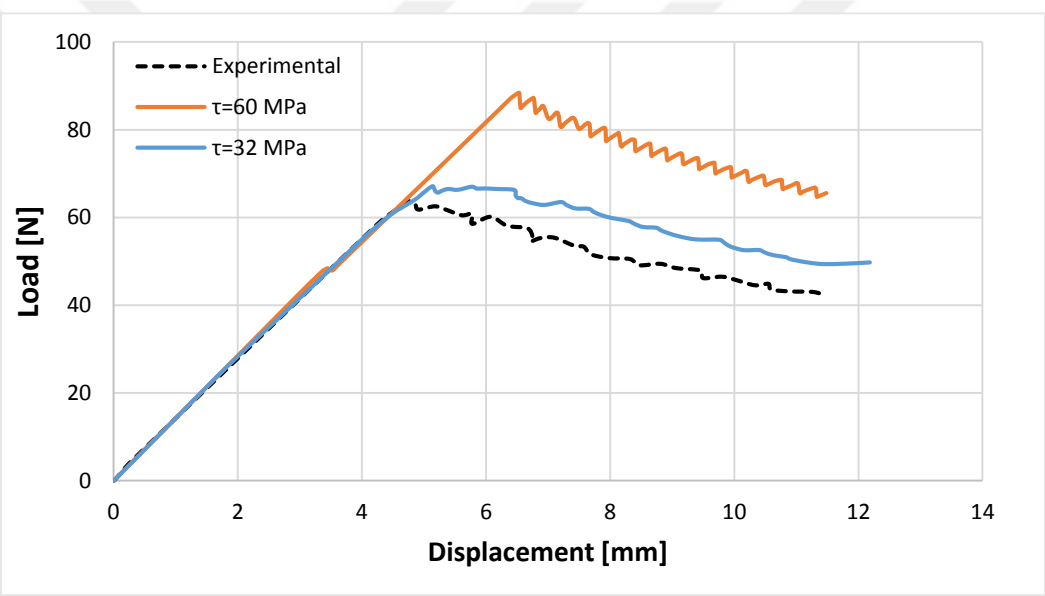

Figure 4.4. Load-displacement curve for DCB using reduced interface strength.

The difference between the experimental load-displacement curve and the predicted one in this approach is considered acceptable according to Turon *et al*. The value for α is 50 in these simulations. However α parameter can be altered since it controls the stiffness values. The maximum load can be reduced by using a smaller value for α and similarly it can be increased by a higher α.

4.1.1.2. 3D Solid Elements with Cohesive Surface Interaction. The 3D model for DCB has been created using solid elements (C3D8: an 8-node linear brick) with structured Hex mesh for two composite parts. The cohesive and damage behaviour is defined by implementing surface-to-surface contact between the two composite parts. The boundary conditions and the meshed assembly is illustrated in Figure 4.5.

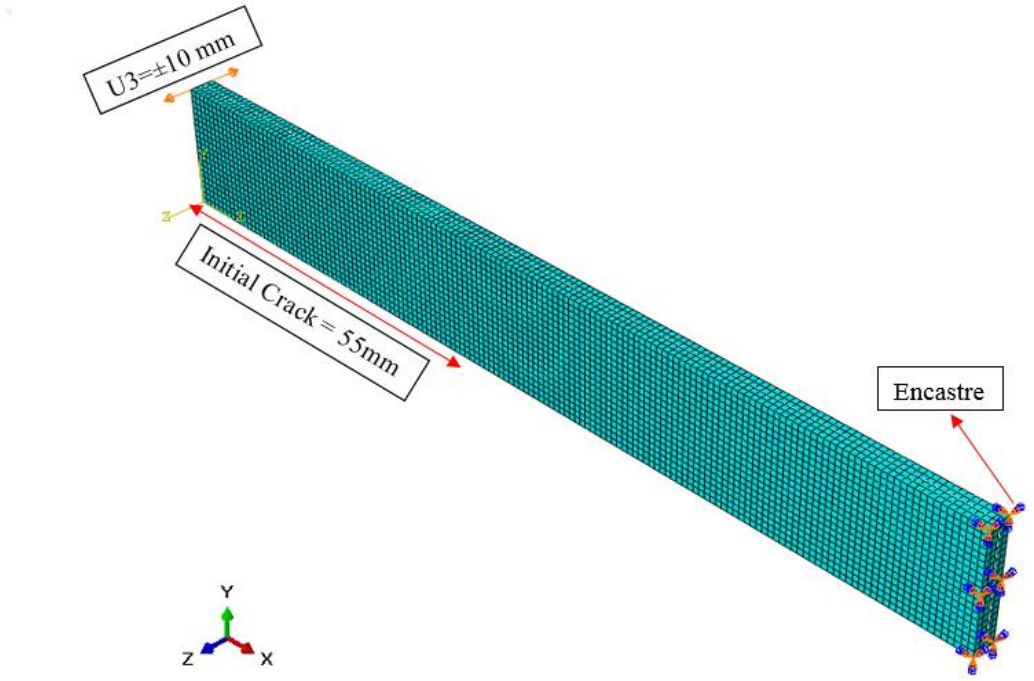

Figure 4.5. BC and mesh structure of 3D DCB model using solid elements and S2S cohesive contact.

The following figures (Figure 4.6-4.8) represent the deformed shape and stiffness degradation (SDEG) results implying the load drop in load-displacement curve and also the evolution behavior of delamination.

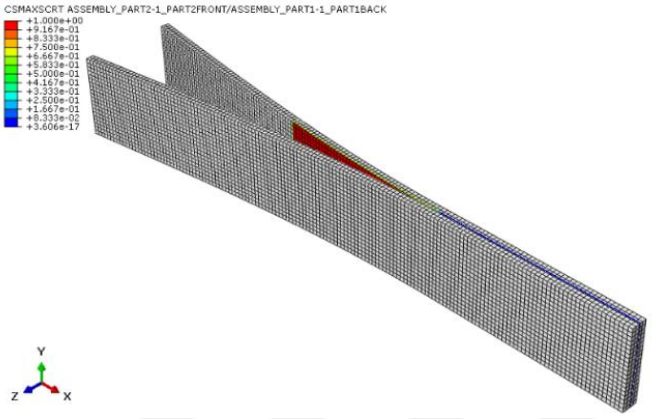

Figure 4.6. Deformed shape of 3D DCB model using solid elements and S2S cohesive interaction.

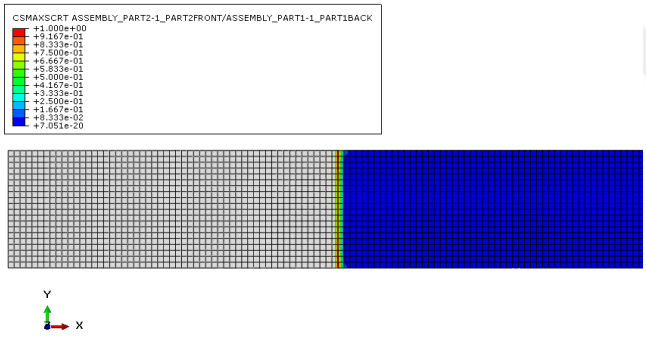

Figure 4.7. Delamination initiation of 3D DCB using solid elements and S2S cohesive interaction.

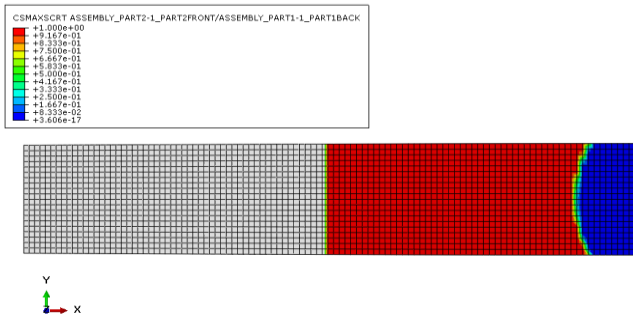

Figure 4.8. Delamination propagation of 3D DCB using solid elements S2S cohesive interaction.

4.1.1.3. Continuum Shell Elements with Cohesive Surface Interaction. The same model for 3D DCB has been investigated by replacing solid elements to continuum shell elements (SC8R) which are 8-node quadrilateral in-plane elements. The load-displacement curves obtained with these two 3D approaches have been compared with experimental and 2D model results in Figure 4.9. Stiffness parameter (K) in a continuum shell based model has been reduced to 100000 N/mm^3 in order to observe the peak load reduction. It can be observed that the 2-D model approximates to the experimental curve quite closely and the model using continuum shell elements provide acceptable predictions.

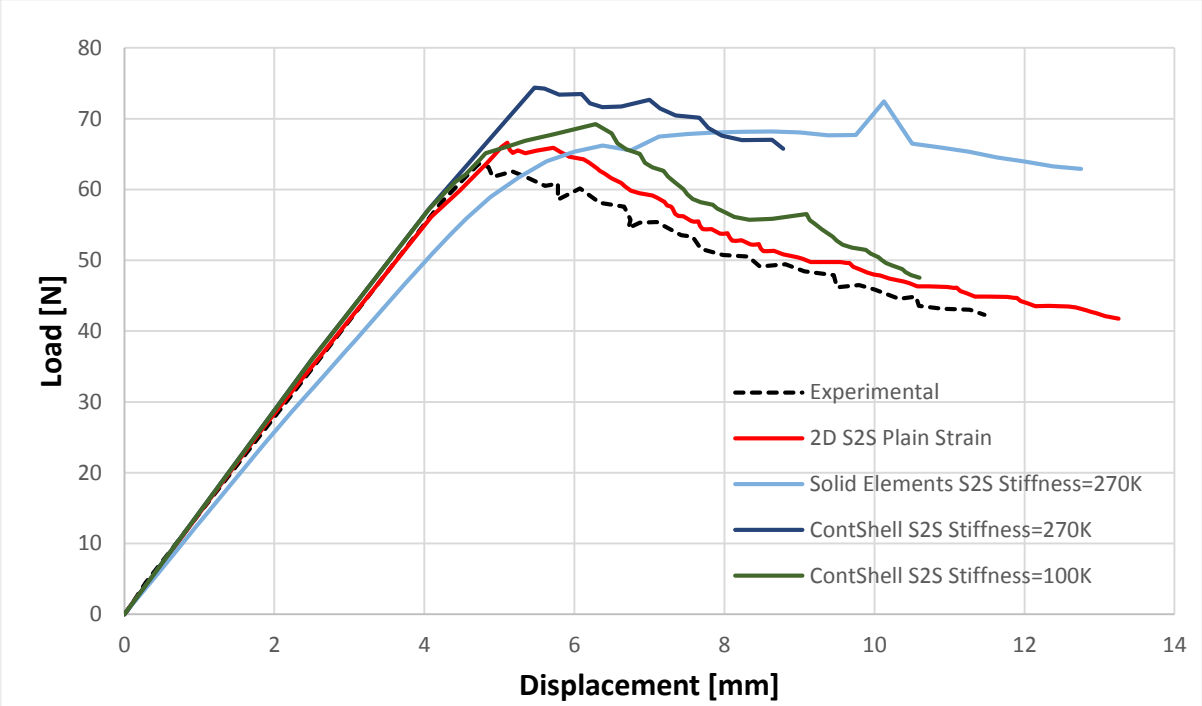

Figure 4.9. Load-displacement curves for various DCB models.

4.1.1.4. 3D DCB using Cohesive Elements method. The final model is based on cohesive elements rather than cohesive surfaces. The difference with the previous model is that only one deformable 3D extruded part is sketched including the initial crack and two composite

arms of the DCB specimen and a 0.001 mm thick cohesive section between the two to assign cohesive material properties later on. The other parameters such as meshing technique and boundary condition are the same. Stiffness degradation parameter SDEG is plotted in Figure 4.10 and Figure 4.11 for crack initiation and final state after crack propagation respectively. The red color refers to delamination, where the value of the SDEG parameter reaches to 1.

The load-displacement curves based on this approach and implementing solid elements and continuum shell elements in separate models for the composite part are compared with 2D approach and experiments in Figure 4.12. Using Cohesive zone elements and continuum shell elements to simulate the DCB test gives better results when compared to using solid elements or cohesive surface interaction

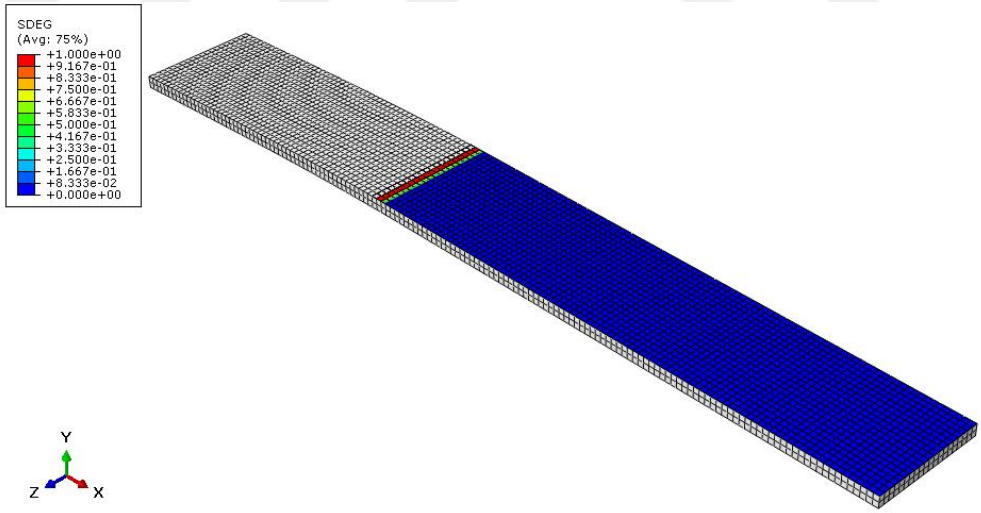

Figure 4.10. Delamination initiation of 3D DCB using continuum shell elements and cohesive elements.

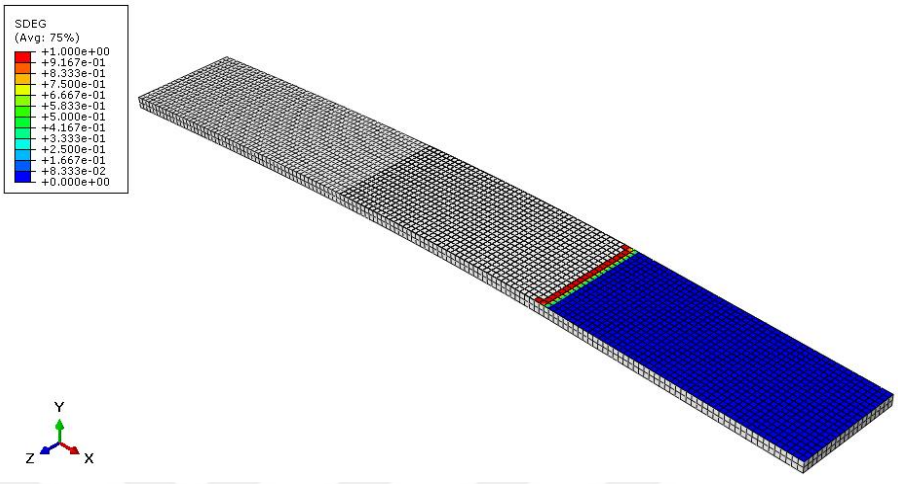

Figure 4.11. Delamination extension of 3D DCB using continuum shell elements and cohesive elements.

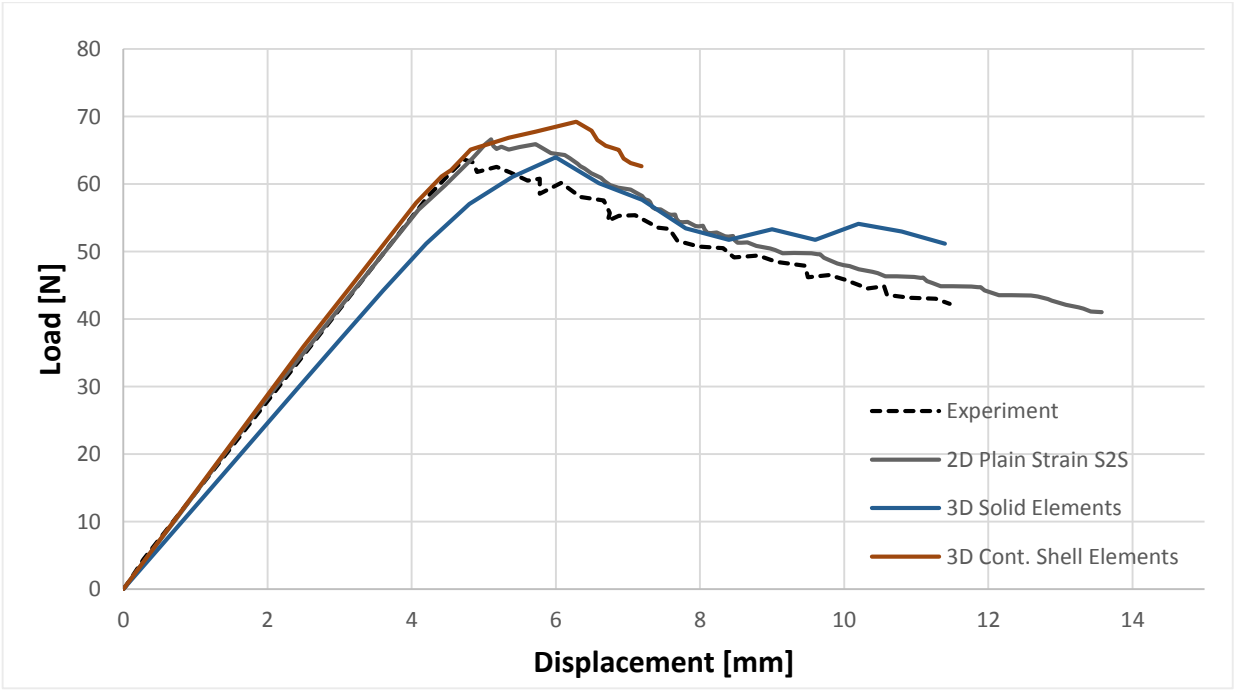

Figure 4.12. Load-displacement curves for DCB models using Cohesive Elements for delamination.

4.1.1.5. Experimental and Numerical Investigation of Mode I Fracture Toughness of AS4/8552. The Double Cantilever Beam (DCB) tests are performed according to the ASTM- D5528 test standard [64]. Then, the test results are compared with the 2D and the 3D Finite Element Model. AS4/8552 UD laminates are tested in this study. A 300 x 300 mm^2 plate consists of 20 plies and a Teflon insert between 10^{th} and 11^{th} plies are manufactured according to the Manufacturer's Recommended Cure Cycle (MRCC) in the autoclave. Then the plate is cut with a water-cooled diamond saw into desired specimen dimensions. Test setup and specimen configuration are shown in Figure 4.13 and Figure 4.14.

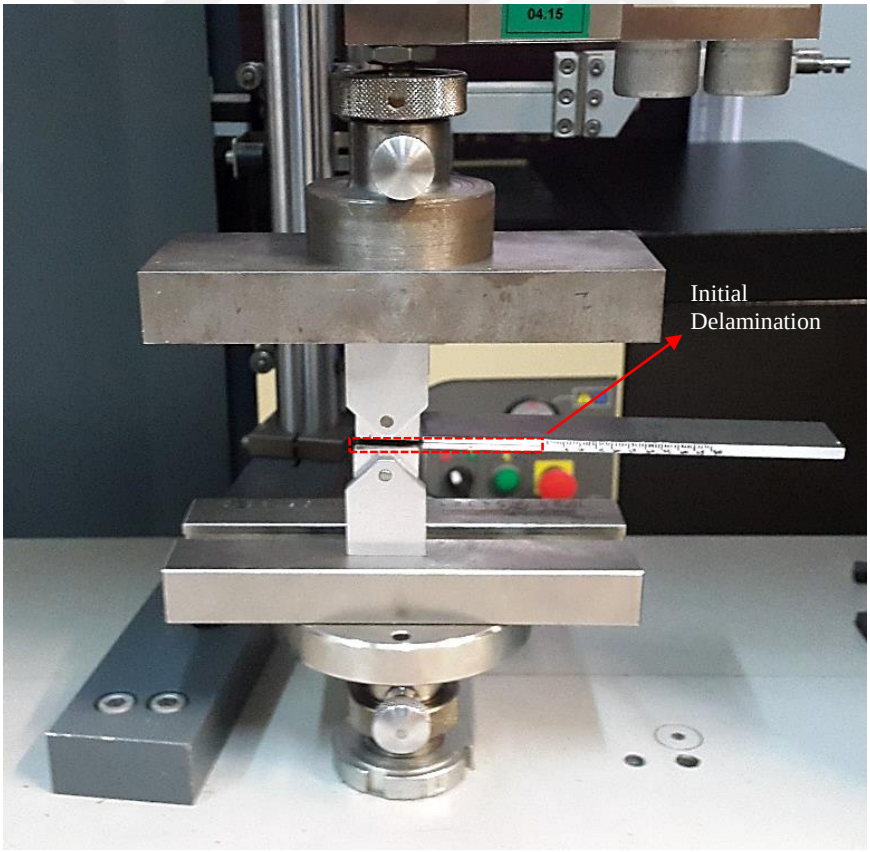

Figure 4.13. DCB Test setup.

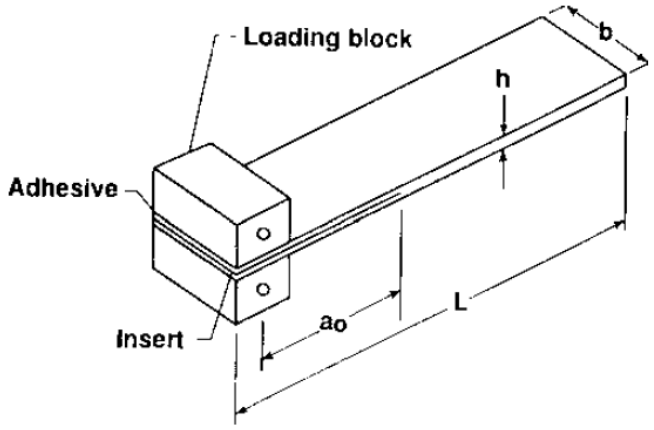

Figure 4.14. DCB specimen with loading blocks [64].

Where a_0 is the initial delamination length, b is the width, h is the thickness and L is the length of the DCB specimen. Modified Beam Theory (MBT) and a Modified Compliance Calibration method (MCC) can be used to calculate interlaminar fracture toughness as given in Equation 4.2 and Equation 4.3, respectively:

$$G_I = \frac{3P\delta}{2ba} \tag{4.3}$$

Where P is the applied load, δ is load point displacement and a is defined as delamination length.

$$G_I = \frac{3P^2C^{2/3}}{2A_1bh} \tag{4.4}$$

Where C is the compliance (δ/ P), of DCB specimen and A_1 is the slope in the plot of a/b versus $C^{1/3}$. The Mode I fracture toughness results with using these two equations and obtained load-displacement results for three tested specimens are given in Table 4.1. Figure 4.15 represents the load-displacement responses of the experimental tests and 2D and 3D FEM models.

Table 4.1. Experimental results with calculated Mode I fracture toughnesses.

	Width (mm)	**Thickness (mm)**	**Max. Load (N)**	**Disp. at Max Load (mm)**	**K (N/mm)**	**C (mm/N)**	**G_{Ic} (MBT)**	**G_{Ic} (MCC)**
Sp1	24.25	3.50	60.56	3.46	14.98	6.6773E-02	0.26	0.30
Sp2	24.25	3.68	53.27	4.32	10.69	9.3449E-02	0.28	0.28
Sp3	24.50	3.54	51.64	3.80	12.23	8.1705E-02	0.24	0.25
Avg.							0.26	0.28
								$G_{Ic : (KJ/m^2)}$

The same 2D and 3D FE models used in benchmarking study in ABAQUS/Implicit are customized for AS4/8552 with using G_{Ic}=0.28 KJ/m^2 and material properties are given in Table 3.1. Composite layers are meshed with SC8R Continuum shell elements, while a 0.001 mm-thick cohesive layer between two composite arms, and meshed with COH3D8 elements. The number of elements in the cohesive zone is considered to be 4. The upper and lower rollers are defined as 3D discrete rigid parts as done in benchmarking study. A similar element size effect investigation has been carried out for AS4/8552 material. In order to reduce computational time without sacrificing accuracy of the results, element size of 1mm with reduced interfacial strength by using Equation 4.2 (= 25.8 MPa) has been selected according to the compared results shown in Figure 4.15.

In this section, in order to assign coarser meshes in modelling Mode I delamination behaviour of AS4/8552 carbon-epoxy laminates, an approach based on an artificial increase of the cohesive zone length by lowering the interfacial strength is followed. The DCB tests are performed experimentally to obtain the load-displacement curves and to evaluate the Mode I interlaminar fracture toughness value. Moreover, 2D and 3D numerical models are applied to simulate DCB test in ABAQUS. A parametric study is carried out for both models to investigate the effect of various cohesive parameters. The accuracy of the results shows

that propagation of delamination can be accurately predicted with a coarse mesh using this computational-time-friendly approach.

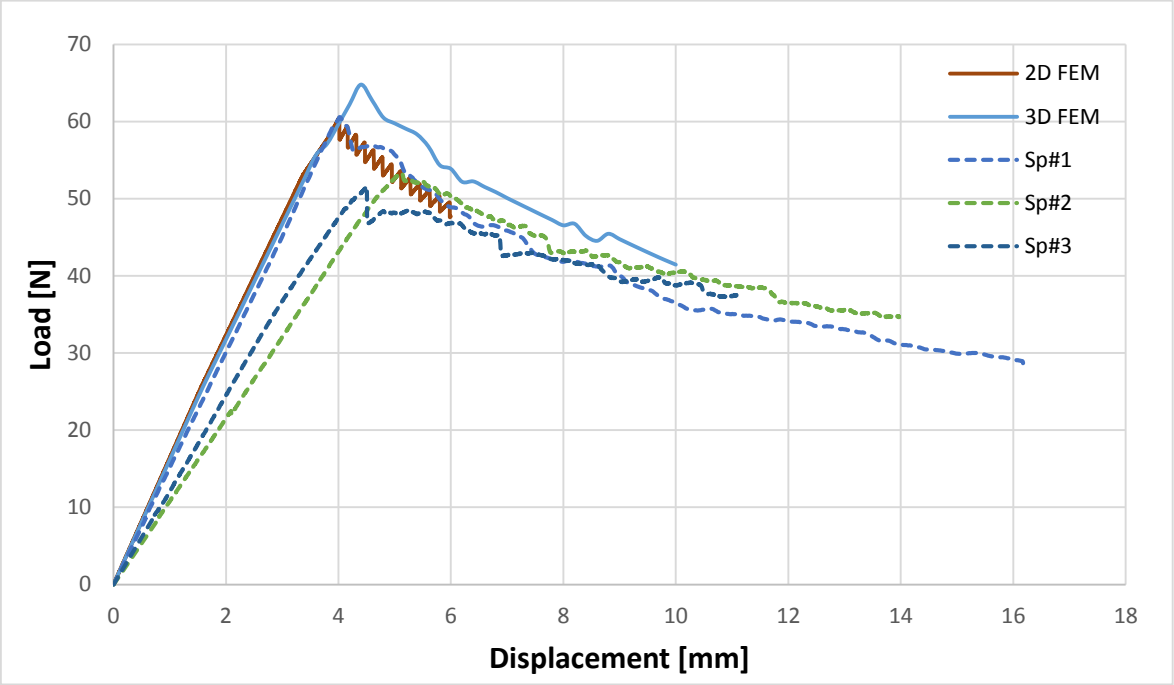

Figure 4.15. Load-displacement responses of experimental tests, 2D and 3D FEM models.

4.2. End-Notch Flexure Experimental and Numerical Analysis

4.2.1. Introduction

End Notched Flexure (ENF) tests are performed according to ASTM D7905 test standard [65]. Then, test results are compared with cited values in the literature [58] and the Finite Element Model.

4.2.2. Material and Test Specimens

AS4/8552 UD laminates are tested in this study. A 300 x 300 mm^2 plate consists of 20 plies and a Teflon insert between 10^{th} and 11^{th} plies are manufactured according to the Manufacturer's Recommended Cure Cycle (MRCC) in the autoclave. Then the plate is cut with a water-cooled diamond saw into desired specimen dimensions. Specimen configuration with dimensions are shown in Table 4.2.

Table 4.2. Specimen configuration and dimensions.

Specimens	Width (mm)	t (mm)	L (mm)	L_C (mm)	L_U (mm)	a_0 (mm)
1	24.45	3.68	50	20	20	30
2	24.50	3.68	50	20	20	30
3	24.75	3.68	50	20	20	30
4	24.55	3.70	50	20	20	30
5	24.45	3.68	50	20	20	30
6	24.50	3.75	50	20	50	30
7	24.60	3.70	50	20	50	30

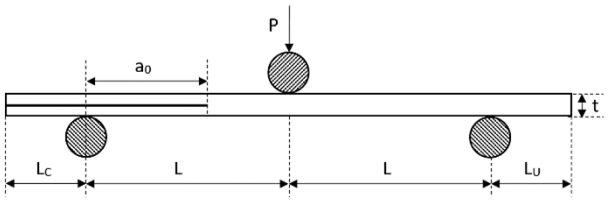

4.2.3. Experimental Procedure

Acoustic emission (AE) registration and Digital Image Correlation (DIC) measurement are applied simultaneously during ENF test. However, DIC results are not presented in this report. Test setup in this study can be seen in Figure 4.16. Seven tests are performed. AE and DIC measurement are used in four of them.

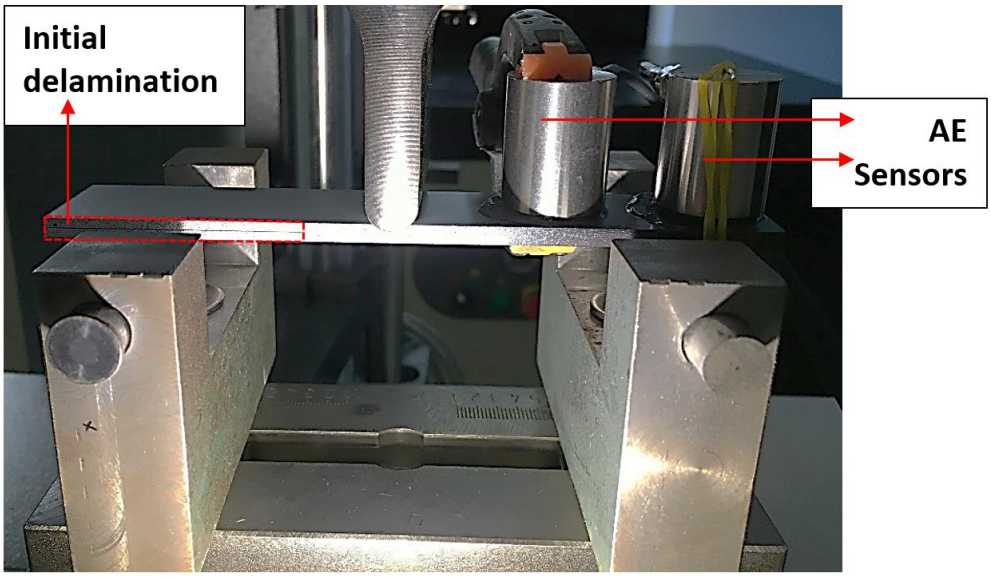

Figure 4.16. ENF Test setup.

Equations 4.5-4.7 are used to calculate Mode-II fracture toughness values of AS4/8552, which are then compared with the values in literature and the prediction from a Finite Element Model. Equation 4.5 gives the Mode-II fracture toughness which can be rearranged to Eq. 4.6 using the compliance function *C* which is expressed in Equation 4.7 as a function of the crack length a. The coefficient "*m*" for Equation 4.4 can be calculated as follows: Compliance is calculated from the slope of the load-displacement curve for different initial delamination length between the spans (a_0). Normally, tests are performed for a_0=30 mm. First, the specimens are loaded until load level lower than the maximum load for a_0=20 mm, then the same loading is applied for a_0=40 mm and finally, the specimen is loaded until maximum load for a_0=30 mm.

A linear regression line is calculated for compliance and cubic power of three different a_0 values to obtain coefficient "*m*". The MISTRAS AE system with PAC AEwin software are used for AE registration. Broadband PK-WDI sensors are used placed on one side of the specimen with a spring clamp and rubber bands. It is used to identify damage modes but AE results are not presented in details within this report.

$$G_{IIc} = 9\frac{(P_c \cdot a_0)^2}{(2 \cdot B)}\left(\frac{C}{2L^3 + 3{a_0}^3}\right) \tag{4.5}$$

$$G_{IIc} = 3 \cdot m\frac{(P_c \cdot a_0)^2}{(2 \cdot B)} \tag{4.6}$$

$$C = A + m(a_0)^3 \ \ (mm/N) \tag{4.7}$$

Where G_{IIC} is the mode-II fracture toughness, P_c is the maximum load reached during the test, a_0 is the initial delamination length between spans, B is the specimen width, L is the half of distance between support spans, C is the Compliance, and A is a constant defined as:

$$A = \frac{2}{3}m(L)^3 \tag{4.8}$$

4.2.4. Finite Element Model

The finite element model is created and analyzed using ABAQUS/Implicit. Composite layers are meshed with SC8R Continuum shell elements, while a 0.001 mm-thick cohesive layer is implemented between two composite arms with four elements in the cohesive zone, and meshed with COH3D8 elements. The upper and lower rollers are defined as 3D discrete rigid parts, and as final assembly, the displacement boundary condition is assigned to the upper roller. The material properties for both composite and cohesive elements are given in Table 4.3 and Table 4.4. The schematic details of the finite element model can be seen in Figure 4.17.

Table 4.3. Material parameters for UD composite.

E_1 (GPa)	E_2 (GPa)	G_{12} (GPa)	G_{23} (GPa)	ν_{12}	ν_{23}
142.84	10	5.571	3.278	0.263	0.525

Table 4.4. Interlaminar strength, fracture energy and stiffness parameters for cohesive elements.

σ_{33c} (MPa)	σ_{13c} (MPa)	G_{Ic} (KJ/m^2)	G_{IIc} (KJ/m^2)	K_{nn} (N/mm^3)	K_{ss} (N/mm^3)
81	114	0.28	2.59	2.72E+006	2.72E+006

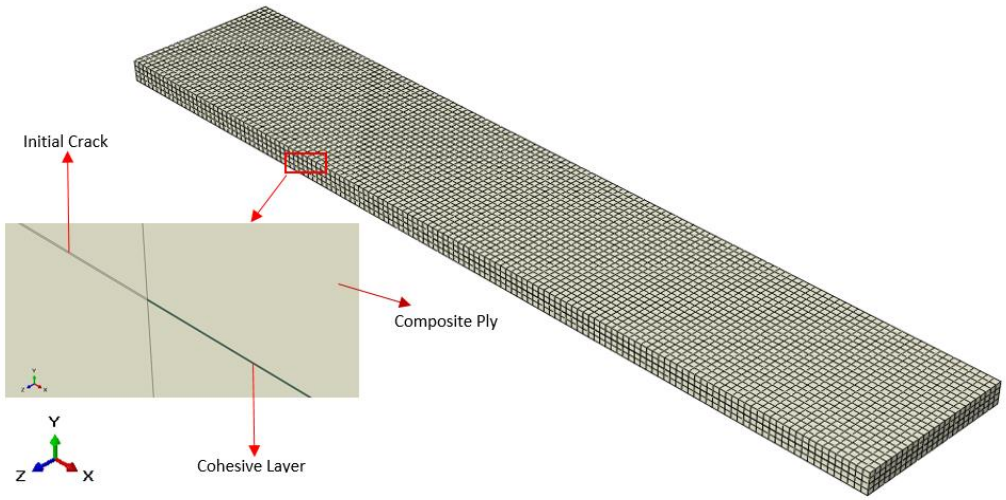

Figure 4.17. Finite Element model of ENF specimen.

As expected and compared to the experimental tests, the initial crack will propagate between the top and bottom composite plies. Extension behavior of stiffness degradation in cohesive elements is represented in Figure 4.18 and Figure 4.19.

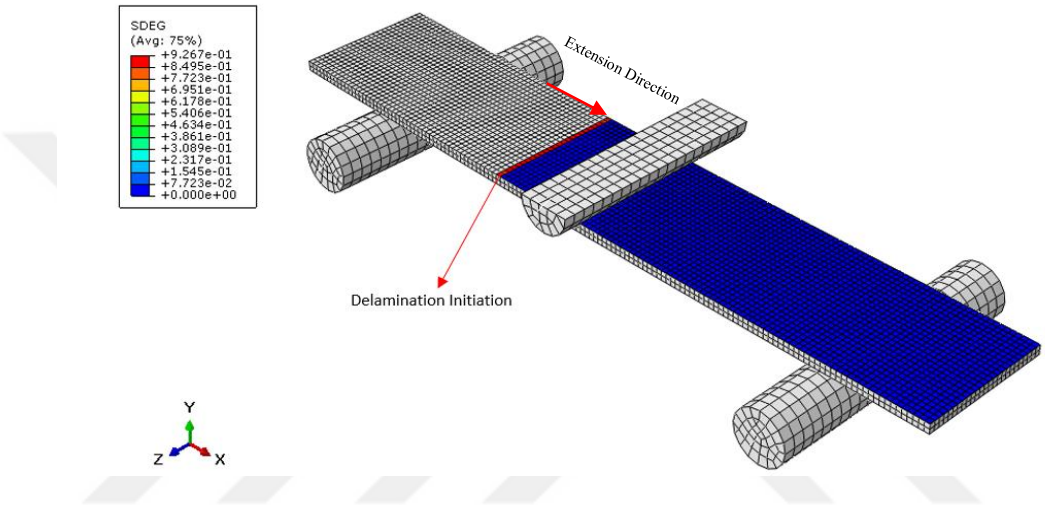

Figure 4.18. Delamination initiation and stiffness degradation (SDEG) in cohesive layer.

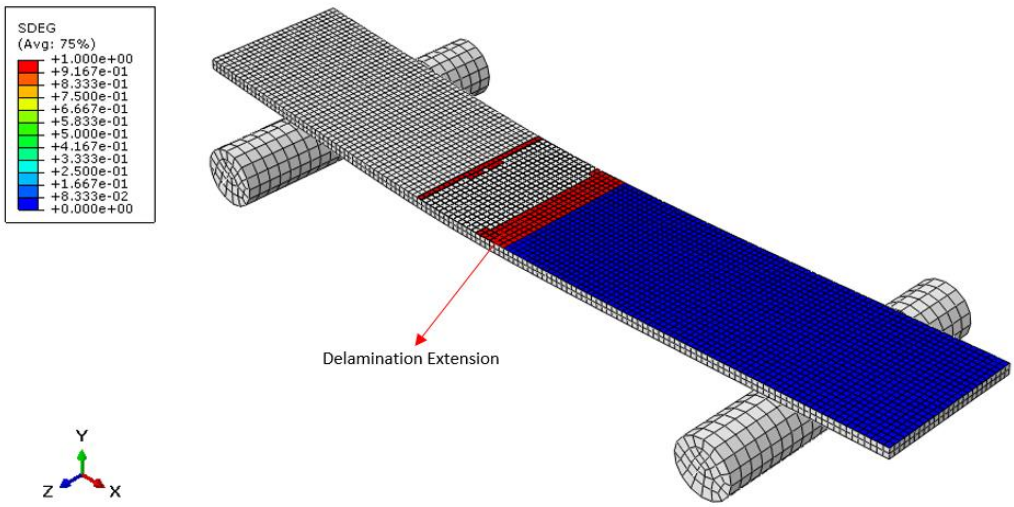

Figure 4.19. Delamination evolution and stiffness degradation (SDEG) in cohesive layer (the upper roller is removed from the viewport in order to show the extension clearly).

The deformation behavior (slipping of the upper composite arm) of the specimen at the failure stage is shown in Figure 4.20.

.

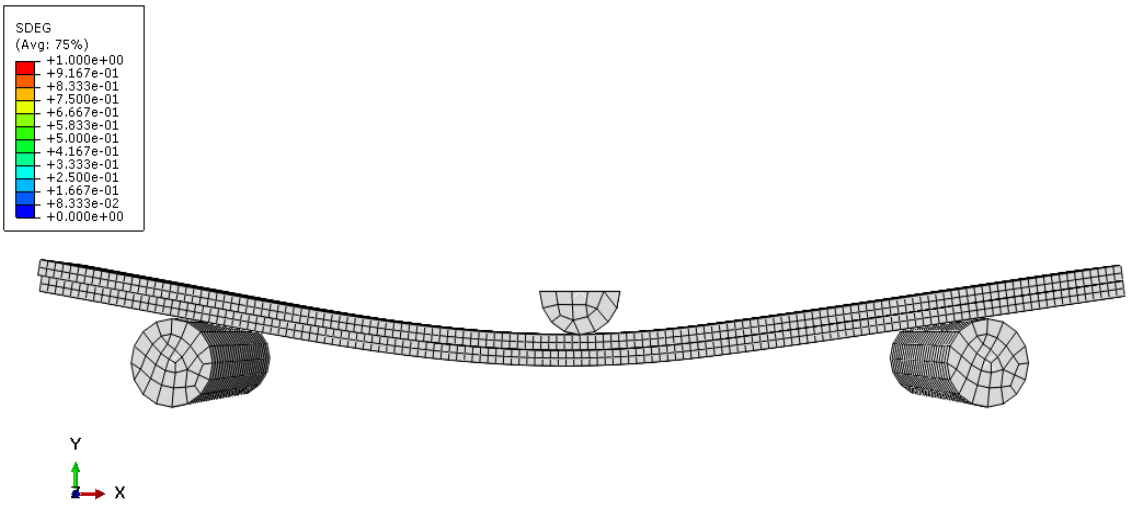

Figure 4.20. Behavior of the upper composite arm and stiffness degradation (SDEG) in cohesive elements.

4.2.5. ENF Test Results

Load-displacement responses and cumulative AE energy curves of ENF tests are shown in Figure 4.21. The load drops in the load-displacement curves are accompanied by a large jump in cumulative AE energy. Maximum load and deflections are given in Table 4.5. ENF . It should be mentioned that "*m*" coefficient is not measured for the first four tests. Each m value for these results is actually the average value of other tests (tests of specimens 5, 6 and 7). There is a great consistency between load-displacement response and AE results in Figure 4.21 and the results in Table 4.5. Only the results of the first specimen are not close to average values. Its maximum load, displacement and G_{IIc} values are higher than other specimens. If the result of the first specimen is extracted then the average value of G_{IIc} becomes equal to 2.50 (kJ/m^2). Standard deviation reduces to 7 %.

The cumulative AE energy curves in Figure 4.21 emphasizes that there are micro cracks initiating after 3 mm displacement which propagates and causes a sudden failure at the end section of initial delamination.

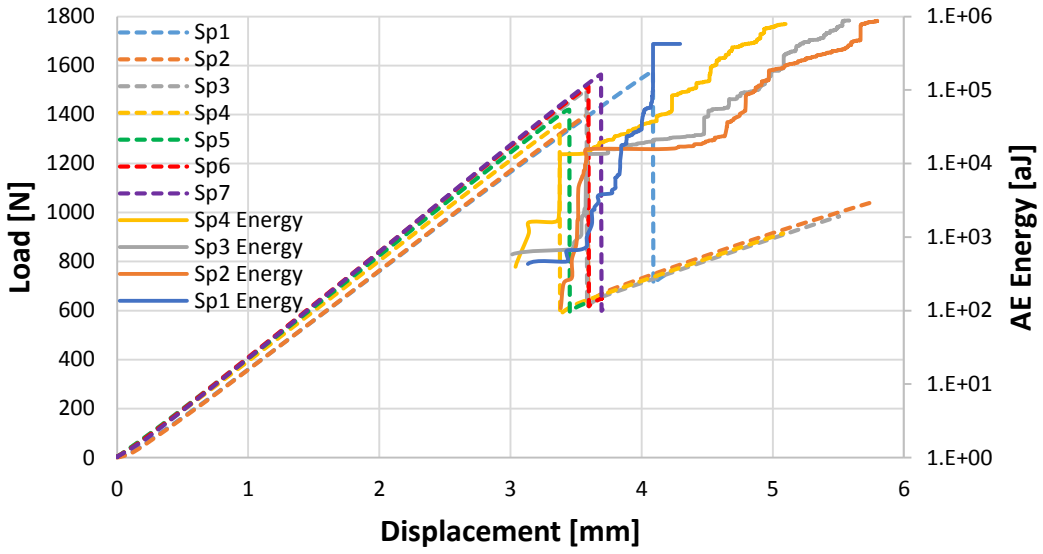

Figure 4.21. Load-displacement responses and cumulative AE energy curves of ENF specimens.

Table 4.6 compares the test results with a previous study [58] in which different test methods are used to evaluate G_{IIc}. Test result in this report is exactly two times higher than the reference value. Its main reason is the maximum load reached during the tests. All the parameters in this study are similar to the ones in [58]. The only difference is maximum loads. They are around 1000 MPa as seen in Figure 4.21, whereas the average value of maximum load in this study is 1476 N as shown in Table 4.6. Since the square of the load is involved to calculate G_{IIc} in Equation 4.5 and Equation 4.6, the G_{IIc} value becomes two times higher than the reference [58].

Table 4.5. ENF test results.

Sp.	Max. Load (N)	Max. Disp (mm)	K (N/mm)	C (mm/N)	m (1//N mm^2)	G_{IIc} (Eq. 4.5)	G_{IIc} (Eq. 4.6)
1	1578.16	4.09	398.76	2.5075E-03	2.0885E-08	3.13	3.05
2	1400.66	3.59	404.25	2.4736E-03	2.0885E-08	2.42	2.40
3	1498.74	3.58	424.46	2.3559E-03	2.0885E-08	2.62	2.72
4	1359.46	3.37	408.72	2.4466E-03	2.0885E-08	2.25	2.25
5	1420.38	3.45	418.90	2.3004E-03	2.2164E-08	2.32	2.47
6	1515.06	3.59	429.63	2.2971E-03	2.1255E-08	2.63	2.69
7	1563.30	3.69	433.57	2.2795E-03	1.9236E-08	2.77	2.58
Avg.	1476.54	3.62	416.90	2.3801E-03	2.0885E-08	2.59	2.59
STD (%)	5.70	6.34	3.18	3.96	4.14	11.51	9.98
G_{IIc} : (kJ/m^2)							

Table 4.6. Comparison of test results with a previous study using different methods for evaluation of $G_{IIc.}$

	Max. Load (N)	Max. Disp (mm)	K (N/mm)	C (mm/N)	m (1//N mm^2)	G_{IIc} (Eq1)	G_{IIc} (Eq2)
Exp.	1476.54	3.62	416.90	2.3801E-03	2.0885E-08	2.59	2.59
[58]	1004.42	2.62	418.48	2.3960E-03	2.0900E-08	1.14	1.15
Average thickness, width and initial delamination length of specimens in [58]: t =3.70 mm B = 25.48 mm a_0 = 30.48 mm							

4.2.6. Comparison with Finite Element Model

Figure 4.22 represents the Load-Displacement responses of the experimental tests and two FEM models. The FEM 1 is carried out by using the G_{IIc} value from experimental tests (2.59 kJ/m^2). The FEM 2 is based on the G_{IIc} parameter in [58] which equals to 1.14 kJ/m^2. In both cases, the number of elements in the cohesive zone is considered to be 4. Assigning element size of 1 mm will require a reduction in interfacial strengths by using Equation 4.2 in order to accurately capture the delamination. However, in order to investigate the mesh dependency of the FE model, simulations are also carried out by using material's own interface strengths with different mesh sizes. It is observed that using 1 mm mesh in conjunction with reduced strengths is in an acceptable agreement with experimental results and is considerably time efficient when compared to using 0.5 mm mesh size. This comparison, shown in Figure 4.24, is brought after a modification in elastic modulus which will be discussed later in this section.

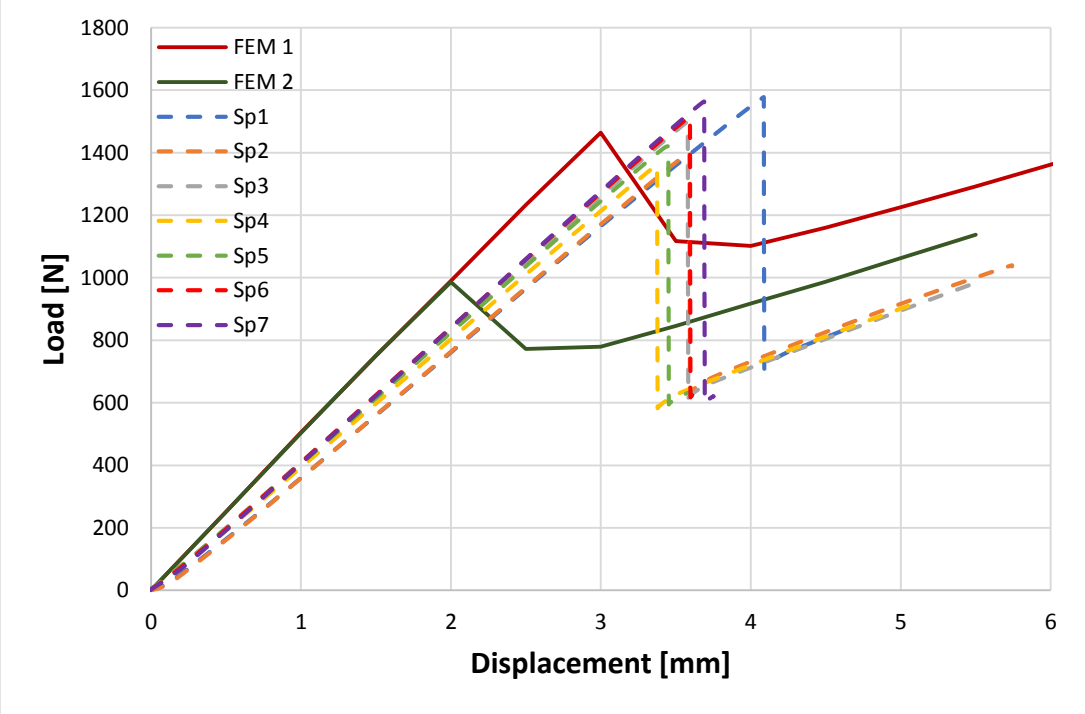

Figure 4.22. FEM and experimental load-displacement responses of ENF specimens.

Table 4.7 shows that the maximum loads extracted from two FEM are in good correlation with experimental and represented results in [58], however, the slope of the load-displacement curve and sudden load drop after initial failure is not captured in the FEA model.

Table 4.7. ENF FE results.

	Max. Load (N)	**Max. Disp (mm)**	**K (N/mm)**
FEM 1	1464.16	3	501.58
FEM 2	986.37	2	502.48

According to experimental investigations of Mujika *et al*. [66] regarding flexural modulus of AS4/8552, the designated value for E_1 is considered to be 131200 MPa. The result of this modification (FEM 3) is compared to the previous (FEM 1) result and the experiments in Figure 4.23 and Table 4.8.

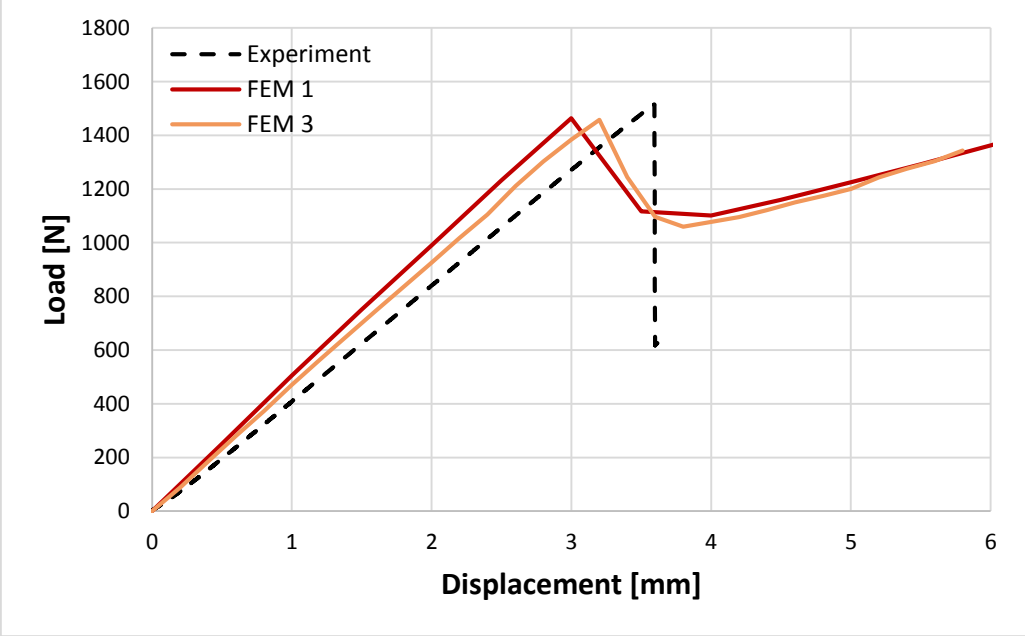

Figure 4.23. FEM 3 and experimental load-displacement responses of ENF specimens.

Table 4.8. FE/Experiments test results.

	Max. Load (N)	Max. Disp (mm)	K (N/mm)
FEM 3	1458.06	3.20	439.30
Experiment	1476.54	3.62	416.90

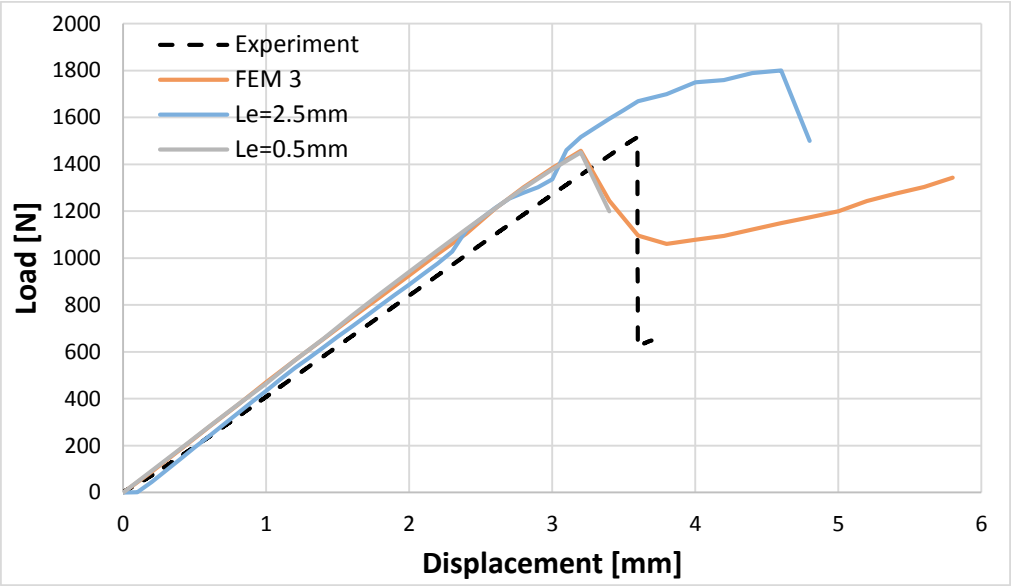

Figure 4.24. Effect of mesh size in 3D ENF model.

5. FINITE ELEMENT MODELING OF OHT COMPOSITES

For numerical analysis of progressive failure in OHT composite laminates, capabilities of the ABAQUS/Standard finite element software package is explored. The OHT specimen configuration used in this study is prepared according to the ASTM D5766 [62] test standard and is demonstrated in Figure 5.1. Note that the gripping region is not considered in the proposed model. A 3D deformable solid extruded part is created with a thickness of $1.479mm$ including $0.184mm$ thick composite plies and $0.001mm$ thick cohesive layers ($8 * 0.184mm + 7 * 0.001mm$). The sketched part is then partitioned into 8 composite plies with 7 cohesive plies in between. To improve convergence, accuracy and efficiency in composite material simulations Autodesk® Helius PFA plug-in for ABAQUS has been used to create composite and cohesive materials. Helius PFA for ABAQUS is implemented via the user subroutines UMAT, VUMAT, URDFIL, and UEXTERNALDB and is defined via an ABAQUS user material. Composite plies are defined to the partitions by assigning Composite Layup with Continuum Shell element type option in part module. Previously mentioned cohesive properties have been applied to the partitioned cohesive layers in Section Assignment with using Traction Separation response. Constitutive thickness for the cohesive elements is chosen to be considered the same as the geometric thickness.

An implicit step (static general) with the time period of 1 second is generated for the analysis. To include nonlinear effects of large deformations and displacements, non-linear geometry option (NLGEOM) is turned on in the step module. An automatic time incrementation with initial increment size of 0.01 is applied, where the size of subsequent increments will be adjusted based on how quickly the analysis converges. Choosing fixed time incrementation is not recommended due to the possibility of causing convergence problems [67]. The General Solution Controls Editor for the step allows the modification of convergence algorithms and accuracy of time integration.

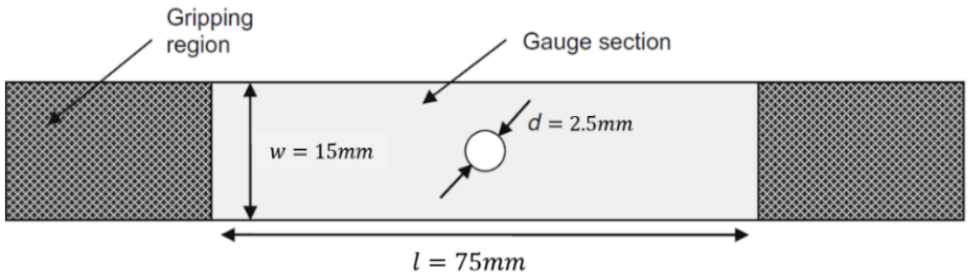

Figure 5.1. Specimen configuration.

The time incrementation control parameters that have been modified from their default values include I_0, number of first equilibrium iterations for consecutive divergence check, I_R, number of equilibrium iterations at which logarithmic convergence rate check begins, I_P, number of iterations after which alternative residual tolerance is used, I_C, maximum number of consecutive equilibrium iterations that is allowed and I_L, which is the equilibrium iteration count for a cut-back in the next increment. The customized values for these parameters have been increased to 1000 and the value for I_C, indicating the maximum cut-backs allowed in an increment, is considered to be 20 [68].

The whole part is meshed with hexahedral elements using swept meshing technique. The Medial Axis Algorithm is preferred to minimize the mesh transition and distortion. Due to the distinctive directional behaviour of continuum shell and cohesive elements, a through the thickness mesh stack direction should be assigned to the part in the mesh module. Figure 5.2 shows the partitions and the mesh structure in this analysis.

Continuum shell elements (SC8R) with linear geometric order and enhanced hourglass control and cohesive elements (COH3D8) are selected as element types for modeling composite plies and cohesive layers respectively. The element deletion option is activated in assigning the element types.

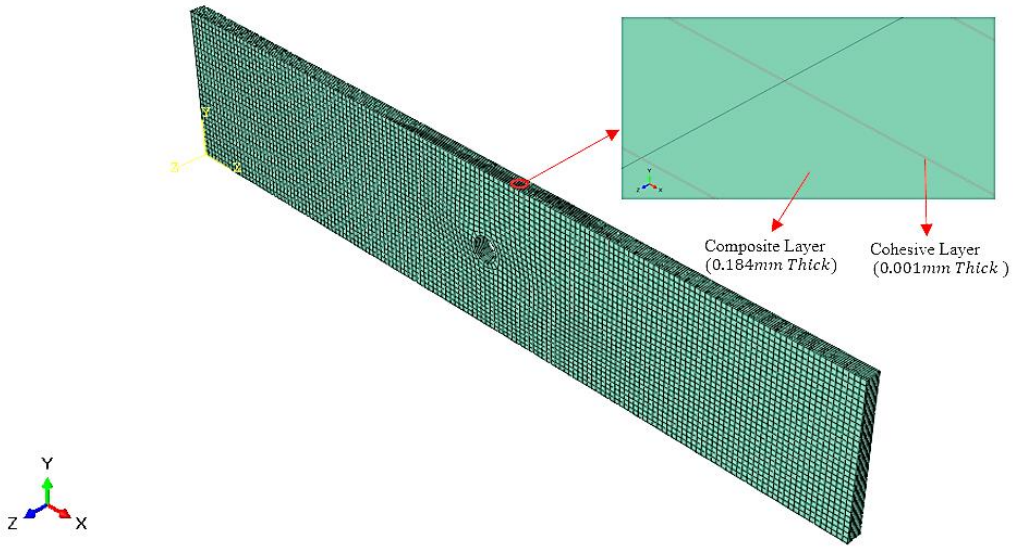

Figure 5.2. Partitions and mesh structure.

A nodal displacement with a tabular amplitude is applied to the tip node, which is connected to all the nodes on the right edge surface of the specimen with using an equation type constraint. This constraint and assigned boundary conditions are represented in Figure 5.3 and Figure 5.4 respectively.

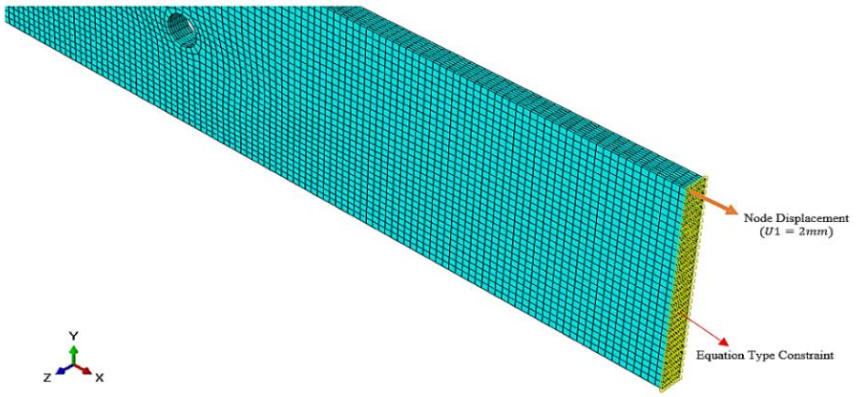

Figure 5.3. Constraint between loading point-loading surface and the applied nodal displacement.

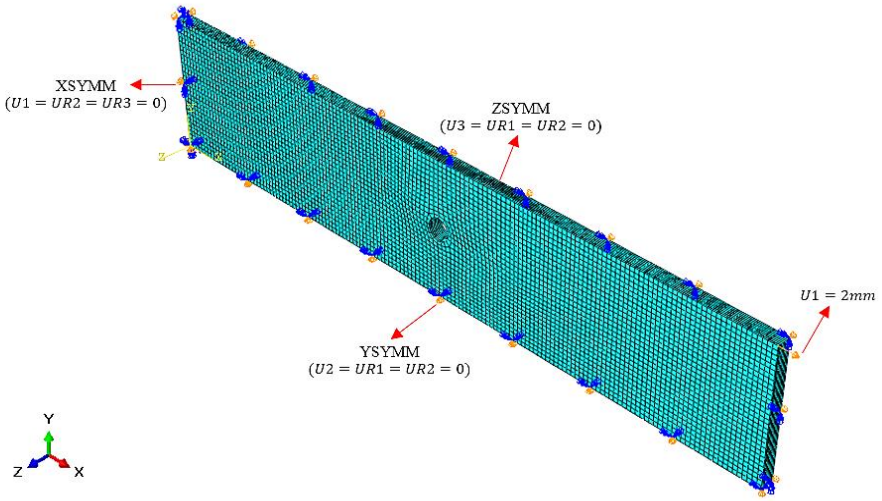

Figure 5.4. Boundary conditions used for the OHT analysis.

To view the results of progressive failure analysis in composites, field output variables should be requested. The number of Solution Dependent MCT (Multi Continuum Theory) State Variables (SDVs), which track the constitutive values for each integration point within each element, is specified by the *DEPVAR keyword. The number of SDVs in ABAQUS/Standard with using instantaneous degradation for unidirectional composites is 7. The default naming convention for state variables is SDVi, where $\mathrm{i} = 1, 2, 3, \ldots, 7, 11, 13, 17, 35,$ or 90. The most fundamental state variable is SDV1 that represents the discrete damage state of the composite material. It assumes a finite number of discrete values between 1 and 3. Table 5.1 provides the interpretation for each allowable discrete value of SDV1 for each possible combination of discrete composite damage state.

Table 5.1. Interpretation of discrete SDV1 values and specified damage state.

Allowable Discrete Values for SDV1	**Composite Damage State**
1	Undamaged Matrix, Undamaged Fiber
2	Failed Matrix, Undamaged Fiber
3	Failed Matrix, Failed Fiber

By default, the state variables are not automatically written to the output database file (*.odb file) and must be explicitly requested which can be accomplished by activating output variable labeled as "SDV, Solution Dependent State Variables" in the field output request section. In addition, the number of the section points where the output variables are calculated should be specified. In a model containing multiple material layers, the default section points only correspond to the top and bottom surfaces. Therefore, the output variables are not available for any of the internal material layers. If the output is requested for each section point, the complete results can be viewed for every single ply. For unidirectional composite materials, state variable SDV2 is a continuous real variable that varies from 0.0 to 1.0 and is used to indicate the fraction of the matrix failure criterion that has been satisfied. For instance, SDV2 = 0.0 denotes that the matrix stress state is zero, while SDV2=1.0 implies that the matrix stress state has reached failure level. Similarly, SDV3 which ranges from 0.0 to 1.0 indicates the fraction of the fiber failure criterion that has been satisfied. The interpretation of other SDVs for unidirectional composites are not mentioned here since they are not analyzed in this study [69].

The number of required state variables for Helius PFA cohesive materials is 9. However, only 3 variables are discussed in the results section. SDV 1 is the current damage state and will be an integer between 0 and 26. A value of zero indicates that the damage has not initiated yet and value of 26 implies the complete failure (zero stiffness). Any other value indicates how much damage has been incurred. This state variable is used mainly as a tracking device for Helius PFA. In order to observe damage, it is recommended to view SDV6, which ranges from 0 to 1 and indicates how much damage has occurred. A value of 1 represents a fully damaged material and consequently zero stiffness. SDV2 indicates how much of the damage initiation criterion has been met. A value of 0 indicates no loads are acting upon the integration point and therefore are not satisfying the damage initiation criterion. A value of 1 states that the damage has initiated and the stiffness is reducing [70]. The ultimate damage state in the half-model using the mid-plane as the plane of symmetry, and for all the composite plies and cohesive layers are demonstrated in Figure 5.5 and Table 5.2, respectively.

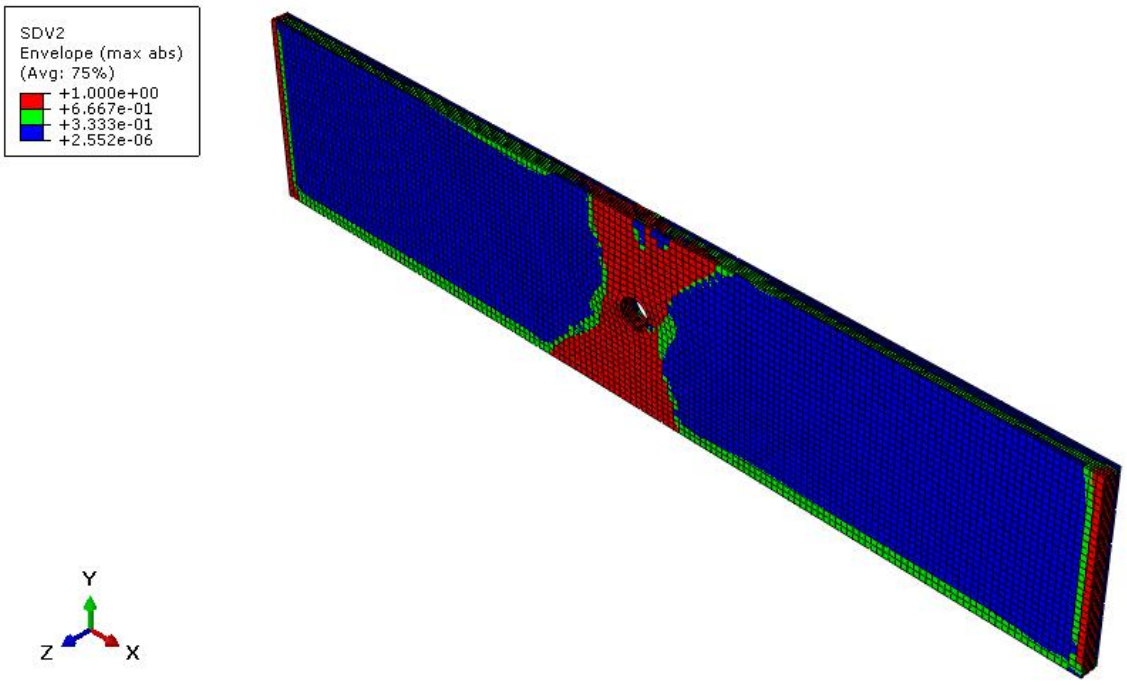

Figure 5.5. Final damage state in $[-45_2/0_2/45_2/90_2]_s$ OHT half-model.

Table 5.2. Final damage state in composite plies and cohesive layers.

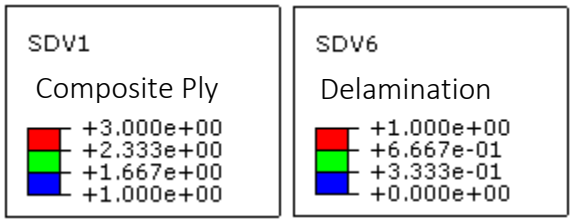

+45°	**+45°/+45°**	**+45°**
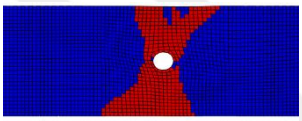	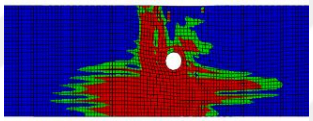	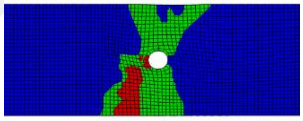
+45°/90°	**90°**	**90°/90°**
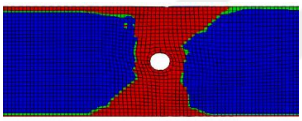	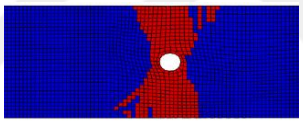	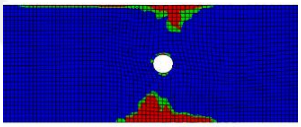
90°	**90°/-45°**	**-45°**
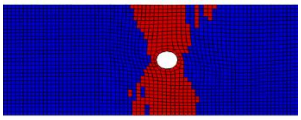	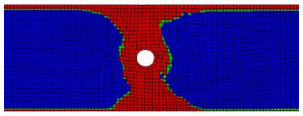	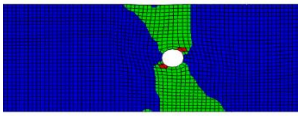
-45°/-45°	**-45°**	**-45°/0°**
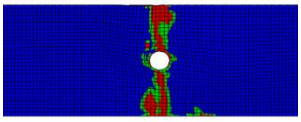	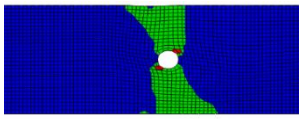	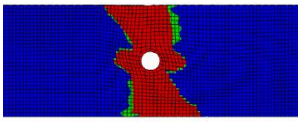
0°	**0°/0°**	**0°**
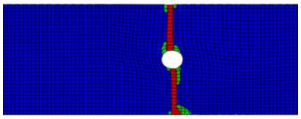	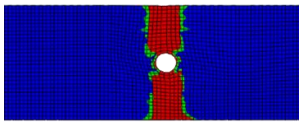	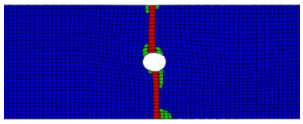

6. EXPERIMENTAL DAMAGE MODE IDENTIFICATION IN OHT LAMINATES

This section covers the tension test results of OHT specimens which are performed according to ASTM D5766 [62] standard. The tests are performed under displacement control and AE sensors are attached to the specimen to acquire Acoustic Emission signals. The test rate is 1mm/min. The tension tests are conducted in KU Leuven with electro-mechanical Instron 4505 test device. DIC technique using VIC 2D software has been optically applied for extensometry measurements. A second camera with a higher resolution is used to capture micro-damage progression on the edges of the specimens. This experimental test setup is shown in Figure 6.1.

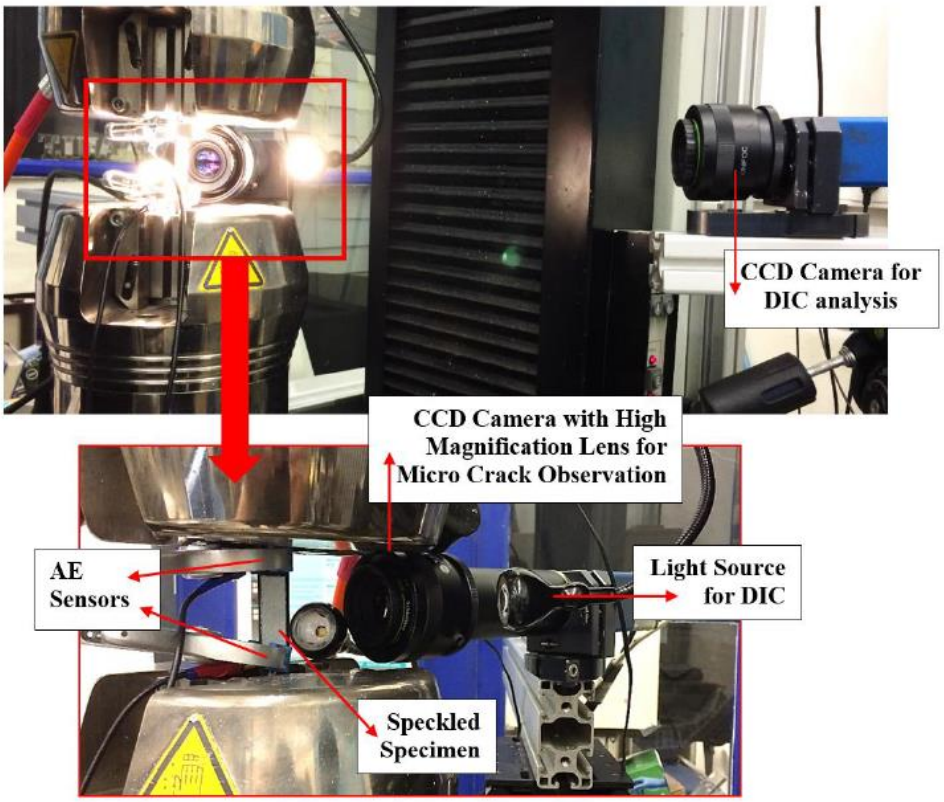

Figure 6.1. Test setup in KU Leuven [71].

6.1. Accoustic Emission (AE)

Acoustic Emission (AE) registration is a useful NDT technique that allows recording and registering damage during mechanical loading of a composite specimen. An acoustic emission signal is an ultrasonic wave which results from the sudden release of strain energy when the damage occurs. These waves can be detected using appropriate sensors. Micromechanical events in the specimen within the test will be converted to electrical signals containing data in time and frequency domain. Vallen AE system situated in KU Leuven accompanied with Vallen AMSY-5 software is preferred in this study due to its better location detecting facilities [72].

6.2. Digital Image Correlation (DIC)

Using AE registration technique solely is not sufficient for detecting damage modes and their correlation with corresponding AE events. Digital Image Correlation (DIC) technique, in addition to AE, is used to identify damage on specimen surface plies and macro damage zones including delaminations in the laminate. The speckled surface of the specimens is used for DIC calculations where displacements of the speckles within an area of interest are captured by consecutive images taken with a Charge-Coupled Device (CCD) camera. The resulted strain maps then used for surface cracks identification.

6.3. Edge Microscopy

To capture the matrix cracks, matrix/fibre debonding and delamination at inner plies of a laminate, free edge of the specimens are photographed during the test by a high resolution and focus camera synchronized with DIC camera shutter speed. Figure 6.2 shows distinct damage modes in a typical edge image captured for $[-45_2/0_2/45_2/90_2]_s$ specimens.

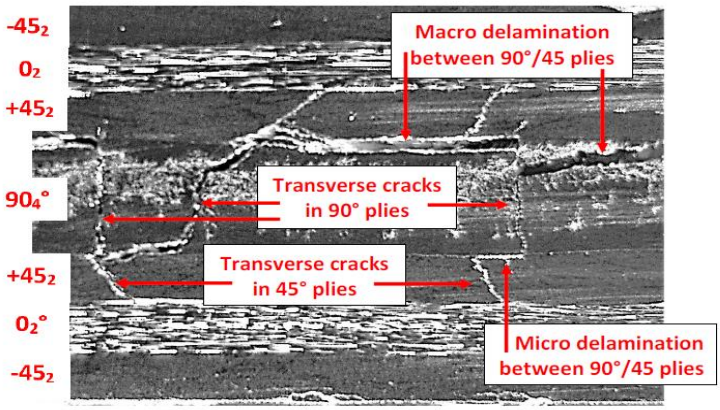

Figure 6.2. An edge image of $[-45_2/0_2/45_2/90_2]_s$ specimen with damage modes identification.

6.4. Experimental Results

Results of the tension test results of OHT quasi-isotropic laminates which are carried out by F.E. Oz [71] at KU Leuven are presented in this section. A summary of combined stress-strain curves and AE registration for five tested specimens with $[+45_2/90_2/-45_2/0_2]_s$ layup is represented in Figure 6.3. The parameters of AE events include Amplitude (A), which is the maximum peak in the AE signal waveform and expressed in dB, Weighted Frequency (WF), which is calculated as the geometric mean of maximum frequency and frequency centroid, expressed in kHz, and location of the AE events. Two sets of plots are provided for the whole gauge length and the observed edge region in two columns. Damage initiates at an average strain level of 0.0042. After the major load drops caused by macro delaminations around 0.0075-0.0081 strain levels, the number of registered signals is reduced significantly. With initiation and evolution of these macro delaminations, the weighted frequency values reduced. The k-means++ clustering algorithm is applied to cluster similar AE signals and correlate them with damage modes. A summary of cluster groups and boundaries from the five tested specimens results are presented in Figure 6.4 [71].

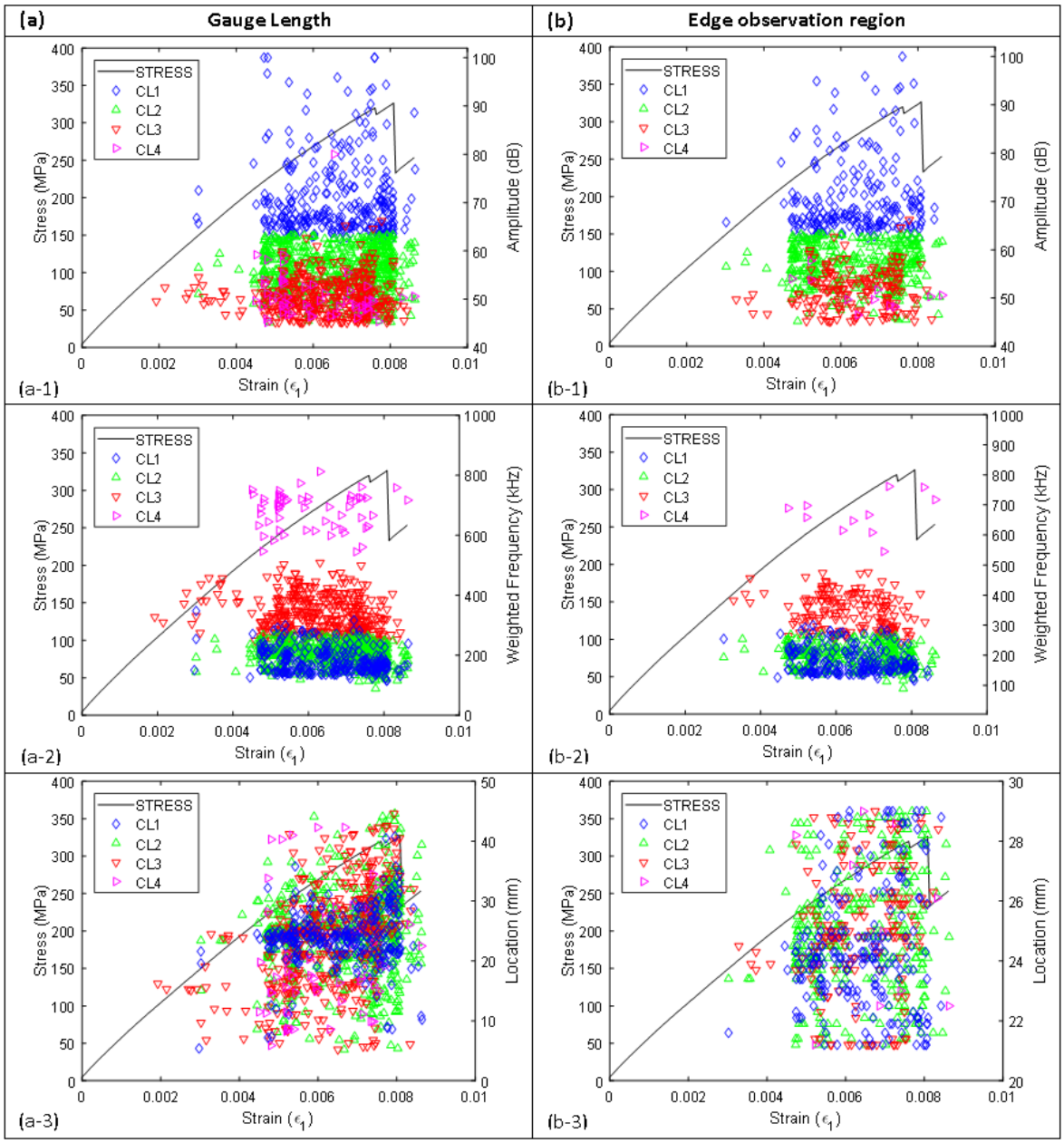

Figure 6.3. Accumulation of AE clusters for $[+45_2/90_2/-45_2/0_2]_s$ laminate: (a) full gage length; (b) edge observation region only; (1) events amplitude; (2) events weighted frequency; (3) events location [71].

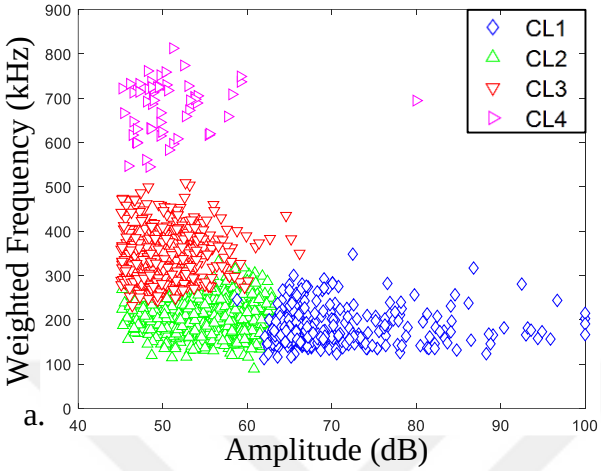

Summary of cluster boundaries		
	A (dB)	WF [kHz]
CL1 ◇	100≥A≥63	350>
CL2 △	63>A>45	280>WF>100
CL3 ▽	63>A>45	540>WF≥310
CL4 ▷	63≥A>45	800≥WF≥540

Figure 6.4. Cluster groups for $[+45_2/90_2/-45_2/0_2]_s$ (a) Clusters from a representative test (b) Cluster boundaries [71].

Figure 6.4 shows the accumulation of AE clusters for the $[+45_2/90_2/-45_2/0_2]_s$ laminates. Four cluster groups have been registered with the damage initiation at 0.0044 strain level. While high-frequency/low-amplitude events (CL3) are mainly registered after 0.0047 strain level in Figure 6.3. The propagation of these events toward the hole region takes place after 0.0051 strain level and will continue to go further away from the AE sensors regions after 0.0070 strain level. These events will gradually disappear with consecutive load drops at 0.0076 followed by 0.0081 strain levels. CL1 events (high-amplitude) are confined to the hole region and initiate at 0.0047 strain level. The propagation of CL1 events to further regions occurs at 0.0071-0.0076 strain levels with load drops caused by macro delamination.

Figure 6.5 shows the edge micrographs as well as strain maps in the loading and transverse directions for various strain levels. The first surface crack adjacent to the hole is detected with DIC at 0.0048 strain level and is shown in Figure 6.5 with the detected delamination within the white rectangle in ε_2 strain map. Surface crack extends toward the edge of the specimen at 0.0053 strain level and the delamination approaches the hole at this strain level as shown within the white rectangle.

These observations are consistent with the CL1 and CL3 events as seen in Figure 6.3. First CL3 evens are recorded between 15-21 mm at 0.0047-0.0052 strain levels with propagation to the hole region (22-27 mm) occurring after 0.0052 and further regions on the other side of the hole region at 0.0071 strain level. These registered events are consistent with delamination extension. So it is highly conceivable to state that CL3 events portray macro delaminations at -45/90 interface.

CL1 events are recorded due to the surface cracks on +45˚ plies with initiation at 0.0048 strain level next to the hole and propagation to outer regions at 0.0053 strain level. After the load drop at 0.0077 strain level, no considerable CL1 events are registered within the hole region since the surface at the vicinity of the hole has been separated and there exists an ongoing separation near the free edges. Therefore, CL1 events represent surface cracks on +45˚ plies.

At 0.0070 strain, first transverse crack in 90˚ plies has been spotted. This is followed by observation of -45/90 interface delamination at 0.0071 strain, its propagation until 0.0076 strain level and appearance of transverse cracks at inner -45˚ plies at this strain level. According to the edge observation region, the separation of upper -45/90 interface induced by macro delamination, occurs at 0.0077 strain level. A negligible number of CL3 and high-frequency (CL4) events are registered after the first load drop due to the extension of macro delamination. The second load drop at 0.0081 strain level appears as a consequence of delamination at lower plies. No CL1 events will be registered after this load drop since the surface ply has been completely separated. It should be noted that distinguishing damage at inner -45˚ and 90˚ plies is considerably difficult since the sensitivity of AE registration regarding micro-damage modes is reduced with the presence of two dominant damage modes: damage at +45˚ surface plies (CL1) and macro delamination (CL3). Low-amplitude/high-frequency (CL4) events are expected to represent transverse cracks at inner -45˚ and 90˚plies. While low-amplitude/low-frequency (CL2) events are anticipated to denote micro delaminations at ±45/90 interfaces [71].

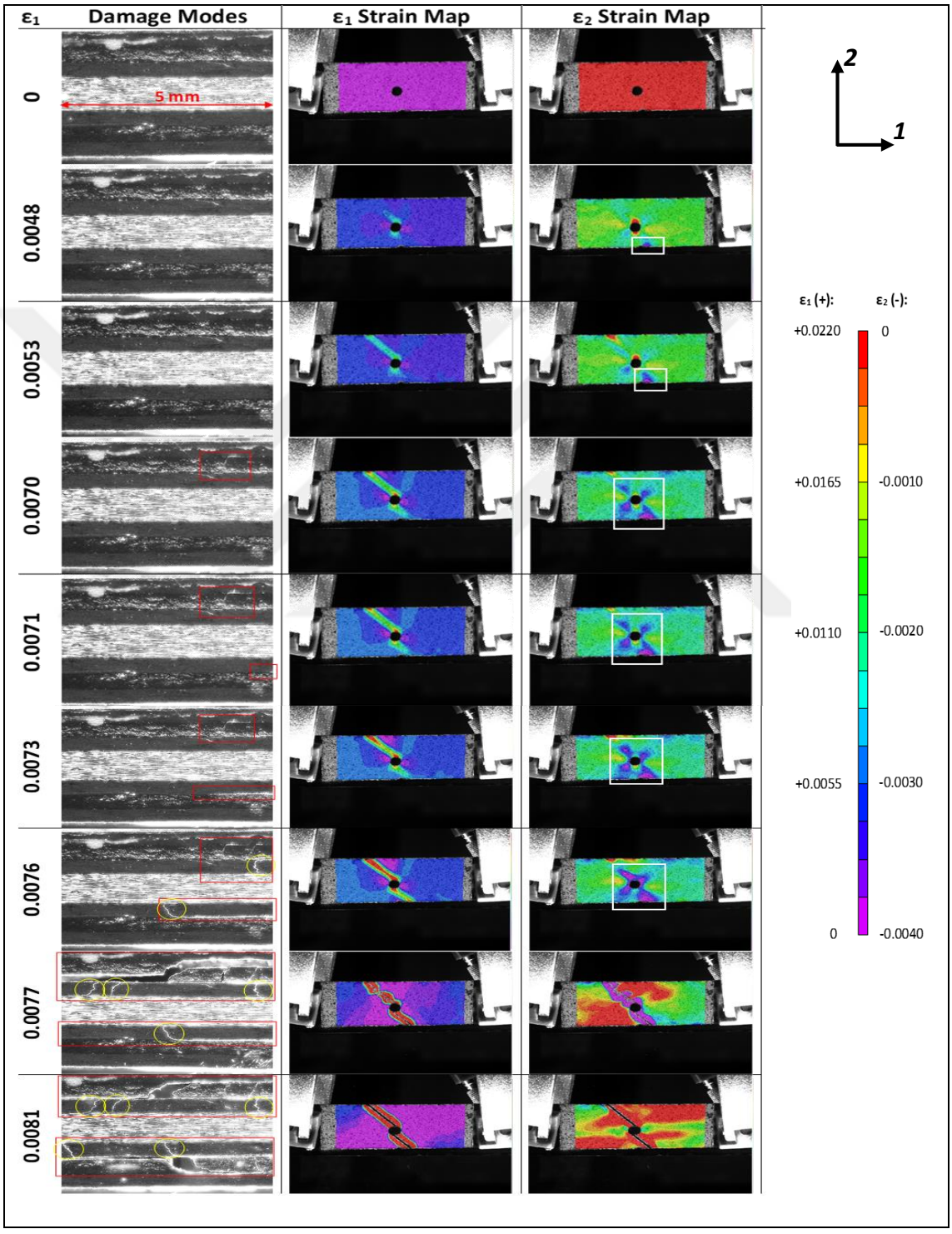

Figure 6.5. Damage evolution in $[+45_2/90_2/-45_2/0_2]_s$ laminate [71].

7. DISCUSSION

The results from experimental tests and FEM are compared with each other in this section. Damage was observed to initiate with micro transverse cracks at 90° plies, followed by surface cracks in +45° plies. Then delaminations occurred at the ±45/90 interface that caused load drop in the stress-strain curve. Finally, delaminations propagated extensively at this interface with delaminations at -45/0 interface which caused higher load drops through the end of the test. The FE model was seen to predict the stress-strain response and damage patterns in OH $[+45_2/90_2/-45_2/0_2]_s$ AS4/8552 laminate successfully. Figure 7.1 demonstrates the stress-strain behaviour measured by experiment and predicted by FE model. In FEA simulation, the first surface crack appears at 0.0043 strain level, the first and the second load drop occurs at 0.0069 and 0.0085 strain levels. The first surface crack at +45˚ ply and first load drop in FE model occurs at earlier strain levels when compared to experimental results. Consecutive load drop is reported to take place at a higher strain level in comparison with experiments.

In Table 7.1 damage progression at different strain levels was compared with FE predictions and the results from two optical observation techniques and FE results are compared with each other, for the mentioned critical stages of damage progression. The delaminations at the free edge of the half model are compared with the edge microscopy and DIC results. The predicted ultimate strength for $[+45_2/90_2/-45_2/0_2]_s$ laminate is in a good correlation with experimental results It can be seen that FE model can successfully predict the sequence of damage modes with less than 10 % error.

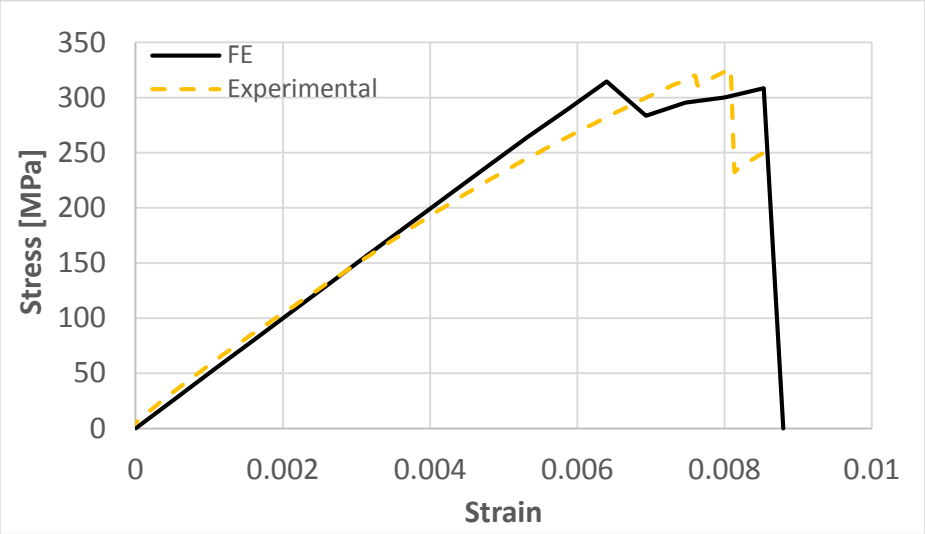

Figure 7.1. Comparison of experimental and FEM stress-strain results.

Table 7.1. Comparison of FE model and experiments.

	First Surface Crack	First Load Drop	Second Load Drop
FEM	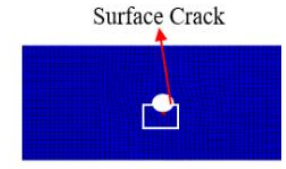 	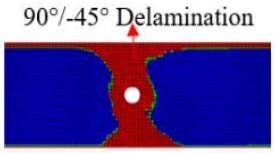 	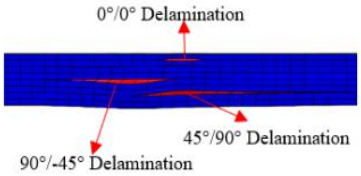
Strain Level	0.0043	0.0069	0.0085
Strain Level	0.0048	0.0077	0.0081
Experiments	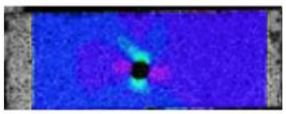 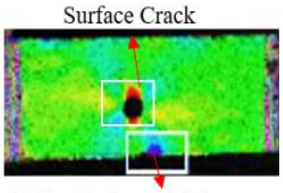	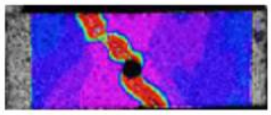 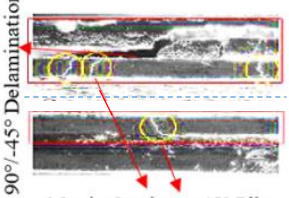	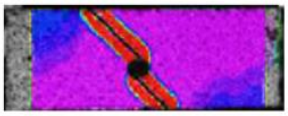 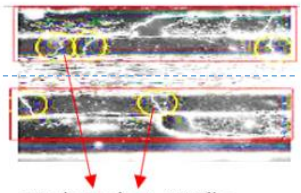

7.1. Modification of the Proposed OHT Model

In order to reduce the computational time of the proposed model, the delamination between two similar consequent plies can be neglected. The modified and simplified symmetric model is consisted of 4 plies with $[+45/90/-45/0]_s$ lay-up orientation, and the thickness of each ply is doubled to consider the presence of neighboring similar ply with no cohesive layer in between. Three cohesive layers are embedded in between these 4 thick plies with the same approach applied in the main model. This schematic view of this model is demonstrated in Figure 7.2. Final state of damage and delaminations are brought in Figure 7.3 and Figure 7.4 respectively. The comparison between stress-strain behaviour of experimental results, main model and the modified model are given in Figure 7.5 and Table 7.2. The detailed progressed damage patterns for composite and cohesive layers are shown in Table 7.3.

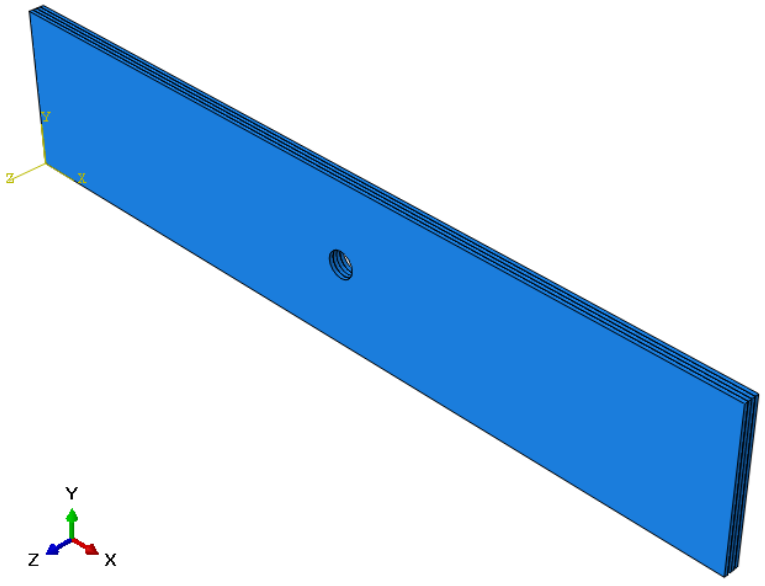

Figure 7.2. Modified OHT model with 4 doubled thickness plies and 3 cohesive layers.

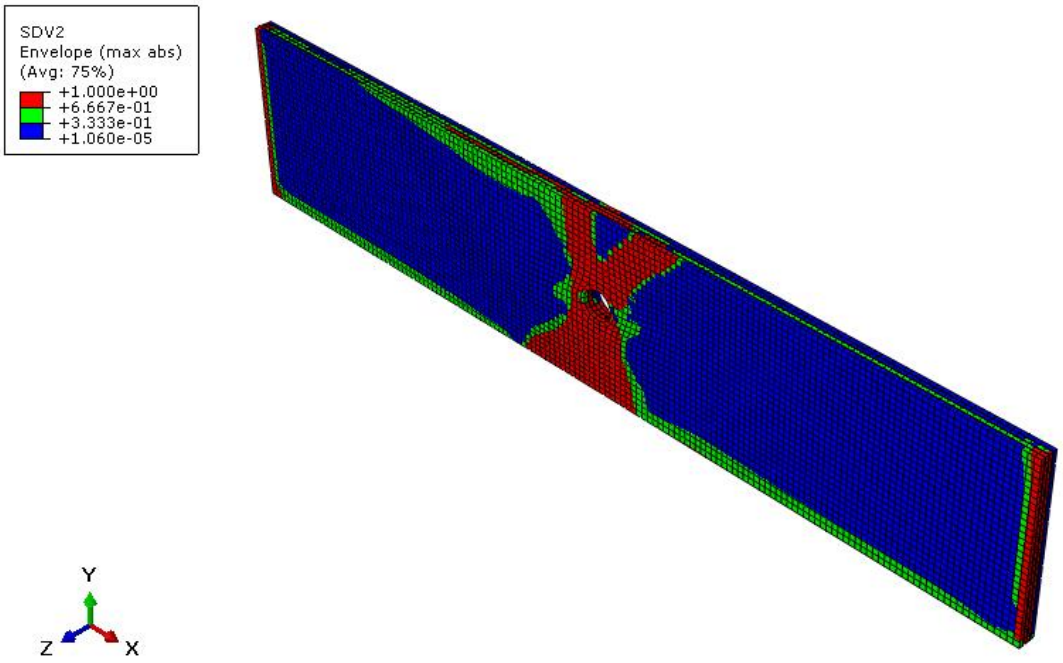

Figure 7.3. Final damage state in modified $[-45_2/0_2/45_2/90_2]_s$ OHT half-model.

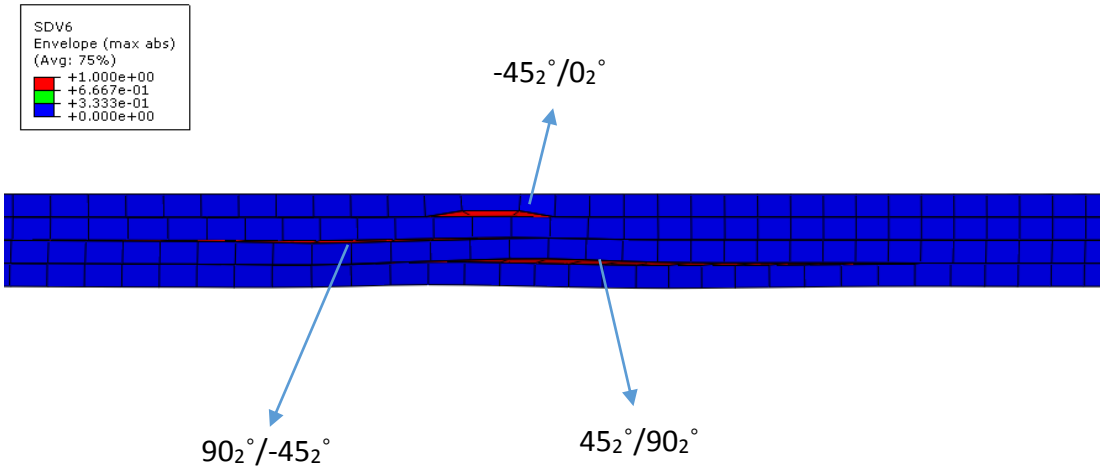

Figure 7.4. Final state of delaminations in modified FE model.

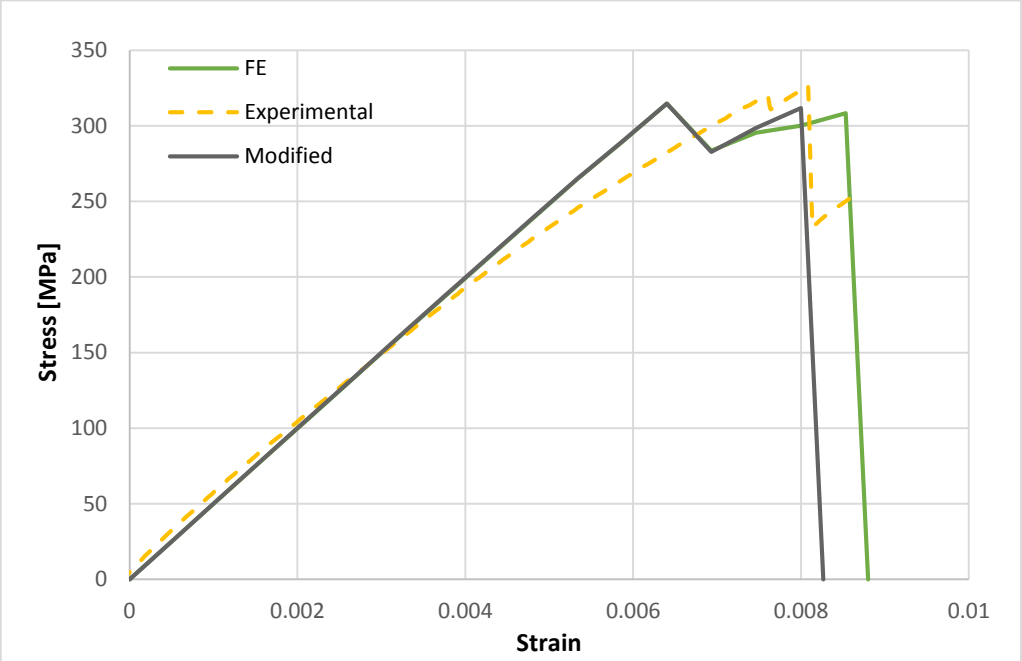

Figure 7.5. Comparison of experimental and FE model stress-strain results.

Table 7.2. Comparison of FE models and experiments.

	First Surface Crack [Strain Level]	**First Load Drop [Strain Level]**	**Second Load Drop [Strain Level]**	**Failure Strength [MPa]**
Experimental	0.0048	0.0077	0.0081	316.25
FE Model	0.0043	0.0069	0.0085	308.35
Modified FE Model	0.0043	0.0069	0.0083	311.65

The obtained results for damage progression from this modified version of the previous model are in a good agreement with the main OHT model results. Neglecting delamination between similar plies will not affect the failure strength and damage patterns significantly. This modified model will considerably reduce the computational time (about 90%).

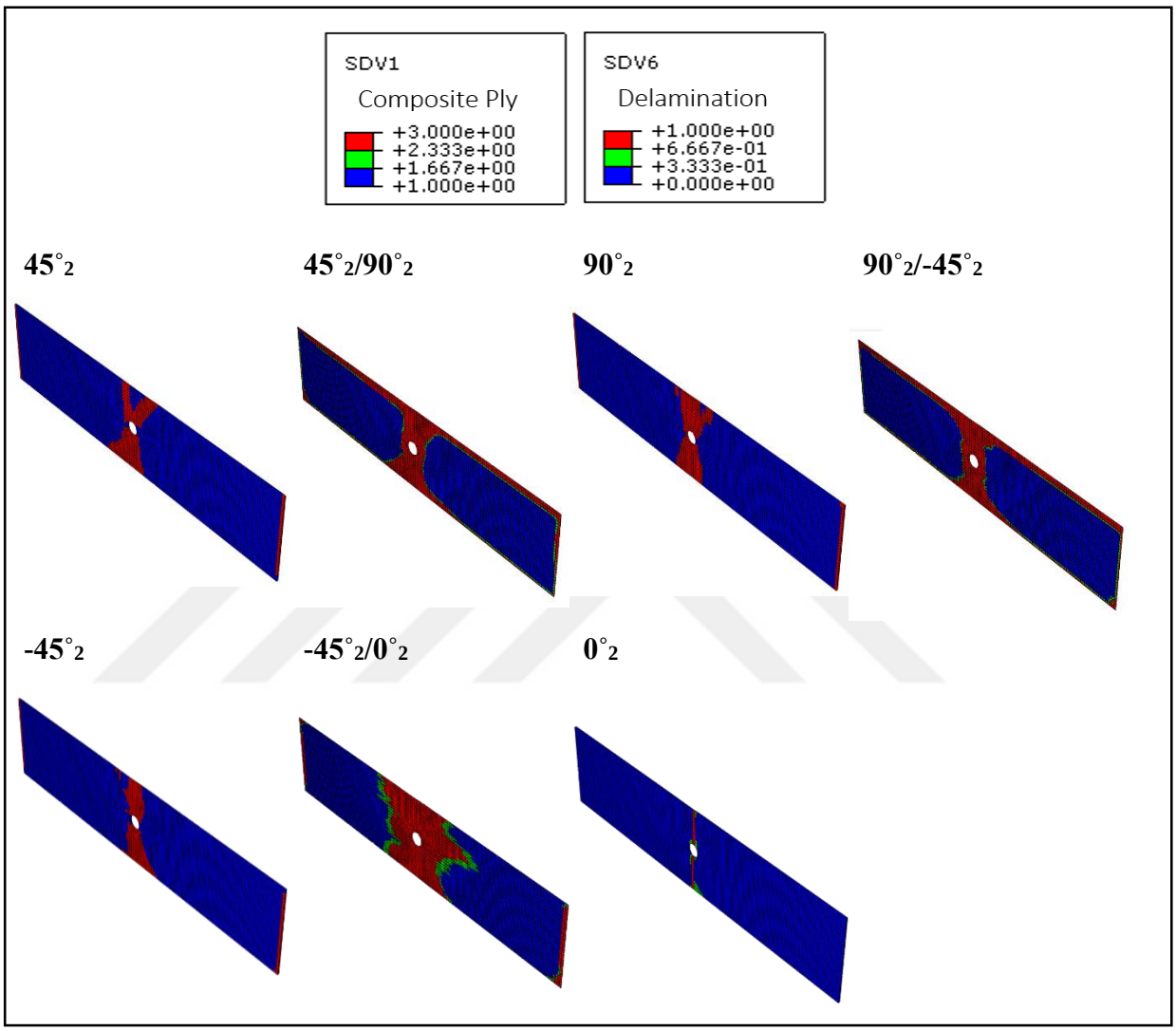

Figure 7.6. Modified FE model results for composite and cohesive layers.

8. CONCLUSION AND FUTURE WORKS

In this study, the progressive failure behavior of the OHT specimens was analyzed both numerically and experimentally. The progressive damage during tensile loading is simulated numerically by taking into account both intralaminar failure and delamination. In conjunction with damage initiation via Hashin's failure criteria, damage evolution law for in-plane failure was defined in terms of fracture energy with linear softening. Initiation and evolution of delamination are based on the Cohesive Zone Model. Numerical and experimental benchmarking studies have also been conducted to evaluate Mode I and Mode II interlaminar fracture toughness by performing Double Cantilever Beam and End-Notched Flexure tests. In experimental part, damage progression in OHT with a 2.5 mm central hole was investigated with Acoustic Emission (AE) technique. Optical instruments have been used to obtain reliable correlations with damage modes and the AE events. Digital Image Correlation (DIC) and *in-situ* edge observation are applied simultaneously during the tensile tests of quasi-isotropic laminates. High-frequency events are registered due to the existence of transverse cracks at the inner ±45˚ plies or the 90˚ plies, whereas high amplitude events around the hole are due to delaminations in the ±45˚/90˚ plies. The model is considered to successfully predict the damage progression and ultimate strength of the OHT specimens. Finally, in order to reduce the computational time, a modified version of the previous model is proposed. The obtained results were in a good agreement with the main OHT model suggesting that neglecting delamination between similar plies will not affect the failure strength and damage patterns significantly. The future work that can be established based on this model can investigate the consistency of numerical results with experimental observations for differently orientated quasi-isotropic OHT laminates and different loading conditions. The predicted ultimate strengths and damage patterns for various cases might be considered valuable in further verification of the proposed model.

REFERENCES

1. Komornicki, J. and L. Bax, "Polymer Composites for Automotive Sustainability", *European Technology Platform for Sustainable Chemistry*, Vol. 12, pp. 5–37, 2017.

2. Mazumdar, S., "Opportunity and Challenges in Automotive Composites Industry", *Lucientel Insights That Matter*, Vol. 25, pp. 1–32, 2013.

3. Chen, B. Y., T. E. Tay, P. M. Baiz, and S. T. Pinho, "Numerical analysis of size effects on open-hole tensile composite laminates", *Composites Part A: Applied Science and Manufacturing*, Vol. 47, No. 1 pp. 52–62, 2013.

4. Girão Coelho, A. M., J. Toby Mottram, and K. A. Harries, "Finite element guidelines for simulation of fibre-tension dominated failures in composite materials validated by case studies", *Composite Structures*, Vol. 126, pp. 299–313, 2015.

5. Bao, H. and G. Liu, "Progressive failure analysis on scaled open-hole tensile composite laminates", *Composite Structures*, Vol. 150, pp. 173–180, 2016.

6. Hallett, S. R., B. G. Green, W. G. Jiang, and M. R. Wisnom, "An experimental and numerical investigation into the damage mechanisms in notched composites", *Composites Part A: Applied Science and Manufacturing*, Vol. 40, No. 5 pp. 613–624, 2009.

7. Saeed, M. U., Z. F. Chen, Z. H. Chen, and B. B. Li, "Comparison of Fracture Characteristics of Open-Hole-Notch Carbon-Fiber-Reinforced Composites Subjected to Tensile and Compressive Loadings", *Mechanics of Composite Materials*, Vol. 52, No. 6 pp. 751–758, 2017.

8. Chen, B. Y., T. E. Tay, S. T. Pinho, and V. B. C. Tan, "Modelling the tensile failure of composites with the floating node method", *Computer Methods in Applied Mechanics and Engineering*, Vol. 308, No. 52 pp. 414–442, 2016.

9. Wisnom, M. R., S. R. Hallett, and C. Soutis, "Scaling Effects in Notched Composites", *Journal of Composite Materials*, Vol. 44, No. 2 pp. 195–210, 2010.

10. Wisnom, M. R. and S. R. Hallett, "The role of delamination in strength, failure mechanism and hole size effect in open hole tensile tests on quasi-isotropic laminates", *Composites Part A: Applied Science and Manufacturing*, Vol. 40, No. 4 pp. 335–342, 2009.

11. Abisset, E., F. Daghia, and P. Ladevze, "On the validation of a damage mesomodel for laminated composites by means of open-hole tensile tests on quasi-isotropic laminates", *Composites Part A: Applied Science and Manufacturing*, Vol. 42, No. 10 pp. 1515–1524, 2011.

12. Zhou, S., Y. Sun, B. Chen, and T.-E. Tay, "Material orthotropy effects on progressive damage analysis of open-hole composite laminates under tension", *Journal of Reinforced Plastics and Composites*, Vol. 36, pp. 1473-1486, 2017.

13. Ridha, M., C. H. Wang, B. Y. Chen, and T. E. Tay, "Modelling complex progressive failure in notched composite laminates with varying sizes and stacking sequences", *Composites Part A: Applied Science and Manufacturing*, Vol. 58, pp. 16–23, 2014.

14. Aidi, B. and S. W. Case, "Experimental and Numerical Analysis of Notched Composites Under Tension Loading", *Applied Composite Materials*, Vol. 22, No. 6 pp. 837–855, 2015.

15. Perogamvros, N. G. and G. N. Lampeas, "Experimental and numerical investigation

of AS4/8552 interlaminar shear strength under impact loading conditions", *Journal of Composite Materials*, Vol. 50, No. 19 pp. 2669–2685, 2016.

16. Mohammadi, R., M. A. Najafabadi, M. Saeedifar, J. Yousefi, and G. Minak, "Correlation of acoustic emission with finite element predicted damages in open-hole tensile laminated composites", *Composites Part B: Engineering*, Vol. 108, pp. 427–435, 2017.

17. Higuchi, R., T. Okabe, and T. Nagashima, "Numerical simulation of progressive damage and failure in composite laminates using XFEM/CZM coupled approach", *Composites Part A: Applied Science and Manufacturing*, Vol. 95, pp. 197–207, 2017.

18. Nagashima, T. and M. Sawada, "Development of a damage propagation analysis system based on level set XFEM using the cohesive zone model", *Computers & Structures*, Vol. 174, pp. 42–53, 2016.

19. Moure, M. M., S. K. García-Castillo, S. Sánchez-Sáez, E. Barbero, and E. J. Barbero, "Influence of ply cluster thickness and location on matrix cracking evolution in open-hole composite laminates", *Composites Part B: Engineering*, Vol. 95, pp. 40–47, 2016.

20. Barbero, E. J. and D. H. Cortes, "A mechanistic model for transverse damage initiation, evolution, and stiffness reduction in laminated composites", *Composites Part B: Engineering*, Vol. 41, No. 2 pp. 124–132, 2010.

21. Green, B. G., M. R. Wisnom, and S. R. Hallett, "An experimental investigation into the tensile strength scaling of notched composites", *Composites Part A: Applied Science and Manufacturing*, Vol. 38, No. 3 pp. 867–878, 2007.

22. Serra, J., C. Bouvet, B. Castanié, and C. Petiot, "Scaling effect in notched composites:

The Discrete Ply Model approach", *Composite Structures*, Vol. 148, pp. 127–143, 2016.

23. Erçin, G. H., P. P. Camanho, J. Xavier, G. Catalanotti, S. Mahdi, and P. Linde, "Size effects on the tensile and compressive failure of notched composite laminates", *Composite Structures*, Vol. 96, pp. 736–744, 2013.

24. Tay, T. E., "Damage Progression in Open-hole Tension Laminates by the SIFT-EFM Approach", *Journal of Composite Materials*, Vol. 40, No. 11 pp. 971–992, 2005.

25. Amacher, R., J. Cugnoni, J. Botsis, L. Sorensen, W. Smith, and C. Dransfeld, "Thin ply composites: Experimental characterization and modeling of size-effects", *Composites Science and Technology*, Vol. 101, pp. 121–132, 2014.

26. Masuelli, M. A., "Introduction of Fibre-Reinforced Polymers-Polymers and Composites: Concepts, Properties and Processes", *Fiber Reinforced Polymers - The Technology Applied for Concrete Repair*, pp. 1-40, 2013.

27. Andersoon, M. and P. Liedberg, *Crash behavior of composite structures: A CAE benchmarking study*, Master's Thesis, Chalmers University of Technology, 2014.

28. Gutkin, R. and S. T. Pinho, "Review on failure of laminated composites: Experimental perspective and modelling", *Chalmers University of Technology Publishings*, pp. 1-43, 2016.

29. Carlsson, L. A., D. F. Adams, and R. B. Pipes, "Basic experimental characterization of polymer matrix composite materials", *Polymer Reviews*, Vol. 53, No. 2 pp. 277–302, 2013.

30. Hyer, M. W., *Stress Analysis of Fiber-Reinforced Composite Materials*, McGraw-Hill

International Editions, 1998.

31. Song, K., C. Davila, and C. Rose, "Guidelines and parameter selection for the simulation of progressive delamination", *2008 ABAQUS User's Conference*, pp. 1–15, 2008.

32. Barenblatt, G. I., "The mathematical theory of equilibrium cracks in brittle fracture", *Advanced Appllied Mechanics*, Vol. 7, pp. 55–129, 1962.

33. Dugdale, D. S., "Yielding of steel sheets containing slits", *Journal of Mechanics and Physics of Solids*, Vol. 8, pp. 100–104, 1960.

34. Hillerborg, A., M. Modeer, and P. E. Petersson, "Analysis of crack formation and crack growth in concrete by means of fracture mechanics and finite elements", *Cement and Concrete Research*, Vol. 6, pp. 773–782, 1976.

35. Camanho, P. P., C. G. Dávila, and D. R. Ambur, "Numerical Simulation of Delamination Growth in Composite Materials", *NASA Langley Technical Report Server*, pp. 1–24, 2001.

36. Turon, A., P. P. Camanho, J. Costa, and C. G. Dávila, "A damage model for the simulation of delamination in advanced composites under variable-mode loading", *Mechanics of Materials*, Vol. 38, No. 11 pp. 1072–1089, 2006.

37. Gigliotti, L., *Assessment of the applicability of XFEM in Abaqus for modeling crack growth in rubber Luigi Gigliotti*, Master's Thesis, KTH School of Engineering Sciences, 2012.

38. Harper, P. W. and S. R. Hallett, "Cohesive zone length in numerical simulations of composite delamination", *Engineering Fracture Mechanics*, Vol. 75, No. 16 pp.

4774–4792, 2008.

39. Turon, A., C. G. Dávila, P. P. Camanho, and J. Costa, "An engineering solution for mesh size effects in the simulation of delamination using cohesive zone models", *Engineering Fracture Mechanics*, Vol. 74, No. 10 pp. 1665–1682, 2007.

40. Falk, M. L., A. Needleman, and J. R. Rice, "A critical evaluation of dynamic fracture simulations using cohesive surfaces", *Journal de Physique*, Vol. 4, pp. 43–50, 2001.

41. Alfano, G., S. De Barros, L. Champaney, and N. Valoroso, "Comparison Between Two Cohesive-Zone Models for the Analysis of Interface Debonding", *Proceedings of the ECCOMAS 2004 European Congress on Computational Methods in Applied Sciences and Engineering*, pp. 1–18, 2004.

42. Rice, J. R., "The mechanics of earthquake rupture", *Physics of the Earth's Interior*, Vol. 5, pp. 555–649, 1980.

43. Irwin, G. R., "Plastic zone near a crack and fracture toughness," *Proceedings of the Seventh Sagamore Ordnance Materials Conference*, Vol. 4, pp. 1-4, 1960.

44. Hui, C. Y., J. A., S. J. Bennison, and J. D. Londono, "Crack blunting and the strength of soft elastic solids", *Proceedings of the Royal Society A: Mathematical, Physical and Engineering Sciences*, Vol. 459, No. 2034 pp. 1489–1516, 2003.

45. Tsai, S. W. and E. M. Wu, "A General Theory of Strength for Anisotropic Materials", *Journal of Composite Materials*, Vol. 5, No. 1 pp. 58–80, 1971.

46. Azzi, V. D. and S. W. Tsai, "Anisotropic strength of composites - Investigation aimed at developing a theory applicable to laminated as well as unidirectional composites, employing simple material properties derived from unidirectional specimens alone",

Experimental Mechanics, Vol. 5, No. 9 pp. 283–288, 1965.

47. Hashin, Z., "Failure Criteria for Unidirectional FibreComposites", *Journal of Applied Mechanics*, Vol. 47, pp. 329–334, 1980.

48. Abaqus Inc., *Aabqus Lecture 9 : Material Damage and Failure*, pp. 1–19, 2005.

49. Dassault Systems, "Damage initiation for fiber-reinforced composites", *Abaqus 6.11 Analysis User's Manual*.

50. Dassault Systems, "Damage evolution and element removal for fiber-reinforced composites", *Abaqus 6.11 Analysis User's Manual*.

51. Matzenmiller, A., J. Lubliner, and R. L. Taylor, "A constitutive model for anisotropic damage in fiber-composites", *Mechanics of Materials*, Vol. 20, pp. 125–152, 1995.

52. Dassault Systems, "Defining the constitutive response of cohesive elements using a traction-separation description," *Abaqus 6.11 Analysis User's Manual*.

53. Camanho, P.P. and C. G. Davila, "Mixed-Mode Decohesion Finite Elements in for the Simulation Composite of Delamination Materials", *NASA/TM-2002-211737*, pp. 1–37, 2002.

54. Benzeggagh, M. L. and M. Kenane, "Measurement of mixed-mode delamination fracture toughness of unidirectional glass/epoxy composites with mixed-mode bending apparatus", *Composites Science and Technology*, Vol. 56, No. 4 pp. 439–449, 1996.

55. Chen, J., E. Ravey, S. Hallett, M. Wisnom, and M. Grassi, "Prediction of delamination in braided composite T-piece specimens", *Composites Science and Technology*, Vol.

69, No. 14 pp. 2363–2367, 2009.

56. Lapczyk, I. and J. A. Hurtado, “Progressive damage modeling in fiber-reinforced materials”, *Composites Part A: Applied Science and Manufacturing*, Vol. 38, No. 11 pp. 2333–2341, 2007.

57. Hexcel, “HexPly ® 8552 - Product Data Sheet - EU Version”, pp. 1–6, 2016.

58. Shivakumar, K. N., R. Panduranga, J. Skujins, and S. Miller, “Assessment of mode-II fracture tests for unidirectional fiber reinforced composite laminates”, *Journal of Reinforced Plastics and Composites*, Vol. 34, No. 23 pp. 1905–1925, 2015.

59. Lemanski, S. L., J. Wang, M. P. F. Sutcliffe, K. D. Potter, and M. R. Wisnom, “Modelling failure of composite specimens with defects under compression loading”, *Composites Part A: Applied Science and Manufacturing*, Vol. 48, No. 1 pp. 26–36, 2013.

60. Oz, F. E., “Micromechanical Progressive Damage Model for Predicting Resin Dominated Strength Values of Fibre Reinforced Composites Under Various Types of Loading”, Master's Thesis, Bogazici University, 2012.

61. ASTM, “D3039/D3039M: Standard Test Method for Tensile Properties of Polymer Matrix Composite Materials”, *Annual Book of ASTM Standards*, Vol. 14, pp. 1–13, 2014..

62. ASTM, “D5766/5766M: Standard Test Method for Open-Hole Tensile Strength of Polymer Matrix Composite”, *Annual Book of ASTM Standards*, Vol. 13, pp. 1–7, 2013.

63. Sandvik, “Composite Product Solutions”, *Sandvik Coromat*, pp. 34–55, 2011.

64. ASTM, "D5528-13: Standard Test Method for Mode I Interlaminar Fracture Toughness of Unidirectional Fiber-Reinforced Polymer Matrix Composites", *Annual Book of ASTM Standards*, Vol. 13, pp. 1–12, 2013.

65. ASTM, "D7905/D7905M-14: Standard Test Method for Determination of the Mode II Interlaminar Fracture Toughness of Unidirectional Fiber-Reinforced Polymer Matrix Composites", *Annual Book of ASTM Standards*, Vol. 15, pp. 1–18, 2014.

66. Mujika, F., N. Carbajal, A. Arrese, and I. Mondragon, "Determination of tensile and compressive moduli by flexural tests", *Polymer Testing*, Vol. 25, No. 6 pp. 766–771, 2006.

67. Dassault Systems, "Time Incrementation Tab", *Abaqus 6.11 Analysis User's Manual*.

68. Dassault Systems, "Customizing General Solution Controls", *Abaqus 6.11 Analysis User's Manual*.

69. Autodesk Knowledge Network, "Autodesk Helius PFA: Appendix C - MCT State Variables for Composite Materials", *User's Guide for Abaqus*, 2016.

70. Autodesk Knowledge Network, "Autodesk Helius PFA: Appendix D - MCT State Variables for Cohesive Materials", *User's Guide for Abaqus*, 2016.

71. Oz, F. E., "Characterisation of Failure in Composite Materials with Acoustic Emission and Correlation with Micromechanics", Ph.D. Thesis, Bogazici University, 2018.

72. Oz, F. E., N. Ersoy, and S. V. Lomov, "Do high frequency acoustic emission events always represent fibre failure in CFRP laminates?", *Composites Part A: Applied Science and Manufacturing*, Vol. 103, pp. 230–235, 2017.